HIGH-RESOLUTION CHARACTERZATION OF LOW-DIMENSIONAL DEFECTS IN $SrTiO_3$

By

GUOZHEN ZHU, M. A. Sc.

A Thesis

Submitted to the School of Graduate Studies

in Partial Fulfillment of the Requirements

for the Degree of

Doctor of Philosophy

McMaster University

Doctor of Philosophy (2012) McMaster University
Department of Materials Science and Engineering Hamilton, Ontario

TITLE: HIGH-RESOLUTION CHARACTERIZATION OF LOW-DIMENSIONAL DEFECTS IN $SrTiO_3$

AUTHOR: GUOZHEN ZHU, M. A. Sc.

SUPERVISOR: Dr. GIANLUIGI A. BOTTON

NUMBER of PAGES: xiv, 128

ABSTRACT

Strontium titanate ($SrTiO_3$) has a wide range of applications in the electronic industry and attracts growing world-widely interest recently because of novel discoveries at its surfaces, interfaces and with selected dopants. The understanding of some of the structural properties of $SrTiO_3$ and its optical properties have been lagging due to limited characterization techniques available to study single monolayers and dopants in this material.

In the present thesis, pure $SrTiO_3$ single crystals with (2x1) and c(4x2) surface patterns were synthesized and samples (Pr, Al) doped $SrTiO_3$ were prepared through ion implantation. The atomic and electronic structures of these samples were investigated by various high-resolution imaging and spectroscopic techniques available in an aberration-corrected transmission electron microscope. Particularly, the direct imaging of individual light atoms and vacancies within a bulk material containing heavier elements was demonstrated for the first time via the STEM-annular dark-field (ADF)/annular bright-field (ABF) images. In addition, the first electron energy-loss spectroscopy (EELS) 2-dimensional maps of dopants located in a lattice were obtained. These results provided a solid foundation regarding the mechanism of red light emission in doped $SrTiO_3$. More importantly, a new experimental approach allowing the effective extraction of weak EELS signals from low-dimensional defects was developed and successfully applied to understand the chemical state and coordination of Ti cations within a single monolayer on a reconstructured $SrTiO_3$ surface and the local defect configurations of injected Pr^+ and Al^+ ions within $SrTiO_3$ single crystals.

ACKNOWLEDGEMENTS

At the end of my enjoyable and difficult journey in obtaining a Ph.D. degree, I would like to thank all those people who contributed in many ways to the success of this project and made it an unforgettable experience for me.

It is impossible to overstate my gratitude to my supervisor, Dr. Gianluigi A. Botton, who is not only a wonderful supervisor but also a true friend. I am sincerely indebted to him from his incredible knowledge and deep insight in the field of electron microscopy, particularly in the field of electron energy-loss spectroscopy. At many stages during this research project I benefited from his inspirational guidance, invaluable advice and unselfish help. He has taught me, both consciously and un-consciously, to have a sharp mind and eyes in science while keeping a good, well-rounded attitude. Without his continual guidance, encouragement and support, this work would not have been completed.

I am deeply grateful to my supervisory committee members, Dr. Andrew P. Knights and Dr. John S. Preston, who provided detailed and constructive feedback throughout this work. I would not access to the implantation technique without the important support from Dr. Knights.

I wish to express my sincere thanks to Dr. Martin Couillard, Dr. Yang Shao and Dr. Kai Cui. Their ideas and concepts have had a remarkable influence on my entire career in the field of electron microscope. Martin not only kindly offered training on the high-resolution imaging and spectroscopic techniques but also provided extensive discussions and valuable advice on my work. Yang and Kai offered me interesting explorations in operations and deep discussions, which had been very helpful at the beginning of this study.

Special thanks to the technical staffs at the Canadian Centre for Electron Microscopy: Dr. Carmen Andrei, Mr. Andy Duft, Mr. Wenhe Gong and Mr. Fred Pearson.

Andy always offered very kindly and quick feedback whenever I have bothered him with questions and reporting problems. Fred taught me both TEM sample preparations and the basic operation of the microscopes. Gong provided interesting discussions on preparing TEM specimens. The work present in this thesis would not go smoothly without their continuous help.

The assistance of the following people at McMaster University is also appreciated:

Mrs. Doris Stevanovic for implantation

Mr. Jim Garrett and Dr. Tihe (Tom) Zhou for heat treatment

Mr. Patrick Wilson for photoluminescence testing

I am also grateful for the assistance of Dr. Ken Burch at Toronto University for ellipsometry, Dr. Sorin Lazar at FEI company for the help with the atomic EELS mapping and Dr. Huikai (Kay) Cheng at FEI company for the help with the super-EDX mapping.

I also obtained enormous help from all my friends inside and outside the lab: David Rossouw, Steffi Woo, Shahrzad Hosseini, Xinxin Zhao, Samantha Stambula and other good friends. I am grateful for the discussions and suggestions from David and Shahrzad on the operation of the microscope (Titan). I wish to thank Xinxin, David and Samantha to edit my abstracts and papers. Very special thanks to Steffi for her essential assistance in editing my proposal and proofreading my thesis. I wish to thank all my friends for their help on various aspects of my living in Canada.

Finally, a special thought is also devoted to my parents for the never-ending support. Their understanding and their endless love encouraged me to work hard and to continue pursuing a Ph.D. degree abroad. I would not have completed this journey if not for my parents.

Guozhen Zhu

Hamilton, 2012

OUTLINE

LIST OF FIGURES

LIST OF TABLES

LIST OF ABBREVIATIONS

α	Convergence angle
β	Inner collection angle
ε_2	Imaginary part of the dielectric function
ε_{xx}	Normal strain along x axis
ε_{xx}	Normal strain along y axis
τ_{xy}	Shear strain in x-y plane
ABF	Annular Bright Field
ADF	Annular Dark Field
AFM	Atomic Force Microscope/Microscopy
BF	Bright Field
Cs	Spherical Aberration Coefficient Value
CBED	Convergent-beam Electron Diffraction
CL	Camera Length
CMP	Chemical Mechanical Polishing
CTS	Charge Transfer State
CTM4XAS	Charge Transfer Mutliplet Calculations for X-ray Absorption Spectroscopy
DP	Diffraction Pattern
EDX	Energy Dispersive X-ray Spectrometry
EELS	Electron Energy-loss Spectrometer/Spectrometry
ELNES	Energy-loss Near Edge Structure
EPR	Electron Paramagnetic Resonance
ESR	Electron Spin Resonance
EWR	Exit Wave Reconstruction
EXAFS	X-ray Absorption Fine Structure
FIM	Field-ion Microscope
GPA	Geometric Phase Analysis
HA	High-angle
HAADF	High-angle Annular Dark Field
IVCT	Inter-valence Charge Transfer

J_{cv}	Interband transition strength
JDOS	Joint Density of States
LA	Low-angle
LAADF	Low-angle Annular Dark Field
LEED	Low-energy Electron Diffraction
ML	Maximum Likelihood
NMR	Nuclear Magnetic Resonance
PACBED	Position Averaged Convergent-beam Electron Diffraction
PCA	Principal Component Analysis
pdf	Probability Density Function
PL	Photoluminescence
RBS	Rutherford Backscattering Spectrometry
RE	Rare-earth
RHEED	Reflection High-energy Electron Diffraction
RT	Room Temperature
STE	Self-trapped Exciton
STEM	Scanning Transmission Electron Microscope/Microscopy
STM	Scanning Tunneling Microscopy
SRIM	The Stopping and Range of Ions in Matter
S_{xtal}	The scaling of the crystal field strength
TEM	Transmission Electron Microscope/Microscopy
TM	Transition Metal
TRR	Time-resolved Reflectivity
XAS	X-ray Absorption Spectroscopy
Z	Atomic number
ZLP	Zero-loss Peak

LIST OF SOFTWARES

SRIM-2008.04

Multislice (Kirkland et al, 2010)

CTM4XAS 5.2

MultiX v1.0.0

MATLAB 7.6.0.324

Digital Micrograph(TM) 3.11.1

CHAPTER ONE

INTRODUCTION

With the technical breakthrough of creating structures on well-defined ionic planes, oxides have recently attracted growing world-wide interest and have lead to novel discoveries due to their unique combination of physical properties and the fact that these materials can be stacked up into 'heterostructures' for multiple devices in the electronic and optoelectronic industry.[1,2] The physical properties of these oxides are ultimately determined by their electronic band structures and are additionally strongly affected by defects and low-dimensional features present in the system. A full understanding of their local defect configurations and subsequent effects on their properties is thus required. However, the characterization of these structures has been limited in the past to broad beam techniques as several studies have been carried out mainly through X-ray absorption spectroscopy (XAS), nuclear magnetic resonance (NMR) and electron paramagnetic resonance (EPR). These techniques have been used to obtain the average physical and chemical information of the chemical species of these defects due to the limited spatial resolution. Therefore, these questions related to the local defect configurations, chemistry and structure are still in dispute. As the electronic/optical

devices continue to shrink in size, the direct determination and characterization of atomic arrangement and electronic environment of individual low-dimensional defects become even more essential.

Amongst a huge family of oxides, $SrTiO_3$ single crystals are of particularly technological interest in microelectronic and optoelectronic industries because of the high dielectric constant, good ferroelectric and insulating properties, outstanding wear resistance and high chemical and thermal stabilities. $SrTiO_3$ is also one of most popular substrates for various complex-oxide thin film[3] and nanostructure growth[4]. Recently, novel properties have been discovered including electric-field-induced superconductivity[5], two-dimensional (2D) interface superconductivity exhibited at its interfaces with $LaAlO_3$ [6], extremely high carrier mobility in doped $SrTiO_3$ single crystals[7] and blue-light emission at room temperature from Ar^+-irradiated $SrTiO_3$ [8]. In spite of their scientific and technological importance, the understanding of the atomic and electronic structure of the surfaces and doped $SrTiO_3$ is still poor, due to the lack of effective high-resolution (HR) characterization techniques to target single monolayer surfaces and single dopants within a $SrTiO_3$ lattice.

With techniques such as scanning transmission electron microscopy (STEM) and electron energy-loss spectroscopy (EELS), high-resolution (HR) transmission electron microscopy (TEM) opens the path to the study of chemical composition and bonding information[9,10] coupled with the atomic level images[11,12], and thus provides an ideal tool to investigate individual low-dimensional defects. The general objective of this Ph.D. thesis is to investigate individual low-dimensional structures making use of the most recent developments in electron microscopy techniques so as to probe the structure of two systems of great interest: 1) the reconstructed surfaces of $SrTiO_3$ due to their fundamental importance as standard substrates and 2) ion implanted layers in $SrTiO_3$ and this because of their optical properties. Using aberration-corrected microscopy, the nature of the surfaces and the nature of the clusters generated following implantation have been studied at the atomic level so as to provide a fundamental understanding of the observed properties.

Because these low-dimensional defects cannot be physically isolated from the bulk, it is difficult to correctly and effectively extract the weak signals from these defects presented in a solid bulk. Such extraction remains a very challenging issue even in TEM where thin foils, with thickness is less than 100 nm, are used. Thus, beside the general investigation of selected $SrTiO_3$ systems through HR microscopy characterization techniques, my goal is also to collect structural and spectral information from single monolayers and dopants in $SrTiO_3$ by extending available techniques and developing new approaches. The visibility of these low-dimensional defects can be enhanced by picking up corresponding signals since the elastically scattered electrons contributing to signals from these low-dimensional defects are distributed unevenly in space and differently compared to the ones contributed by the bulk. The STEM-annular bright-field (ABF) imaging technique was demonstrated for the first time to directly image individual light atoms and vacancies within a bulk with heavier elements. Regarding the fact that EELS signals from the defects and the bulk are distributed similarly in space, a new experimental approach, based on a 'thickness' series of EEL spectra containing different bulk contributions, was proposed to effectively extract weak EELS signals from these low-dimensional defects. Through this approach, the chemical state and coordination of Ti cations within a single monolayer on a reconstructed surface and the local defect configurations of nano-clusters generated in (Pr, Al) implanted $SrTiO_3$ were successfully solved.

The structure of the thesis is listed as follows. Chapter 2 gives the necessary background, highlights the issues of interest and systematically reviews the previous work done on the selected systems. Chapter 3 describes the experimental methods and techniques applied in the present work. In Chapter 4, we present the new experimental approaches we developed on how to correctly and effectively extract weak signals attributed to these low-dimensional defects. Following that, Chapter 5 presents the results on the reconstructed (001) $SrTiO_3$ surfaces, which provide the experimental evidence on the atomic structure along missing direction in the literature and both experimental and simulated electronic structure of the reconstructed surfaces for the first time. Chapter 6

gives the analysis of bulk defects within the implanted $SrTiO_3$ single crystals. We observed that the Al ions have a negative instead of positive effect on the emission intensity but blue-shift the red emission peak. The associated electronic structure and the detailed atomic model were investigated by EELS and STEM-HAADF/ABF images. We also presented the first observations of light elements (Al) within a heavier lattice ($SrTiO_3$) by ABF images and the first EELS 2-dimensional map of dopants (Pr) within a lattice. The conclusions as well as suggestions for future study are stated in Chapter 7.

CHAPTER TWO

LITERATURE REVIEW

Oxides have led to novel discoveries and have received increasing attention in the electronic and optoelectronic industry. Their physical properties are strongly affected by low-dimensional defects present in them; however, the understanding of their local defect configurations is still incomplete. In this chapter, a brief introduction of defects in oxides is given and followed by two detailed cases: the surfaces of perovskite-type $SrTiO_3$ lattice, and (Pr, Al) implanted $SrTiO_3$ single crystals. In each case, we summarize the previous work and highlight the current research hotspots. Lastly, a detailed description of characterization of individual low-dimensional defects using transmission electron microscopy (TEM) is given.

2.1 DEFECTS IN OXIDES: AN OPPORTUNITY FOR FUTURE DEVICES

Since the high-temperature superconducting phenomenon was discovered in oxides in 1986, the understanding of oxides has continuously challenged our view of the solid. The application of oxides in the electronic industry was initially slow due to manufacturing issues. Subsequently, with the technical breakthroughs of creating oxides by novel thin film deposition techniques with well-controlled structures, i.e., atomically-sharp interfaces, there is currently a race to make new discoveries using oxide materials, mainly in the field of electronics and optoelectronics. The remarkable physical properties discovered in oxides, e.g. extremely high magnetoresistance, have been applied to next generation devices and lead to significant reduction in size of devices in the electronic industry.[1,13]

Colossal magnetoresistance (GMR)[14], i.e. an orders-of-magnitude change in electrical resistance as a result of a slight change of the external magnetic field, was discovered in 1993 and has been applied in memory devices and sensors. GMR exists in perovskites $T_{1-x}D_xMnO_3$, where T is a trivalent lanthanide cation (e.g. La) and D is a divalent, e.g. alkaline-earth (e.g. Ca, Sr, Ba), cation. The quantum Hall effect[15] observed in ZnO-$Mn_xZn_{1-x}O$, in which the free-roaming electrons inside a layer condense into a liquid-like state, provides the possibility for 'spintronics' devices. Two-dimensional electron gas[6] describing the high-mobility electrons was reported at the interface between $LaAlO_3/SrTiO_3$, which may be the scientific foundation for the next generation of fast transistors.

The story of oxide electronics could go even further since there are more than enough possible choices based on the huge family of oxides and various underlying physical effects. Beyond that, due to the common sub-lattice of oxygen atoms, various multi-effects, e.g. multiferroics[16], could be achieved with designed heterostuctures via epitaxial growth. However, the most novel phenomena appear only in oxides with designed defects including atomically-sharp interface and dopants. Therefore, the

understanding and controlling of defects will be the key to bring oxides from the current scientific curiosity and discoveries to practical technologies.

The development of characterization techniques such as TEM has lead to improved understanding of several functional oxides. For example, Y dopants in alumina improve its mechanical properties due to the regular distribution of Y atoms along grain boundaries[17]; designable stability at high-temperatures is achieved in La-doped Al_2O_3 catalysts[18]. In short, creating and characterizing artificial structure at the atomic scale provide us the great opportunity to achieve the final application goals through understanding the underlying structure-property relationship at the nanometer scale.

2.2 SURFACE DEFECTS: RECONSTRUCTED $SrTiO_3$ SURFACE

The surfaces of metal oxides are defective in nature and have been extensively studied for various fundamental properties and related technological applications. Amongst them, the surfaces of $SrTiO_3$ crystals were used initially as lattice-matched substrates for high-T_c superconductors such as $YBa_2Cu_3O_{7-x}$ lattice. Nowadays they are used as a standard substrate for the epitaxial growth of various functional thin films[3] and nano-structures[4], and as the preferential photo-catalyst to split water for solar hydrogen generation[19]. In spite of the technological and scientific importance of $SrTiO_3$ crystal surfaces, the understanding of their atomic structure is still incomplete due to the limited high-resolution (HR) characterization. In addition, to assess the possible surface reactions and bonding occurring during the growth process or the deposition of catalysts on their surfaces, it is particularly important to understand the electronic structure of $SrTiO_3$ reconstructed surfaces.

High-resolution characterization of metal oxide surfaces is limited on account of their defective structure, non-stoichiometric complexity and insulating properties. As a result, modern surface analytical tools, such as electron spectroscopy and scanning tunneling microscopy (STM), are not fully applicable although extensive work has been done on doped $SrTiO_3$ surfaces[20]. Noncontact atomic force microscopy (AFM) seems to

be the only applicable powerful tool but provides only outermost surface information with limited spatial resolution. Compared to the above techniques, TEM provides simultaneous insight into both surface patterns and associated electronic structure. However, TEM signals are integrated in projection and therefore are sensitive to both the surfaces and the bulk. Furthermore, HR images sensitive to the surfaces can be obtained in a TEM equipped with a secondary electron detector[21].

2.2.1 Surface Patterns

Various reconstructed surfaces on (001)-oriented $SrTiO_3$ crystals produced under different annealing conditions, were reported via different characterization techniques including STM, reflection high-energy electron diffraction (RHEED), and low-energy electron diffraction (LEED), as summarized In Table 2-1, A few atomic-level models were proposed for these structures although they are often inconsistent with others.

Table 2-1 Surface reconstructed patterns on (001) $SrTiO_3$ crystal surfaces[22]

Observed Reconstruction	Sample Preparation	Technique
(1x1)	(1) UHV, 1100 K, 60 min (2) 10^{-5} mbar O_2	AES, LEED, AFM, STM, UPS, RHEED, MEIS
(2x1)	(1) 10^{-5} mbar O_2 (2) UHV, 950 ℃, 2 h (3) UHV, 600-800 ℃, 30 min (4) Pure O_2, 950-1000 ℃ [23]	LEED, AES, STM, **TEM**[23]
(2x2)	10^{-5} mbar O_2	LEED, MEIS, AES, RHEED, UPS
c(4x2)	(1) 10^{-5} mbar H_2, 950 ℃, 2 h (2) UHV, 1200C, 15 min [24] (3) air or O_2, 850-930 ℃ [25]	LEED, AES, STM, **TEM**[25]
c(6x2)	(1) O_2, 1100 ℃, 3 h, followed by UHV, 950 ℃, 2 h (2) air or O_2, 1050–1100 ℃ [26]	LEED, AES, STM, **TEM**[26]
(6x2)	O_2, 1100 ℃, 3h, followed by UHV, 950 ℃, 2 h	LEED, STM
√5)x√5 R26.6˚	(1) UHV, 900 ℃, 15 h, then flashing at 1200 ℃, 2 min (2) UHV, 830 ℃, 120 min	RHEED, XPS, STM, LEED
√13x√13 R33.7˚	UHV, 1250 s,	STM

The oxygen deficiency model states that a wide range of oxygen deficient intermediate phases form, and are periodically aligned to achieve observed surface patterns. V_O-Ti^{3+}-O complexes, first reported via photoelectron spectroscopy[27], were found by STM with <1 nm resolution in the case of the $(\sqrt{5}\times\sqrt{5})-R26.6^o$ reconstructions[20]. However, several theoretical studies provide inconsistent results with the STM images[28,29], suggesting the Sr adatom model, in which ordered Sr adatoms periodically sit at the oxygen fourfold site of a TiO_2-terminated layer[30]. No conclusive experimental evidence was published due to the limited ability of the existing characterization techniques. As a consequence, the lack of accurate initial approximate structure solution leads to slow improvement through simulations and further refinements.

2.2.2 TEM Studies

The use of TEM for the purpose of providing HR information on surface reconstructions is rather limited as the key pioneering studies have been carried out mainly through diffraction techniques.[23,25] In reciprocal space, the periodicities of surface patterns give rise to superlattice diffraction spots, which are typically much weaker than the Bragg diffraction spots from the bulk of the crystal. A set of plausible atomic models can be fitted to observed qualitative diffraction measurements, however, the ubiquitous "phase problem", which describes the lack of phase information in the Fourier transform from reciprocal space to real space, remains a fundamental hurdle with this approach. Additionally, the surface reflections provide no depth sensitivity since the diffraction is just the projections of reconstructed surfaces. Furthermore, a quantitative interpretation of diffraction patterns requires precisely calibrated detectors and consideration of possible non-linearity in measurements of intensities and strict control the thickness of specimens in order to minimize dynamical effects of diffraction or full consideration of such effects with a precise knowledge of the thickness.

Alternatively, direct imaging of reconstructed surface patterns with atomic-level resolution can be achieved through profile imaging[31,32] and plan-view imaging[23]. The

former requires the reconstructed surface to be parallel to the electronic beam but with the obvious limitation from the fact that only a projection of the structure is observed. The first profile imaging approach was performed on the Au(110)-(2x1) surface under TEM mode[33]. Similar results were also published on some other surfaces such as silicon, germanium and TiO_2 crystals[32]. Conversely, when the reconstructed surface is normal to the electron beam, both surface and bulk information are integrated and recorded as plane-view images or spectra. However, correctly extracting the relatively low surface signal from images or spectra containing dominant bulk information has been a major restriction of this technique.

2.3 BULK DEFECTS: (PR, AL) IMPLANTED $SRTIO_3$

The optical properties of rare-earth doped perovskite-type oxides were actively investigated for the combination of luminescence and ferroelectricity, phase transition or semiconducting properties during the 1960s and 1970s. The observed intensity of luminescence in such systems was so low that they were not treated as a real phosphor. Nevertheless, the optical spectrum was used as a probe of physical properties of the host crystal. For example, the vibronic structure in the luminescence spectra and decay characteristics[34] of Pr^{3+}, Eu^{3+} or Tb^{3+} in $BaTiO_3$ and $SrTiO_3$ powders was studied with a goal of investigating the electron-phonon interaction[35].

In 1994, a strong red luminescence from $CaTiO_3$:Pr^{3+} was obtained, and then considered as a potential red phosphor for display applications[36]. Toki et al.[37] also reported $SrTiO_3$:Pr^{3+} shows red cathodoluminescence with an efficiency as high as 0.4 lm/W at 400 V and an acceptable efficiency at low voltages even below 10 V. Additionally, the light emitted from $SrTiO_3$: Pr^{3+} has excellent color purity with the CIE chromaticity coordinates* of x=0.670 and y=0.329, which is close to the 'ideal red'. This perfect color indices and acceptable efficiency at low accelerating voltage make Pr-doped perovskite-

* The CIE chromaticity diagram, created by the International Commission on Illumination (CIE), defined the chromaticity of a color by two parameters x and y derived from all three tristimulus values.

type oxides potential phosphor candidates under low-energy electron excitation, which would be the solution of a key limitation for the next-generation flat panel displays, e.g. field emission displays and vacuum fluorescent displays. Furthermore, $SrTiO_3:Pr^{3+}$ can be turned into a bright phosphor if a small amount of selected elements, e.g. Al [38], Ga [38,39], In, Mg [40], Zn [40] Ba [41], Ca [41], La and Li [42] are added in during the synthesis of phosphor powders. (Figure 2-1(a)) Similar increased efficiency phenomena were also reported in other rare-earth doped perovskite-type oxide powders such as $SrTiO_3:Tb^{3+}$, $CaTiO_3:Pr^{3+}$ and $CaTiO_3:Tb^{3+}$ [43].

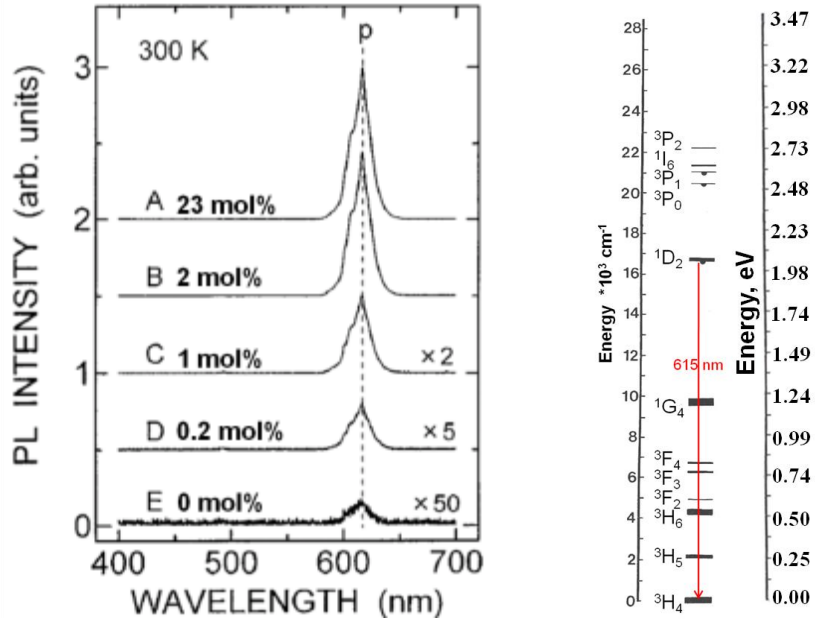

(a) (b)

Figure 2-1 Photoluminescence spectra of $SrTiO_3:Pr^{3+}$ (Pr^{3+}: 0.2 at.%) with various molar ratios of Al under the 325-nm laser excitation at room temperature. The central wavelength of 616 nm corresponds to intra-4f emission from the excited-state $^1D_2$ to the ground-state $^3H_4$ of Pr^{3+} ions as shown in (b).[44]

2.3.1 Emission Mechanism of $SrTiO_3:Pr^{3+}$

In $SrTiO_3$ crystals, an electron in the 2p valence bands of oxygen ions is (photo)excited to the 3d conduction band of titanium ions, as a result of creating a self-trapped exciton (STE) and/or transferring to a defect level. The energy is released by

emitting a visible photon. However, the details involved in the above processes are not fully understood.

2.3.1.1 Energy Absorption

The energy absorption process occurs mainly within the $SrTiO_3$ lattice since the effect of Pr and/or Al ions on the energy absorption process is negligible according to an X-ray absorption spectroscopic (XAS) study[45]. During the energy-absorption process, the uniaxial vibration of Ti ions along the Ti-O bond in a TiO_6 octahedron plays an essential role. The vibration of Ti ions was confirmed in a $SrTiO_3$ crystal after absorbing a UV photon during the photo-induced phase transition[46].

2.3.1.2 Energy Release

In Pr-doped $SrTiO_3$, the energy originally from the UV photon is transferred to the Pr^{3+} ions which subsequently release a red photon via the intra-4f transitions from the excited-state $^1D_2$ to the ground-state $^3H_4$.[44] (see Figure 2-1(b) for the energy sequence of the spectroscopic levels) During the above emission process of Pr^{3+} ions, two key processes are involved in: (a) the intra-4f transitions which are parity forbidden by the Laporte rule[†] and (b) the quenching of $^3P_0$ luminescence since Pr^{3+} ions in oxides offers either greenish-blue luminescence from the $^3P_0$ level or red luminescence from the $^1D_2$ level.

The occurrence of intra-4f transitions strongly depends on the crystal field around them; in detail, the transitions are forbidden when rare-earth ions occupy centrosymmetric lattice sites and are allowed when the ions occupy non-centrosymmetric sites[47]. In Pr-doped $SrTiO_3$, Pr^{3+} ions are expected to preferentially locate at the centrosymmetric Sr sites, resulting in weak intra-4f transitions. In contrast, the strong

[†] The Laporte rule is a spectroscopic selection rule formally-stated as the following: electronic transitions that conserve parity – i.e. g (gerade) →g, or u (ungerade) →u respectively – are forbidden in a centrosymmetric environment.

emission observed at room temperature in Pr-doped $BaTiO_3$ and $CaTiO_3$ are due to the non-centrosymmetric Ba sites in $BaTiO_3$ and Ca sites in $CaTiO_3$.

In oxide-based lattices, the quenching of $^3P_0$ luminescence can be achieved via a few possible non-radiative de-excitation pathways[48]: (a) relaxation through phonons (named as multi-phonon relaxation), (b) cross-relaxation within clusters of Pr^{3+} ions and (c) relaxation through either low-lying 4f levels hybridized with 5d levels (labeled as $4f^15d^1$ levels) or Pr-to-metal charge transfer state (CTS) (also called inter-valence charge transfer state (IVCTS)). The rate of multi-phonon relaxation is very low (e.g. $550\,s^{-1}$ in $CaTiO_3$ [49]) and leads to very little contribution. Due to the very low concentration of Pr^{3+} ions, the effect from cross-relaxation is negligible.[49] Therefore, the relaxation occurs through either low-lying $4f^15d^1$ bands only when the high-lying intra-4f levels are close in energy to these $4f^15d^1$ bands or Pr-to-metal CTS requiring possibly-oxidized host ions[50]. In $CaTiO_3$: Pr^{3+}, the existence of Pr^{4+} was reported[49] from optical and EPR characterization, as a proof of the low-lying $Pr^{3+/}Ti^{4+} \leftrightarrow Pr^{4+}/Ti^{3+}$ CTS relaxation pathway. The energy position of the Pr-to-metal CTS relates to the 'optical electronegativity' $\chi_{opt}(M^{n+})$ of the ions and the distance of Pr^{3+}-M^{n+} [51,52]. However, the existence of Pr^{4+} was in doubt[53] in $CaTiO_3$:Pr^{3+}, $BaTiO_3$:Pr^{3+} and $SrTiO_3$:Pr^{3+} systems, instead, electron-trapping states are present, especially in $CaTiO_3$:Pr^{3+}.

2.3.2 Increased Efficiency Mechanisms

Several mechanisms explaining the resultant high efficacy from co-doped elements have been reported. The well-known one is the charge compensation mechanism involving the improvement of crystallinity and the change of local crystal field around Pr^{3+} ions. The additional ions, e.g. Al^{3+} ions, preferentially substitutes Ti^{4+} around Pr^{3+}, in order to compensate the charge difference between Pr^{3+} and the host Sr^{2+}, which, as a consequence, changes the local crystal field around Pr^{3+} ions and suppresses the generation of defects[37]. The defects, working as non-radiative centers, were reported[38,54,55,56] as (a) point defects caused by the extra positive charge of Pr^{3+} at Sr^{2+} sites; (b) SrO planar faults. The appearance of forbidden intra-4f transitions reflects the

symmetry breaking of Pr-occupied lattice sites[57]. The importance of the above symmetry breaking effect can also be proved in systems with non-centrosymmetric sites. Although a few studies reported slight improvement in light emission following the addition of elements such as Al and Mg on the red luminescence in $CaTiO_3:Pr^{3+}$ system[58,59], others studies claimed that even an amount of 0.1-0.2 mol% Al or Mg results in a decrease of the red-emission intensity[53].

The above charge compensation mechanism has presumed that Pr^{3+} ions locate at Sr-sites and co-doped elements substitute at Ti-sites. In order to occupy a particular lattice site, the substituting ion should match the host ion in both the ionic radius and charge. In principle, the ionic radius of Pr^{3+} (0.101 nm) and La^{+} (0.106 nm) are close to that of Sr^{2+} (0.113 nm). On the other hand, the ionic radius of Al^{3+} (0.050 nm), Ga^{3+} (0.062 nm), Zn^{2+} (0.074 nm), Mg^{2+} (0.065 nm) are similar to that of Ti^{4+} (0.068 nm). Experimentally, Ga ions were confirmed at Ti-sites by an extended X-ray absorption fine structure (EXAFS) analysis[60]. However, several RE ions have amphoteric behaviors and are found at both A-sites and B-sites in ABO_3 oxides, e.g. Sm^{3+} replace Ba^{2+} and Ti^{4+} in $BaTiO_3$ [61]. The occupied site is affected by the A/B ratio, as reported in an ESR study on the site occupancy of Ga^{3+} ions in $BaTiO_3$ [62]. In a word, even under the assumption that the rare-earth and co-doped ions sit in the right sites, it is still hard to explain why the co-element concentration, offering the best luminescence, is not the one required for just compensating the charge difference.

Another possibility of the increased efficacy comes from the energy transfer mechanism[38], whereby Al^{3+} ions form traps which provide free carriers and enhance the carrier flow rate from the host to the activator Pr^{3+} ions. A small number of electrons in $SrTiO_3$ generated by substituting La for Sr, Nb for Ti, or by introducing oxygen vacancies (V_o)[63], recombine with holes in an in-gap state, resulting in the room-temperature blue light under UV irradiation[8,64], which should be quenched at room temperature in pure $SrTiO_3$.[65]

Last but not least, such enhanced luminescence can also be attributed to the formation of secondary nano-particles and associated interfacial defects[66], which occur in

samples with much higher Al concentration as compared to the real phosphor. Additionally, the authors[43,44,54,55] did not consider the local composition variations within the microstructure and did not explain the optimal Al concentration leading to the best luminescence.

In summary, people have proposed different mechanisms to explain the enhanced luminescence by co-doped elements. However, no clear understanding of rare earth luminescence is available due to the lack of direct experimental evidence of the type of defects and local chemistry. What is the site occupancy of the RE ions and co-doped ions such as Al^{3+} in $SrTiO_3$ lattice? How does the Al^{3+} ion associate with the Pr^{3+} ion? What is the change of the local electronic structure? How do these changes result in high luminescence? To answer the above questions, we need to investigate the local distribution and local environment of the Al and Pr dopants within the $SrTiO_3$ lattice.

2.3.3 Introduction of RE ions in $SrTiO_3$

Compared to doped powders reported in the research literature, doped single crystals have less interference from other structural factors such as grain boundaries and particle size effects. This also facilitates the structural characterization and further analysis in a TEM. Amongst many physical and chemical techniques able to introduce foreign atoms into materials, ion implantation attracts a lot of interest as a non-equilibrium method to alter the near-surface properties of single crystal wafers and to synthesize non-equilibrium compositions as well as compositionally graded materials. This method is widely applied to almost all types of materials despite the fact that it was traditionally used for semiconductors and metals[67,68].

The responses of materials to ion implantation are complex and depend on the combination of hosts, dopant atoms and implantation conditions (e.g., temperature, dose, dose rate etc). In general, two regions (implanted and un-implanted) can be identified in implanted materials and a damaged layer is usually found on the surface of the implanted material. In insulating materials (as in the cases in the present project), radiation damage processes can usually be categorized into: (a) electronic processes; (b) nuclear or elastic

collision processes; and (c) radiolysis or photochemical processes. Electronic processes refer to the change of electronic or charge states due to the deposited energy. Nuclear or elastic collision processes are in the form of displacement damage. Radiolysis processes describes the creation of atomic or ionic defects initiated due to electronic excitation.

Three mechanisms have been extensively used to modify the near-surface properties of optical materials by creating functional defects such as V_O (e.g. in $SrTiO_3$ crystals[8]), introducing special dopants, and generating precipitates such as Au nano-particles[69].

2.3.3.1 Ion Implantation

Previous studies were carried out on the optical properties of Ar^+ [8], N^+ [70], Au^+ [71,72,73] and Sb^+ [71] implanted $SrTiO_3$, irradiation-induced epitaxial re-growth of the amorphous layer with He^+, Ne^+, Ar^+ [74] and Si^+ [75], damage accumulation and/or recrystallization from He^+ [76], Ne^+, Kr^+, Xe^+ [77], Au^+ [78] and Pb^+ [76,79], surface modification with Ga^+ [80] and magnetic behaviors following implantation with Co^+ [81] or Mn^+ [82].

Based on studies on $SrTiO_3$ crystals implanted with heavy ions, a non exhaustive list of parameters for implantation and post-annealing is presented in table 2-2. In order to avoid phase transitions of the host crystal during implantation, the implantation experiments were generally carried out above the phase transition temperature (108 K). To amorphize $SrTiO_3$ crystals, much higher implantation damage is required above 400 K[77,79], as shown in the critical dose v.s. implantation temperature graph (Figure 2-2).

Table 2-2 Summary of parameters used in heavy ion implantation and post-annealing for $SrTiO_3$ (100)

Dopants	Implantation				Post-annealing		
	Energy / keV	Temperature / K	Dose / cm^{-2}	Depth Amorphous	Temperature /K	Time	Atmosphere
Pb [68]	540	125	$1x10^{15}$	1800 Å	673	0.5h	air
Au [83]	250	628	$3\sim5x10^{16}$	-	978	5min	N_2
Nb [84]	150	298	$10^{14}\sim10^{17}$	-	-	-	-
Au[73]	2000	975	$1.4x10^{17}$	-	1275	10h	air

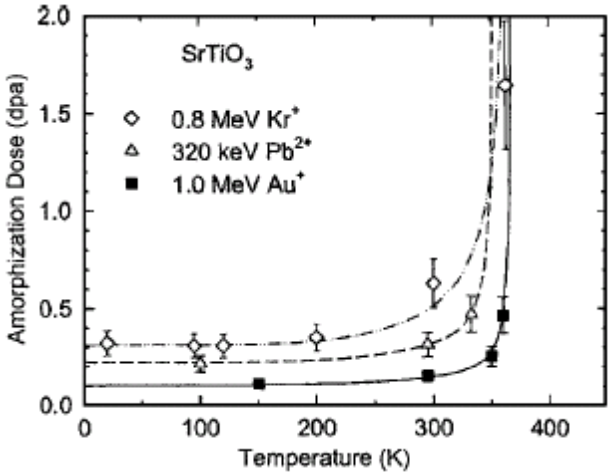

Figure 2-2 Amorphization dose (displacement per atom) v.s. temperature to achieve a relative disorder level of 0.97 in $SrTiO_3$ [78]

2.3.3.2 Damage Recovery

In order to remove the damage and achieve (meta-)stable structure, post-annealing is always carried out after implantation. The material behaviors during the heat-treatment depend on several key factors such as time, temperature and atmosphere, as well as the crystallographic plane of the surface[68]. Other annealing techniques such as rapid heating and cooling are introduced to obtain a perfect crystal without causing significant diffusion of injected ions.

Although the temperature at which full thermal recrystallization occurs is generally not agreed upon, the complete epitaxial crystallization of the ion-damaged amorphous $SrTiO_3$ crystals with (001) surfaces have been obtained at 400 ˚C for 30 min in air[68]. The new crystal retains the original crystal orientation although a high density of dislocations appears in the re-crystallized regions. After an "incubation" period, the growth velocity, defined as the rate of change in recrystallized depth, is constant. The initialization period has an inverse relationship with the annealing temperature, and is almost non-detectable above 350 ˚C. During the linear growth period, the growth rates for thermal re-crystallization can be described as

$$v(T) = v_{th} \exp\left(-\frac{Q}{RT}\right) \qquad \text{Equation 2-1}$$

In which, v_{th} (=0.05 cm/s [67]) is a prefactor for thermal epitaxial regrowth, Q (=0.77 eV in air[67] or 1.2 eV in N_2 [85]) is the activation energy, R is universal gas constant and T is temperature. The thermal re-growth kinetics for (111) surface is reported to be different than the ones for (001) and (011) surface[68]. There are no well-behaved and reproducible results in the literature for the former cases[68], which indicates the complexity of recrystallization process.

In many potential applications of $SrTiO_3$, such as cathodoluminescence phosphors and nuclear waste disposal hosts, the understanding of the dynamic recovery and nanostructure evolution under irradiation is critical. Ion-amorphized $SrTiO_3$ by heavy injected ions exhibits strong epitaxial recovery at the amorphous/crystalline interface under an electron beam with a dose on the order of 10^{20} $cm^{-2}s^{-1}$, common conditions for TEM observations[86]. The recrystallization behavior shows a strong dependence on the electron beam flux. One of the parameters that is important to understand the recrystallization behavior is the effect of local temperature and the contribution of the electron beam to temperature changes. The temperature rise under electron beam irradiation was estimated to be a few degrees[87], thus can be negligible. The maximum energy transferred from the probe electron to the target atom is much lower than the threshold displacement energies in oxides[88]. The beam-assisted re-crystallization process is probably due to the ionization-induced processes, e.g. localized electronic excitations, which may lower the energy barrier by disturbing local atomic bonds and structure. It should be noted that the beam-induced effect on the sample is still not well understood, particularly with a finely focused and thus high dose density beam.

2.4 CHALLENGES IN CHARACTERIZATION OF DEFECTS AND LOW-DIMENSIONAL STRUCTURES

The complete characterization of defects and low-dimensional defects in a host matrix, including elemental identification and determination of local atomic configurations, provides new insights in many fields of materials science, physics and nanotechnology while remaining as an open and very challenging topic. Traditionally, the changes of physical and chemical properties of a bulk with or without defects are used as the means to reveal the distribution and average local environment of defects, i.e. photon absorption and electron spin resonance (ESR, also known as electron paramagnetic resonance (EPR)).

The breakthrough of imaging individual atoms first appeared in surface science. The very first atomic structure images of metal surfaces were obtained by field-ion microscopy (FIM)[89] but with very tough requirement in terms of the sample as a sharp needle-shaped specimen is necessary. Atomic force microscopy (AFM) and scanning tunneling microscopy (STM) not only form images of the surface (potentially at atomic resolution) but can also position single atoms on the surface of a flat specimen[90,91]. Chemical identification of individual surface atoms by AFM was recently achieved indirectly through the comparison between AFM images and the force value computed from large-scale density functional theory simulations.[92] Compared with the above techniques, HR TEM is an essential tool potentially capable of accessing the local distribution and environment of dopant atoms because of its ability to directly image at sub-Ångstrom resolution[11] and execute various spectral techniques[9] at high spatial resolution, with the EELS method approaching today few tens of meV energy resolution[93,94].

In order to verify whether the detected weak contrast is from a single impurity atom or not, three quantitative tests are proposed by Voyles et al.[95]: 1) concentration test, i.e. the number of atoms in images should be consistent with the concentration of other independent measurements; 2) intensity test, the observed intensity should agree with a

model considering their spatial distribution and relevant contrast mechanism; 3) null test, no intensity appears in a null bulk under the same imaging conditions.

2.4.1 STEM Mode

The development of scanning TEM (STEM) provides a new possibility to directly image and chemically identify individual defects on the surface and in the bulk. The successful application of annular dark-field (ADF) to image heavy atoms, i.e. U and Th atoms lying on a very thin amorphous carbon film, was first reported by Crewe[96] in the 1970's. In order to remove the strong dynamical diffraction occurring at lower collection angle, high-angle ADF (HAADF) images (Z-contrast images) were used to successfully detect individual Pt atoms on crystalline γ-Al_2O_3 support material[97].

The characterization of (point) defects inside a bulk material seems much more challenging because of much weaker contrast from the atomic column containing only one foreign atom compared with the neighboring atomic columns containing typically a few tens, up to a few hundred atoms in typical samples. The first successful demonstration of ADF imaging single atoms in a bulk was reported in Sb-substitutional n-type bulk silicon[10]. To increase the contrast from the extra-Sb atom, chemical-mechanical polishing and etching techniques were applied to achieve a clean surface and further reduce the thickness of the specimen to less than 5 nm (i.e. approximately 26 atoms). In their HAADF images, Voyles et al[10] showed that Sb-containing columns appear as bright dots compared with the neighboring unoccupied columns. Besides substitutional dopants, HAADF images were applied to image various defect configurations of single Au inside Si nanowires[98], such as tetrahedral interstitial, hexagonal interstitial and buckled Si-Au-Si chain configurations.

One of the main disadvantages is that all TEM images are 2D projections of 3D objects since TEMs have a huge depth of focus (>1 mm depending on the operating conditions) compared to the thickness of thin foils (~100 nm). However, HAADF images taken under large convergence angle have depth sensitivity, which can be applied to investigate the depth distribution of defects. Accordingly, the contrast contributed by La

atoms at different depths within γ-Al_2O_3 is different in images taken under different defocus conditions[18].

Low-angle ADF (LAADF) images, acquired synchronously with ADF or HAADF images, are much more sensitive to the de-channeling of probe electrons, as a likely result of local phonon modes or strain fields around defects. Accordingly, Muller et al.[99] applied LAADF images to detect oxygen vacancies (V_O) and revealed their distribution in $SrTiO_3$ crystals.

2.4.2 TEM Mode

In order to improve the spatial resolution and extend the information limit under TEM imaging conditions, the contrast transfer function of a microscope can be taken into account by the exit wave reconstruction (EWR) method through the use of a series of images obtained at different defoci (also known as the focal series reconstruction technique) so that the aberration of the microscope can be accounted for. The EWR method was successfully applied to image one-dimensional crystals formed within single-walled carbon nanotubes[100]. It should be noted that beside the complex calculation involved in the reconstruction processes, the requirements for TEM specimens and equipment stability are quite strict for this method: samples have to be extremely stable mechanically and structurally and the microscope must provide extreme electronic and mechanical stability

Other alternative methods include the hardware modification of the transfer function of a microscope by the insertion of spherical aberration correctors that allow the reduction and adjustment of the spherical aberration coefficient value (C_s), directly resulting in an improvement of the interpretability of the images and dramatic reduction of delocalization in the images. Using negative C_s values, the detection of oxygen atoms[101] and oxygen vacancies[102] in perovskite structure has been achieved.

2.4.3 Spectroscopy

TEM not only offers direct insight to defects, but also provides local chemical information from electron energy-loss spectroscopy (EELS) or energy dispersive X-ray spectrometry (EDX). The detection of single Gd atoms from EEL spectra was first reported[103] with a spatial resolution of ~0.6 nm, which was mainly determined by the size of probe[104]. The above spatial resolution is too low to resolve the atomic structure of most systems. With a much smaller probe, single atom spectra from La dopants in $CaTiO_3$ lattice[105] were reported, which suggests the wide application of EEL spectra for detecting individual defects in most systems.

EEL spectra can be applied as an indirect method to detect vacancies. The detection limit for V_O in $SrTiO_3$ could be achieved at a level of ~0.05 (~1 at.% V_O) determined by the ratio of Ti^{3+}/Ti^{4+} calculated from the associated EEL spectra in $SrTiO_3$ crystals[99].

Although a few exciting experimental results have been reported, more limitations still challenge our ultimate goals: not all dopants, even heavy atoms, are visible in all local configurations[106]. Due to the integrated signals contributed by both defects and the bulk in a TEM, the enhancement or isolation of the signals from defects is usually demanded.

CHAPTER THREE

SPECIMEN SYNTHESIS AND CHARACTERIZATION TECHNIQUES

The starting materials are $SrTiO_3$ single crystal wafers with the dimensions of 10x10x0.5 mm ±0.05 mm, orientation of (001) ± 0.5°, which were purchased from MTI Corporation. One surface of these single crystals is "EPI-quality" polished by the chemical mechanical polishing (CMP) technology with less sub-surface lattice damage. At the beginning of this chapter, synthesis techniques necessary to create low-dimensional defects in a $SrTiO_3$ crystal are presented. Following that, the experimental techniques are presented including luminescence tests and structure characterization. Finally, some theoretical methods are introduced, which are used to analyze our obtained experimental dataset.

3.1 Synthesis of Reconstructed Oxide Surfaces

TEM specimens with surface reconstruction were prepared through a similar approach to that described in Erdman et al.[25]. The plan-view TEM specimens were obtained through low angle polishing (Multi-Prep#) followed by ion milling (Details are discussed in section 3.4.1). Subsequently, the TEM specimens were annealed at 800-1200 ˚C in air in a tube furnace for 1 hr to create surface patterns. During the annealing process, the TEM specimens were located on a $SrTiO_3$ wafer in an alumina annealing boat. The resulting surface patterns have a strong dependence on the annealing temperature, which will be discussed later.

3.2 Synthesis of Implanted Oxides

Ion implantation was applied as a surface modification method of single crystals with precise control of the dose, impurity depth and species. Although the resulting structure of implanted materials always includes a damage layer, a post-annealing treatment can be carried out to remove this damage.

3.2.1 Ion Implantation

The implantation process involves energy loss from the high-energy injected ions in the host, resulting in displacement or/and ionization of the host atoms. Generally, light ions or ions at higher energy support more electronic stopping, while heavier ions or ions at lower energy offer more nuclear stopping. Due to the complexity of such processes, “stopping and range of ions in matter” (SRIM) simulations were performed to assess the interaction between the injected ions and the host atoms based on individual cases.

Several parameters involved in implantation are user-controlled: dose, referred to the concentration of the final product, and usually linked to the damage of hosts; energy,

involving the implantation depth; temperature, related to the final damage of the substrates.

3.2.1.1 Implantation Energy

Injected ions are favored to go deeper under a higher implanting energy, thus more ions are expected to be introduced into the crystalline layer, the main region of interest in the present project. The energy of implanting heavy Pr^+ ions is limited by the implanter to be lower than 35 keV. To match the concentration profiles of Pr^+ ions implanted at 35 keV, the optimized implanting energy for light Al^+ ions is 15 keV according to SRIM simulations. (Table 3-1 and Figure 3-1 (a))

Table 3-1 The projected range of Pr^+ and Al^+ at various energy in $SrTiO_3$

Ions	Energy/keV	Projected Range /Å	Longitudinal Straggling /Å	Lateral Straggling / Å
Pr^+	35	134	49	37
Al^+	5	63	42	30
Al^+	10	109	68	49
Al^+	15	154	93	67
Al^+	20	199	116	85
Al^+	25	244	140	101

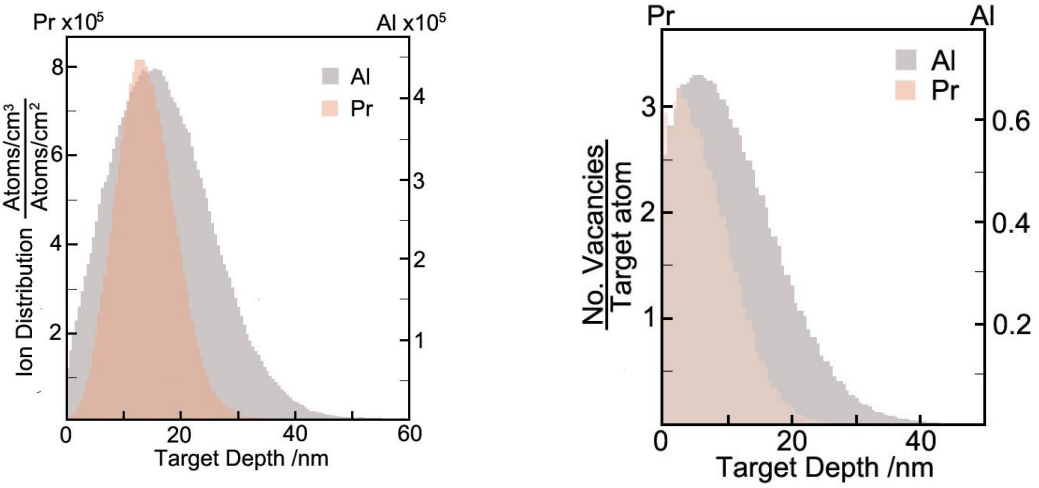

(a) Ion distribution (b) Damage

Figure 3-1 SRIM simulation of Pr implanted at 35 keV and Al implanted at 15 keV based on 100,000 ions simulation

3.2.1.2 Implantation Dose

According to the research literature, a Pr concentration of about 0.2 at.% can optimize the luminescence from $SrTiO_3$:Pr/Al. The Al concentration was selected in the range of 2 at.% to 15 at.%. In order to isolate the effect from Pr^+, study the damage recovery processes and facilitate TEM characterization, specimens implanted only with high Pr concentration were produced to have the same damage computed by SRIM compared to (Pr, Al) co-implanted specimens. (Figure 3-1(b))

The dose of injected ions is calculated based on the known concentration according the following equation,

$$\phi = \int_0^\infty C(x)dx \qquad \text{Equation 3-1}$$

In which, *C(x)* describes the concentration profile with the unit of number of atoms/cm^3 and φ stands for the dose with the unit of number of atoms/cm^2. Under the Gaussian approximation of implant profile,

$$C(x) = C_P \cdot e^{\frac{-(x-R_P)^2}{2(\Delta R_P)^2}} \qquad \text{Equation 3-2}$$

Where, C_p is the constant determined by the peak concentration. R_P and ΔR_P are the projected range and longitudinal straggle, respectively. They describe the profile shape, and are different for different systems under different implantation conditions. In the present project, they are evaluated via SRIM simulations. (Figure 3-1(a))

In summary, Pr^+ ions were implanted in EPI polished surfaces of (001) $SrTiO_3$ single crystals at an energy of 35 keV and a dose of $7x10^{13}$ cm^{-2} at room temperature (RT). The peak concentration of Pr^+ ions is estimated to be 0.2 at.% in the region of 10-20 nm depth. The Al^+ ions were implanted subsequently at 15 keV with doses of $8.5x10^{14}$ cm^{-2}, $3.8\ x10^{15}$ cm^{-2} and $6.3x10^{15}$ cm^{-2} at RT. Similar concentration profiles of Al^+ ions should therefore be achieved with peak value of 2 at.%, 9 at% and 15 at.%, respectively.

As for the second series, Pr^+ ions were implanted into (001) $SrTiO_3$ single crystal at an energy of 35 keV and doses of $7x10^{13}$ cm^{-2}, $2.8x10^{14}$ cm^{-2} and $9.8x10^{14}$ cm^{-2}. The corresponding peak concentration of Pr^+ ions are thus 0.2 at.%, 0.8 at.% and 2.8 at.%,

respectively. The computed damage caused by Pr^+ ions at doses of $2.8x10^{14}$ cm^{-2} and $9.8x10^{14}$ cm^{-2} matches the ones in the first series with additional Al^+ ions co-implantation at a dose of $3.8\ x10^{15}$ cm^{-2} and $6.3x10^{15}$ cm^{-2}, respectively. Furthermore, Al^+ ions at a dose of $8.5x10^{13}$ cm^{-2} (0.2 at.% peak concentration and $8.5x10^{14}$ cm^{-2} (2 at.% peak concentration) at 15 keV were implanted into the pre-Pr implanted specimens with 0.2 at.% peak concentration as controls for the second series of implantation.

3.2.1.3 The Control

In order to evaluate the implantation processes, silicon single crystal wafers were used as reference test materials on account of their well-known structure. Additionally, compared to the present $SrTiO_3$ lattice, Si substrates are suitable for TEM characterization of single dopant atoms due to the large Z-difference between the dopant and host atoms. Thus, implantation tests in (011) Si wafers were carried out under the same conditions as used for the $SrTiO_3$ wafer. The peak concentration of dopant ions in Si is within the region of 25-35 nm depth compared to 10-20 nm depth in $SrTiO_3$ lattice from the SRIM calculation.

3.2.2. Post-implantation Treatment

Several issues should be taken into account when designing the heat-treatment of implanted oxides:

a) To fully recover the surface damage caused by implantation, 330˚C is reported[68,85] to the lowest temperature (lower limit) for recrystallization.

b) To long-range thermal diffusion of injected ions, a low annealing temperature or a short annealing time is thus required.

c) To form nano-clusters, long-range diffusion must be involved, which requires high annealing temperature and long annealing time.

d) To avoid the surface reconstruction, high temperature annealing should be avoided, which determines the upper limitation of temperature.

e) To avoid new oxygen vacancies caused by annealing, the annealing atmosphere is chosen as air.

Accordingly, to obtain oxides with fully recovered damage layer and isolated and clustered injected ions, annealing treatment of implanted $SrTiO_3$ crystals were carried out in a tube furnace at different temperatures of 400 ˚C, 700 ˚C and 800 ˚C for different time of 5 min, 60 min and 180 min in air.

3.3 LUMINESCENCE OF IMPLANTED OXIDES

In order to test the optical properties of Pr-implanted $SrTiO_3$ crystals, photoluminescence (PL) measurements were performed on the as-implanted and annealed crystals. The emissions are expected within the wavelength range of 400-900 nm. A He-Cd pump laser of 325 nm wavelength was selected as an appropriate source and the spectra in the range of 400-1000 nm wavelength were recorded to cover the whole region of interest. The PL tests were run at room temperature in a dark room to minimize the effect from the room light. To minimize the statistical errors, the final spectra were the average of 5 original scans with scanning time of 30 s each.

3.4 TEM CHARACTERIZATION

The microstructure of $SrTiO_3$ single crystals, with certain low-dimensional defects including reconstructed surfaces as well as injected Pr^+ and Al^+ ions and the subsequent defects caused by implantation, was characterized under TEM.

3.4.1 Sample Preparation for TEM

In order to satisfy different requirements for TEM characterization, several methods of preparing specimens were used. With the purpose of introducing ex-situ/in-situ annealing on TEM specimens, the conventional method was applied to create plan-

view specimens. A 3 mm disk was cut from single crystal wafers mechanically polished to a thickness of 150-180 μm via an ultrasonic cutter, and then was dimpled to a central thickness of 10-20 μm, finally ion milled to electron transparency with 4 keV Ar^+ ions at 6-8°. The above approach avoids the use of glue, which limits the high-temperature annealing. However, the specimens had to be ion milled for ~15-25 hrs, thus a considerably thick amorphous layer was formed on both surfaces, which could be later removed by annealing.

To reduce the ion-milling time and thus minimize the formation of surface amorphous layers, the low-angle polishing (Multi-prep#) method was selected to obtain both plan-view and cross-section specimens. Plan-view specimens were usually used as the reference to provide bulk information, while cross-section samples were mainly prepared to investigate the implanted layer. Implanted oxide wafers were cut into 5x1.5x~0.5 mm slices using a wire saw, which ensures minimal damage to the cutting surface. Two slices with implanted layer face-to-face were glued together with standard quick setting epoxy. Thus, 5x1.5x1 mm sandwich blocks were obtained and ready to cut into pieces of dimensions about 1x1.5x1 mm. A block with 1x1.5x1 mm was polished via an Allied MultiPrep™ equipment on one side to get a mirror finish. The block was glued onto a TEM wedge thinning paddle with shiny side down and then polished down to the thickness of 300 μm with polishing papers of 15 μm, 9 μm, 6 μm and 3 μm sized particles, a load of 200 grams and water as the lubricant. After that, a low polishing angle of 4° was used and the wedge of the block was further reduced in thickness to 10 μm. 1 μm polishing paper with an alcohol-based lubricant (Allied Bluelube™ polishing lubricant) was used to obtain the wedge, which now has a thickness of a few hundred nanometers. Finer polishing papers of 0.5 μm were used to additionally reduce the thickness and surface damage. After polishing, the wedge specimen was glued on a molybdenum ring with standard quick setting epoxy. Finally, ion milling with 0.25-1.5 keV Ar^+ ions in a Gentle Mill™ was selected to make the specimen electron transparent, reduce the surface damage layer and remove the bright islands shown in Figure 3-2 (a), which are probably

due to the re-deposition of Si atoms by the Ar^+-beam with higher energy or residues from the lubricant.

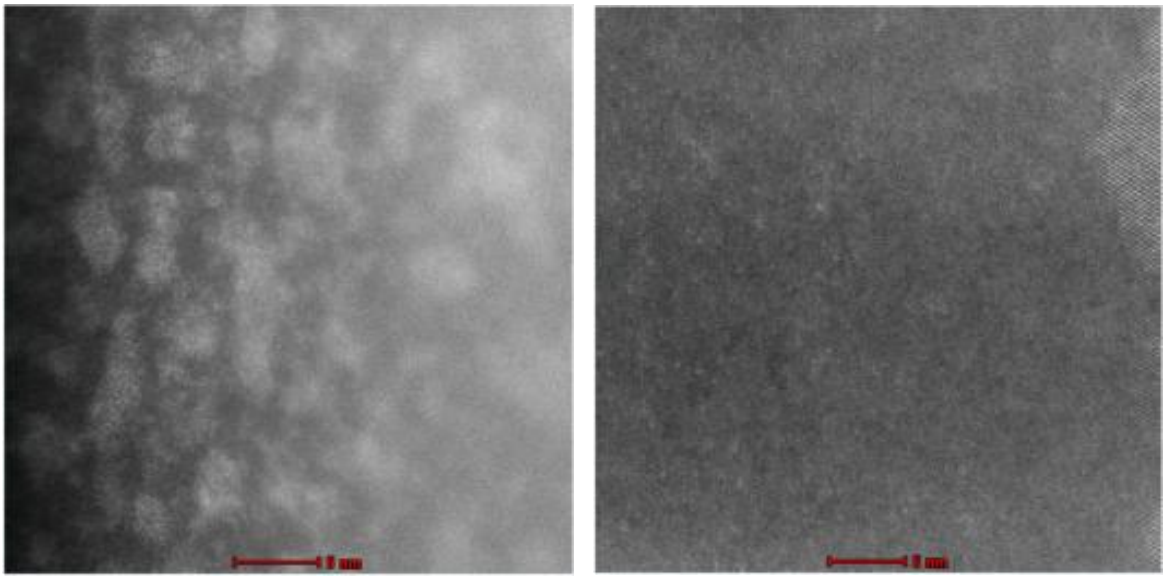

(a) (b)

Figure 3-2 Effect of low energy ion milling: (a) ion milling at 4 keV and cleaning with 1 keV, produced bright clusters probably due to the re-deposition of Si or residues from the lubricant; (b) ion milling at 1.0 keV and cleaning with 250 eV, produced sample without bright island.

3.4.2 Conventional Transmission Electron Microscopy

A conventional TEM (Philips CM12) operated at 120 keV was used to investigate the over-all view of specimens. Diffraction contrast under image mode was applied to reveal the linear and planar defects due to their crystallographic differences. Additionally, the diffraction pattern provided a way to index the associated crystallographic parameters and more crystallographic information related to different defects. Particularly for the surface reconstructed specimens, a series of negative plates with exposure times varying from 1 s to 150 s were taken to record the surface reflections.

3.4.3 High-Resolution Imaging

Detailed structural characterization was performed with scanning transmission electron microscopy (STEM) with an aberration-corrected FEI Titan 80-300 Cubed microscope. In STEM, an atomic size probe is rastered over the specimen and an (annular) detector is used to collect the signal within a defined angular range of scattering and integrates the detected signal as the intensity at the current location of the probe. Depending on the collection range with respect to the illumination cone of the probe, a few imaging techniques including high-angle annular dark-field (HAADF), low angle annular dark-field (LAADF), annular bright-field (ABF) and bright-field (BF) imaging are listed and discussed as follows.

The high-angle (HA) condition is defined when the inner collection angle (β) of the detector is at least 2-3 times the convergence angle (α) standing for the maximum angle of the illumination cone. Correspondingly, the signal contributed by diffraction is minimized. The signal collected by the HAADF detector represents the high-angle elastically scattered electrons, which is highly sensitive to the atomic number (~proportional to $Z^{1.7}$). Therefore, atomic level HAADF imaging provides direct chemical sensitive contrast plus structural information, and thus is considered as one of the most advanced techniques to characterize individual low-dimensional defects.

The low-angle (LA) ADF images are formed with the signal in the range of just outside the illumination cone, up to 2-3 times the convergence angle. On the other hand, the ABF detector is placed within the illumination cone but avoid the most intense central signals, typically with $\beta=0.5*\alpha$. The contrast in ABF images is considered mainly associated with the 1s-state channeling effect.

In practice, several parameters beside a perfect alignment of the microscope are important in order to obtain perfect HAADF images: a) camera length (CL), directly linked to the collection angle of an ADF detector; b) probe current, related to beam damage and the intensity of signals. Large collection angle is preferred for Z-contrast images but leads to lower signals. Increased probe current thus helps to enhance signals,

but may introduce beam damage; c) convergence angle (α) of the probe, the optimized α can be found through image simulation and affects the depth sensitivity.

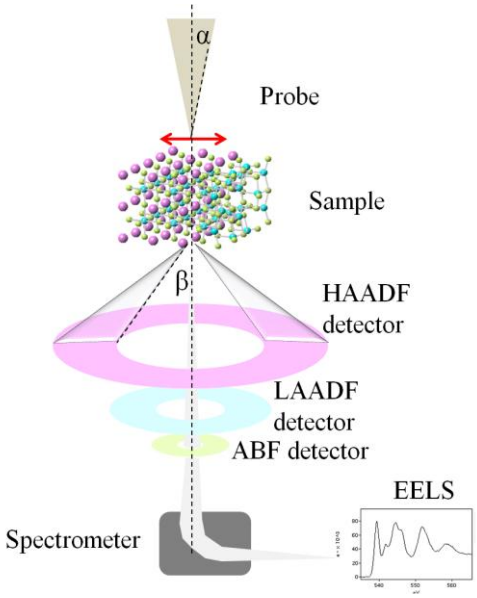

Figure 3-3 Major elements of a STEM.

Since the HAADF image only collects large-angle scattered electrons, BF image or ABF image or EELS signals can be acquired simultaneously, thus providing chemical analysis and further crystal structure information.

3.4.4 Electron Energy-Loss Spectroscopy

Electron energy-loss spectroscopy (EELS) measures the inelastic interaction between the probe electrons and a specimen. A spectrometer is used to measure the energy-loss spectrum which includes features such as phonon excitations (<0.1 eV), Cerenkov radiation (<10 eV), plasmon excitations (<50 eV), inter- and intra-band transitions (<20 eV), and inner-shell ionization (from ~50 eV, up to few keV).

A typical EEL spectrum can be summarized into the following parts: a) a sharp and intense zero loss peak (ZLP) comes from no-loss electrons and elastic scattering. The width of the ZLP is mainly determined by the energy distribution of the electron source and related optics, which represents the experimental energy resolution limitation. The

ZLP can also include phonon losses; b) a series of low-loss peaks (<50 eV), they involve plasmon excitations and the intra-band and inter-band transitions; c) several low intensity but distinct core loss peaks (>50 eV), arise from core excitation to empty states and are usually used to identify the presence of specific elements and investigate their local chemical states and coordinations.

Energy-loss near edge structure (ELNES) describes core loss spectral structure. ELNES is caused by the transitions of excited core electrons to unoccupied states and reflects the local atomic environment, such as valence, type of bonding and coordinations[107]. Therefore, ELNES features are applied as the probe to obtain the local chemical and physical environment of selected low-dimensional defects.

A parallel electron energy-loss spectrometer (Gatan 866 model) attached to an aberration-corrected FEI Titan 80-300 Cubed microscope was used to obtain the EEL spectra associated with selected low-dimensional defects in oxides. To improve the energy resolution, a monochromatic electron beam[93] is usually used as the probe, which offers an energy resolution of less than 0.1 eV.

3.5 SIMULATION

3.5.1 Multislice Method

The contrast in high-resolution images is complex and difficult to interpret, therefore, image simulation is mandatory. The image simulation used in my work is based on the multislice method with detailed explanation as follows.

The strong interactions between the incident electrons and the crystal can be precisely described by the relativisitic Schrödinger equation of electrons modified by the atomic potential of the crystal. However, it is very time consuming to obtain a reasonable accuracy and sampling. The multislice method[108] reduces such 3D problems to quasi-2D cases and makes it possible to obtain fairly reliable results for crystalline solids and near amorphous materials but with much shorter computation time. The core idea is based on

the following principles (Figure 3-4): first of all, the specimen is divided into many thin slices, and we consider the atomic potential of each slice $v_{z,n}(\mathbf{x})$; secondly, the incident wave function $\psi_o(\mathbf{x},\mathbf{x_p})$ is modified by the atomic potential layer by layer, finally the exit electron wave function $\psi_{t,m}(\mathbf{x},\mathbf{x_p})$ is calculated at the exit surface of the specimen. The simulation code was implemented by Kirkland[109] and adapted to run on a parallel computer (a 104 CPU cluster running under LINUX operating system at the Canadian Centre for Electron Microscopy) by Michael Robertson (Acadia University) on the occasion of the CCEM summer school held in 2009 at McMaster University.

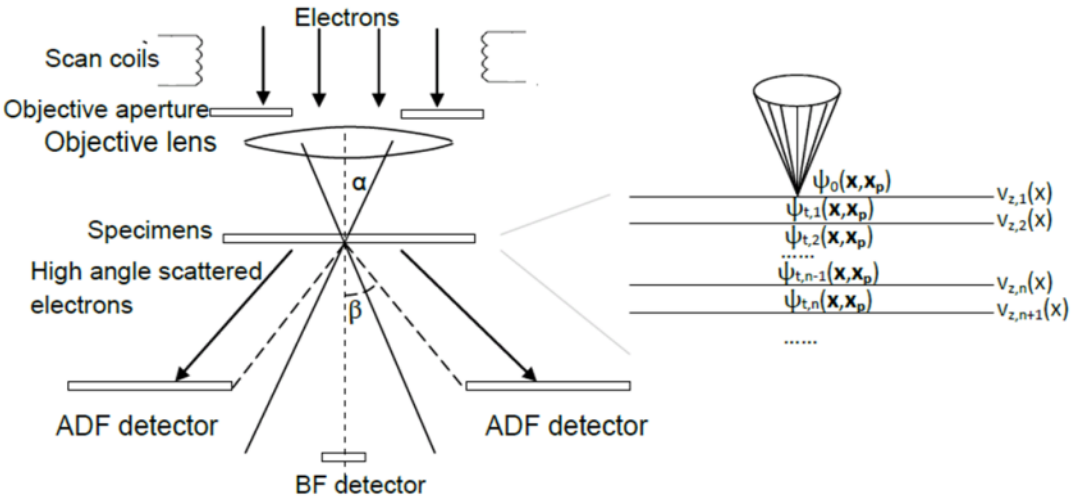

Figure 3-4 Illustration of multislice simulation.

To achieve the correct local defect configuration presenting a realistic concentration of defects, the target defect must be isolated in a large periodic unit supercell to reduce the interaction between adjacent defects. Usually, the inter-spacing between adjacent defects is about 20-25 Å.

3.5.2 Multiplet Method

The atomic multiplet method[110] implemented in the CTM4XAS program[111] is a semi-empirical approach for calculating the L- and M-edge EEL spectra of rare-earth (RE)

and transition metal (TM) elements. During the X-ray and electron absorption process, the atomic multiplet effect is manifested experimentally as a largely-screened core-hole potential experimentally, which originates from the overlap of the core wave function and the valence wave function. The intensity of the selected transition in the atomic multiplet simulation is determined by the matrix elements which accounts for the effective electron-electron interaction and spin-orbit coupling. The many-body effects in a RE and TM compound are taken into account by adding the charge-transfer effect and the crystal field effect perturbations on the atomic multiplet theory. The charge-transfer effect is responsible for bonding in ionic solids and the crystal field effect depends on the local symmetry of the core excited atom in the solid.

Crystal-field multiplets[112] theory was applied particularly for low-symmetry environments. Instead of the nonrelativistic Schrödinger equation in the previous atomic multiplet treatments, the Dirac equation has been used to calculate the central field model orbitals and energies, including spin-orbit coupling effects. In contrast to conventional ligand-field multiplet theory with freely controllable crystal field parameters, the new approach relies on a crystal field constructed numerically from the positions and formal charges of the surrounding atoms.

CHAPTER FOUR

THE EXTRACTION OF WEAK SIGNALS

The characterization of low-dimensional defects, which are impossible to be physically separated from the bulk, is essential but very challenging. Under the electron beam, signals containing all information, from both the bulk and the low-dimensional defects present, are integrated and recorded as an image or a spectrum. Owing to the fact that the electrons scattered by defects and the bulk have different distribution in space, imaging techniques such as HAADF images (Z-contrast images) and ABF images collect corresponding signals and thus can enhance the visibility of these defects. Regarding EEL spectra containing integrated signals from both defects and the bulk, we proposed a simple but entirely new experimental approach to separate EELS signals caused by defects from the ones resulting from the bulk, which is based on a 'thickness' series of plan-view spectra containing different bulk contributions.

4.1 IMAGES

As we mentioned in section 2.4.1, heavy atoms can be directly viewed from the HAADF (Z-contrast) images because of the strong scattering power of heavy atoms. However, not all heavy atoms can be seen from a low-Z background. It should be noted here that the electron energy-loss spectroscopy (EELS) technique can provide the location of dopants even when they are invisible from the simultaneously acquired images[113]. Analogous to the heavy atoms, the signals from other low-dimensional defects (light elements and vacancies) are not evenly distributed in space. Accordingly, collecting corresponding signals can enhance the contrast from other low-dimensional defects. In this section, we will discuss the visualization of low-dimensional defects from a single frame.

4.1.1 Invisible Z-contrast from Heavy Atoms

Visibility tests of heavy dopants in a HAADF image were carried out on Pr-implanted $SrTiO_3$ (001) crystals using multislice simulation, which provides a reasonable evaluation of the HAADF image contrast from a crystal along a rational zone axis. As shown in figure 4-1, I_{Pr}, I_{Sr} and I_{Ti} are defined as the intensity at the atomic column containing one Pr atom, and the intensities at the Sr and Ti-O positions respectively. The visibility of Pr atoms is quantitatively described by the intensity ratio I_{Pr}/I_{Sr} or I_{Pr}/I_{Ti}, depending on the specific lattice site occupied by the Pr atom. The Pr atom is considered to be invisible when the intensity difference between the column containing one Pr atom and the one without is less than 10%, i.e., the intensity ratio is below 1.1. Under the best observation conditions including suitable focus, convergence angle and collective angle[114], Pr atoms can only be visible in specimens with a thickness less than 2 nm, which is an almost impossible experimental achievement. In fact, we cannot directly see Pr atoms as bright spots within a $SrTiO_3$ lattice experimentally even when the Pr signals are clearly detected from corresponding EEL spectra.

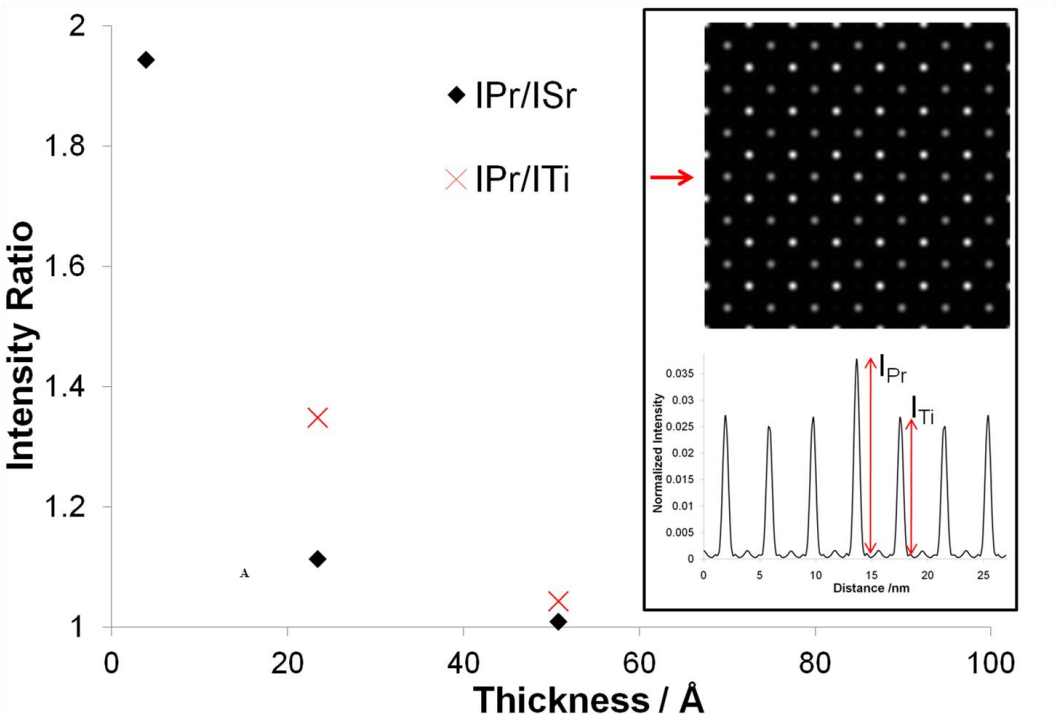

Figure 4-1 The detectability of Pr sitting in a substitutional position of Sr or Ti. The insert present the original output image from the multislice simulation under the best experimental parameters. The intensity ratio is defined from the line scanning profile contain the Pr atoms within the lattice.

The channeling effect, which acts as a microlens and focuses the probe electrons along the atomic columns, enhances the visibility of these heavy atoms but requires a certain thickness of the lattice (i.e., 5~10 nm) before reaching the heavy atom[115]. Therefore, when the atomic number difference (ΔZ) between the heavy atom and the host is small, the thickness required for strong channeling will fade the very weak contrast caused by ΔZ. Although the heavy atom can be visible within a very thin specimen without the help of channeling (Figure 4-1), a very thin specimen is extremely difficult to achieve in practice due to the very different ion-milling rates between the low-dimensional defects and the hosts. Additionally, such thin specimens are usually unstable under the electron probe.

4.1.2 Directly Imaging Light Atoms within a Heavier Lattice

Since direct imaging heavy atoms in the present $SrTiO_3$:Pr, Al system is impractical, probing other low-dimensional defects associated with the heavy atoms can offer indirect observations of these heavy atoms. Similar to the heavy atoms, the scattering of the probe electrons from other low-dimensional defects provide unevenly distributed signals in both intensity and space. The collection of corresponding signals contributed by these defects can be achieved by varying the position and shape of annular detectors. As shown in figure 4-2, the simulated ABF[‡] and LAADF images clearly indicate that Al ions should be visible as bright dots within a $SrTiO_3$ lattice.

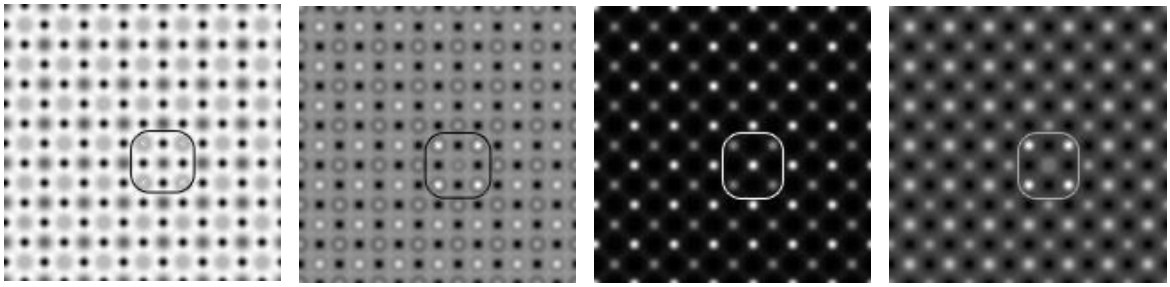

(a) 10-47 mrad (b) 15-70 mrad (c) 25-116 mrad (d) 18-37 mrad

Figure 4-2 The detectability of an Al_8 cluster substituting adjacent Ti-sites based on the multislice simulation. The simulation box has a dimension of 27x27x100 Å containing 6,370 atoms, in which four neighboring atomic columns containing two adjacent Al ions each (the four atomic columns are marked by a square). The simulation is run under 200 keV with the convergence angle of 18 mrad. The annular detector has the ratio of outer/inner angle at the value of 4.6 for (a)-(c) and 2 for (d), and the collection angles are shown in each graph.

The contrast from low-dimensional defects within a lattice can be greatly enhanced from channeling, in which an atomic column functions as a microlens to focus the broad probe electrons into a narrow peak. The above enhancement effect varies with the collect angle, occupied lattice site, as well as dopant species. As shown in figure 4-3,

[‡] The standard ABF imaging is equivalent to the TEM hollow cone illumination imaging technique, in which an annular detector only covers outer half of the illumination cone. However, the ABF imaging technique here involves both the signal channel within and outside (mainly) the illumination cone.

the visibility of the dopants oscillates with depth referring to the top surface within the lattice. Within a 10 nm thick specimen, Al ions become brighter if they sit within the first 5 nm depth, and then become darker when they are in a depth of 5-8 nm, and then become brighter again. In another words, the optimized condition of imaging Al is when Al ions sit at the depth of 4-5 nm in a 10 nm thick specimen. On the other hand, the visibility of Pr ions oscillates with depth but at higher frequency. For the HAADF images, the contrast enhancement effect from channeling mainly occurs in the first 1 nm depth, which is consistent with invisible contrast from Pr in $SrTiO_3$ lattice noted in the previous section.

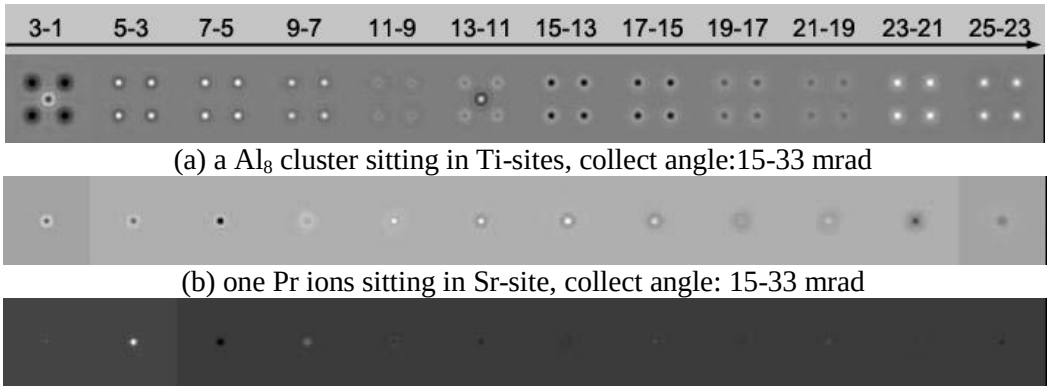

(a) a Al_8 cluster sitting in Ti-sites, collect angle:15-33 mrad

(b) one Pr ions sitting in Sr-site, collect angle: 15-33 mrad

(c) one Pr ions sitting in Sr-site, collect angle: 75-163 mrad

Figure 4-3 Contrast enhancement by channeling based on the multislice simulation. The simulation box has a dimension of 27x27x100 Å containing 6,370 atoms, in which one Sr-site is occupied by a Pr atom ((b) and (c)) or eight Ti-sites are replaced by eight Al ions (a). The enhancement of contrast is defined as the difference between two defect configurations, in which the defects sit at adjacent depth with respect to the top surface. The axis is labeled by the two configurations with the depth in the unit of unit cells. From left to right, the lattice sites occupied by dopants are moving from the top surface to the exit surface.

4.2 EEL SPECTRA

Under the electron beam, both low-dimensional defects and bulk information are integrated and recorded as plan-view EEL spectra. Although the defect signal extraction from a single plan-view acquisition may thus seem unconventional, a series of plan-view acquisitions, each containing different contributing weights of the defect signals taken

from different regions of increasing thicknesses, can in principle be used to retrieve the missing low-dimensional defect information. In order to separate blind defect signals from bulk signals, many algorithms, such as principle component analysis (PCA) and independent component analysis (ICA)[116], can be used. Nonetheless, the representative 'signal' outputs by these methods are the linear combinations of the real components, in our case, the blind defect and bulk signals. The direct separation of blind signals seems impractical because of the indeterminate equations, in which both the sources and their mixing weights are unknown. However, if the mixing weights of defect and bulk signals can be precisely estimated from quantitative local thickness measurements, the extraction of blind surface signals becomes potentially straightforward, more reliable and relatively simple. This idea was initially developed for extracting spectroscopic information from the reconstructed surface on a $SrTiO_3$ (100) single crystals. In section 5.3 and 6.3.2, the successful demonstrations of this method on a single monolayer of surfaces and nano-clusters within the bulk of $SrTiO_3$ are presented.

4.2.1 Experimental Design: A Thickness Series

Acquisition of EEL spectra in transmission mode from areas of different sample thickness, provides a series of measurement where the defect (e.g. surface) and bulk components can be varied in a controlled fashion. Spectra from regions labeled P1,P2,…,Pn in figure 4-4, thus provide a constant contribution of the surface signal at each thickness while the bulk components varies systematically.

The Ti $L_{2,3}$-edge and O K-edge core-loss EEL spectra of $SrTiO_3$ crystals were acquired and used to probe the surface electronic structure due to the following reasons. First of all, their major peaks are sensitive to local physical and chemical environments, including oxidation state and crystal field effects[107]. Secondly, EELS signal intensity is linearly related to the local thickness of the specimen under the single electron scattering condition in the samples studied in our work.

Mathematically, the whole idea is described by the following equation:

$$S_{Pi} = t_{B,Pi} S_B + t_{D,Pi} S_D \quad i = 1, 2, ..., n \qquad \text{Equation 4-1}$$

where, S_{Pi} is the experimental EEL spectrum at position Pi. At position Pi, S_B and S_D are the EEL spectra per thickness for the bulk and defect, respectively. $t_{B,Pi}$ and $t_{D,Pi}$ are the thickness for the bulk and defect, respectively.

Figure 4-4 Schematic diagram of a 'thickness' series

4.2.2 Step I: Background Subtraction

The core-loss EEL signals contain core shell level edges originating from the excitation of inner shell electrons and a relatively large background mainly arising from the excitation of loosely-bonded electrons within the specimen. Thus, accurate background subtraction from original datasets is essential for the quantification and structural analysis of EEL spectra. Traditionally, a background model is proposed and fit to the pre-edge with or without post-edge regions and then extrapolated to the edge region to isolate the spectrum edge itself. A simple and popular background model is an inverse power-law model which provides not only excellent agreement with experimental datasets but also based on a well-founded description of the related physical processes including the Drude model and the hydrogenic cross section[93].

The recorded counts C_i in an individual energy interval E_i are treated as the sum of the ionization edge S_i and the background B_i, thus,

$$\mathbf{C} = \mathbf{S} + \mathbf{B} \qquad \text{Equation 4-2}$$

The inverse power-law background model describe ***B*** as

$$\mathbf{B} = \alpha \mathbf{E}^{-r} \qquad \text{Equation 4-3}$$

In which, ***C***, ***S***, ***B*** and ***E*** are (nx1) vectors, and n is the total number of energy intervals involved.

Table 4-1 Various EELS background parameter estimators

	Least Square	Weighted least square		Maximum likelihood (Cramér-Rao lower bound)
Moments	$m_l = \sum x_i^l \Big/ n$	$m_{\sigma l} = \sum \sigma_i^{-2} x_i^l \Big/ \sum \sigma_i^{-2}$	≅	$m_{\lambda l} = \sum \bar{C}_i x_i^l \Big/ \sum \bar{C}_i$
$E\{\alpha - \bar{\alpha}\}$	B{y_i}	B{y_i}		0
$E\{r - \bar{r}\}$	0	0		0
Var(α)	$\frac{\sum (m_2 - m_1 x_i)^2 \operatorname{var}(y_i)}{\{\sum (x_j - m_1)^2\}^2}$	$\frac{m_{w2}}{\sum \sigma_i^{-2} (x_i - m_{w1})^2}$		$\frac{m_{\lambda 2}}{\sum \bar{C}_i (x_i - m_{\lambda 1})^2}$
Var(r)	$\frac{\operatorname{var}(y_i)}{\sum (x_j - m_1)^2}$	$\frac{\operatorname{var}(y_i)}{\sum \sigma_i^{-2} (x_j - m_{w1})^2}$		$\frac{1}{\sum \bar{C}_i (x_j - m_{\lambda 1})^2}$
Covar(α,r)				$\frac{m_{\lambda 1}}{\sum \bar{C}_i (x_j - m_{\lambda 1})^2}$
Var(a)	$a = \alpha - r \cdot m_1$ $\operatorname{var}(y_i) \Big/ n$	$a = \alpha - r \cdot m_{\sigma 1}$ $\operatorname{var}(y_i) \Big/ \sum \sigma_i^{-2}$	≅	$a = \alpha - r \cdot m_{\lambda 1}$
Covar(a,r)	0	0		0

Note: E(*) is the expectations of the observations, var(*) is the variance of *, describing the fluctuation about the observations or expectations.

Accordingly, how to extract the background becomes a statistical parameter estimation problem. Several mathematical methods were applied to evaluate the optimized parameters, and the results were summarized in Table 4-1 with the details stated in Appendix 1. Compared to the common-used logarithmic (weighted) least square methods, the maximum likelihood estimation method provides unbiased and minimum mean square error estimates of all parameters for the inverse power-law background model and was thus implemented in our work. A *MATLAB* code was developed and applied to the original EEL spectral image datasets to numerically solve the power-law background and provide the optimum signal-to-noise of the extracted ionization edge. (The code is attached as in Appendix 2.1)

Although the background removal is subjectively user-dependent and subjected to quite some debate, some general rules have to hold to achieve better quality results: (1)

the more counts the better, e.g. 10000 counts will give roughly 1% uncertainty in S_i; (2) background windows should be close to signal windows as much as possible; (3) a larger background fitting window, which will reduce the variance caused by background fitting. It should be noted that if necessary, the effect of multiple scattering has to be removed by de-convoluting with corresponding low-loss spectrum. However, such methods are based on Fourier techniques and can also introduce severe artifacts.

4.2.3 Step II: Spectra Alignment and Normalization

Reliable extraction of the surface signal from the EEL spectra demands accurate alignment of all recorded spectra along the energy-loss axis and normalization of the signal to account for the changing thickness and the variation in incident electron beam intensity over time. Under the reasonable assumption of dominating bulk signals, the EEL spectra are precisely aligned using the major features of the bulk EEL spectra. Additionally, EEL spectra are normalized to the continuum past the edge (about 15 eV above the threshold) which is insensitive to bonding variations but only proportional to the number of atoms excited by the electron beam and electron beam current.

4.2.4 Step III: Thickness Evaluation

To estimate the local thickness associated with individual EEL spectra, both low-loss EEL spectra and position averaged convergent-beam electron diffraction (PACBED)[117] images were recorded from the same region. Both techniques can be used to estimate the thickness of a sample. However, the low-loss EEL spectrum provides reliable local thickness estimation for thick regions (~> 40 nm), but is less accurate at the very thin regions due to the large contribution of surface signals and the potential presence of hydrocarbon contamination peak. Therefore, thickness quantification was carried out using the complementary method of PACBED images as this technique has been shown to be reliable particularly for very thin samples used for quantitative HAADF imaging. Precise evaluation of the local thickness was achieved by comparing significant

experimental features in the convergent beam diffraction patterns with simulated patterns (Figure 4-5) based on the well-established multi-slice theory[109]. Thus, the error of the local thickness estimation is estimated to be a few unit cells as discussed in reference[117].

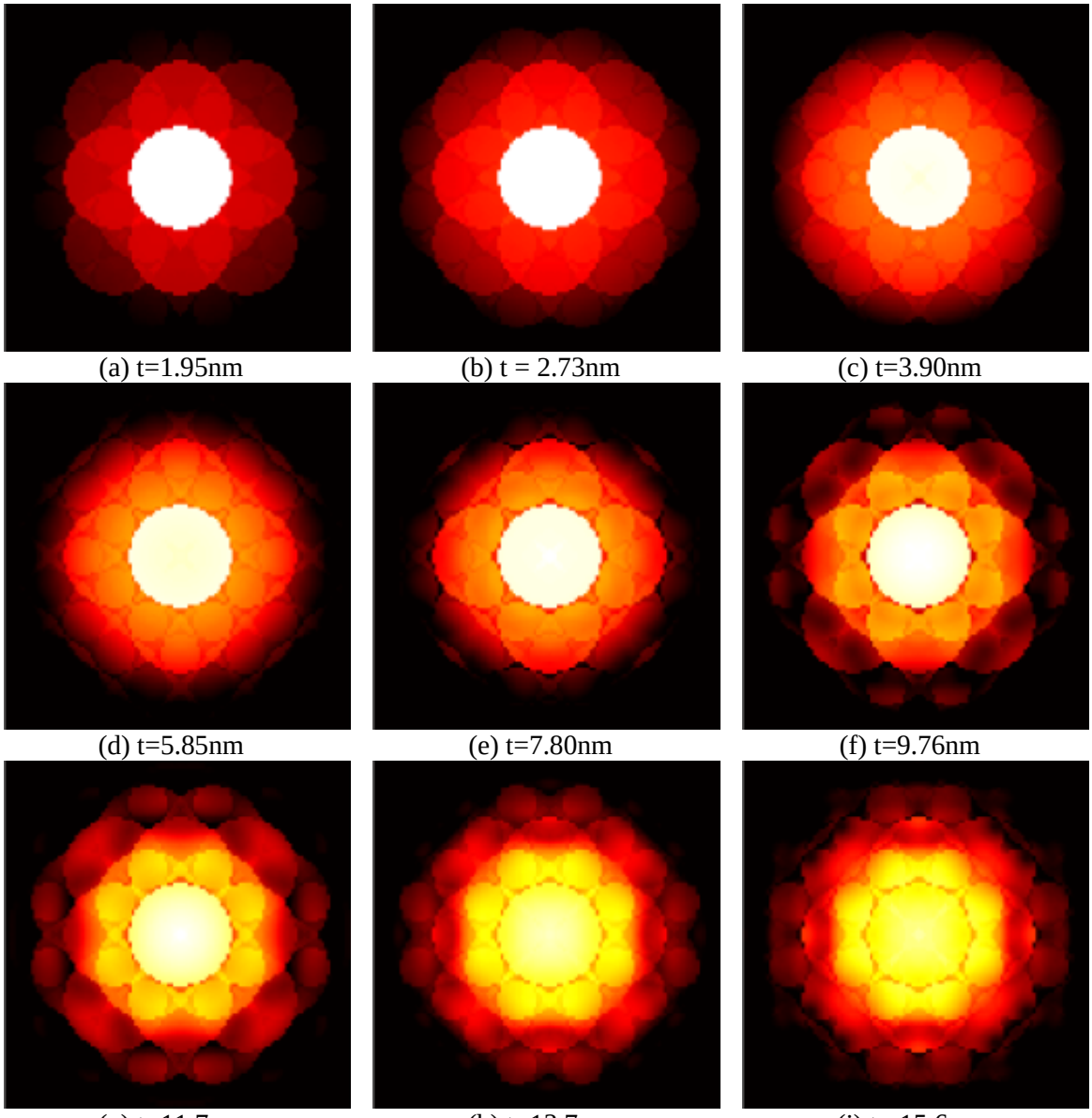

(a) t=1.95nm (b) t = 2.73nm (c) t=3.90nm

(d) t=5.85nm (e) t=7.80nm (f) t=9.76nm

(g) t=11.7nm (h) t=13.7nm (i) t= 15.6nm

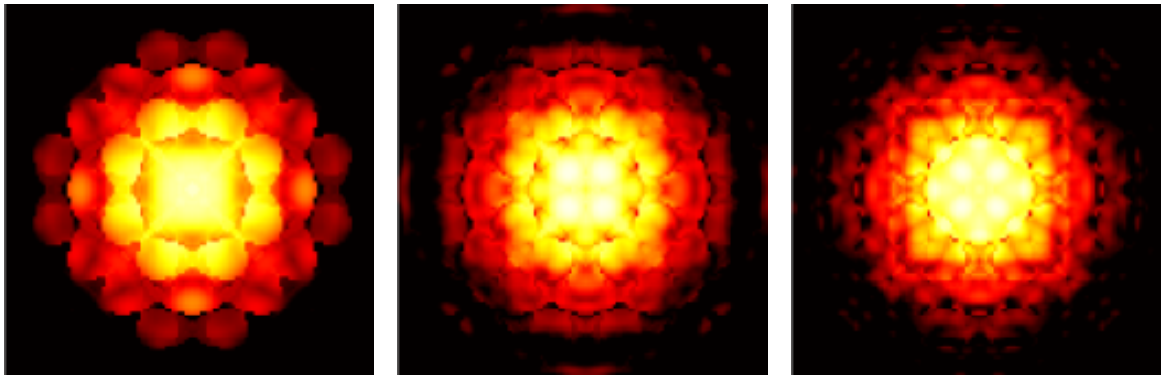

(j) t=19.5nm (k) t=31.2nm (l) t=39.5nm

Figure 4-5 The simulated PACBEDs with different specimen thickness for a (001)-oriented $SrTiO_3$ lattice. Thicknesses are labeled under each graph.

4.2.5 Step IV: Signal Extraction

After the spectra were acquired at regions with known thicknesses, a linear least square fitting method was used to extract the defect and bulk signals for individual energy intervals where the coefficients were deduced from the thickness measurements. It should be noted that a *MATLAB* function named 'lsqnonneg' was involved in extracting the surface and bulk signals (see Appendix 2).

CHAPTER FIVE

RESULTS: (001)-ORIENTED $SrTiO_3$ RECONSTRUCTED SURFACES

$SrTiO_3$ crystals attract continuing interest owing to the novel structure and properties exhibited at the crystal surfaces, which have led to their widespread application as standard substrates for the epitaxial growth of functional thin films and nano-structures and as the preferential photo-catalyst to split water for solar hydrogen generation. In spite of their technological and scientific importance, the understanding of their atomic and electronic structure is still incomplete due to the limitation of high-resolution (HR) characterization. In this chapter, we demonstrate the application of HR EELS and TEM, with plan-view and cross-sectional imaging modes, to extract both experimental structural and spectroscopic information on the valence state and local crystal field of Ti atoms on the surface of a $SrTiO_3$ crystal. The results fill the experimental gap of depth sensitivity and more importantly, show that valuable spectroscopic information can be deduced on surface atoms even in transmission electron microscopy.

5.1 FORMATION OF SURFACE RECONSTRUCTION

The air-stable surface patterns formed on TEM wedge specimens are strongly associated with the annealing treatment. In this section, only the specimens annealed at 900 ℃ and 975 ℃ in air are discussed.

5.1.1 (2x1) Surface Pattern

The TEM wedge specimen annealed at 975 ℃ has a (2x1) reconstructed surface structure. The extra reflections in the diffraction pattern (primitive cells are marked in figure 5-1) reveal the existence of single surface steps domains with 2x1 unit cells consistent with the literature[23]. As shown in the bright-field (BF) image, the edges prefer to exist along {100} sets of planes.

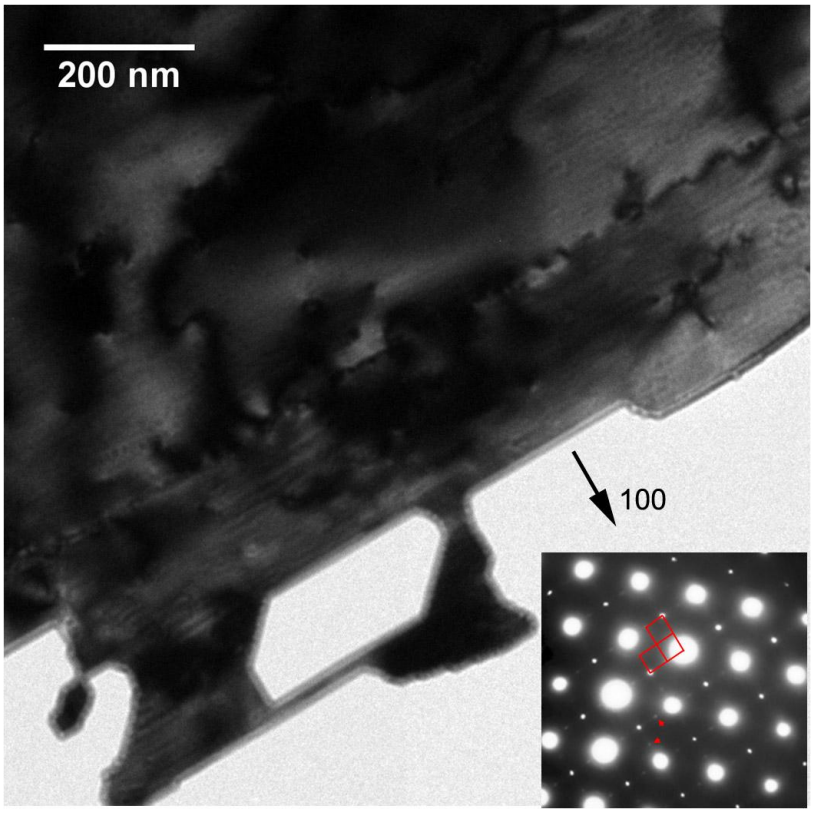

Figure 5-1 BF image of [001] zone axis and diffraction pattern (DP) as inserted with arrow indexed the extra group of points from the surface reconstruction structure.

5.1.2 c(4x2) Surface Pattern

A c(4x2) surface reconstruction was obtained in the heat-treated specimen at 900˚C. The extra diffraction points in the insert in figure 5-2 marked by yellow lines reveal the existence of the single surface domain with 4x2 unit cells. Similar to the (2x1) surface patterns, surface steps form along the <100> direction.

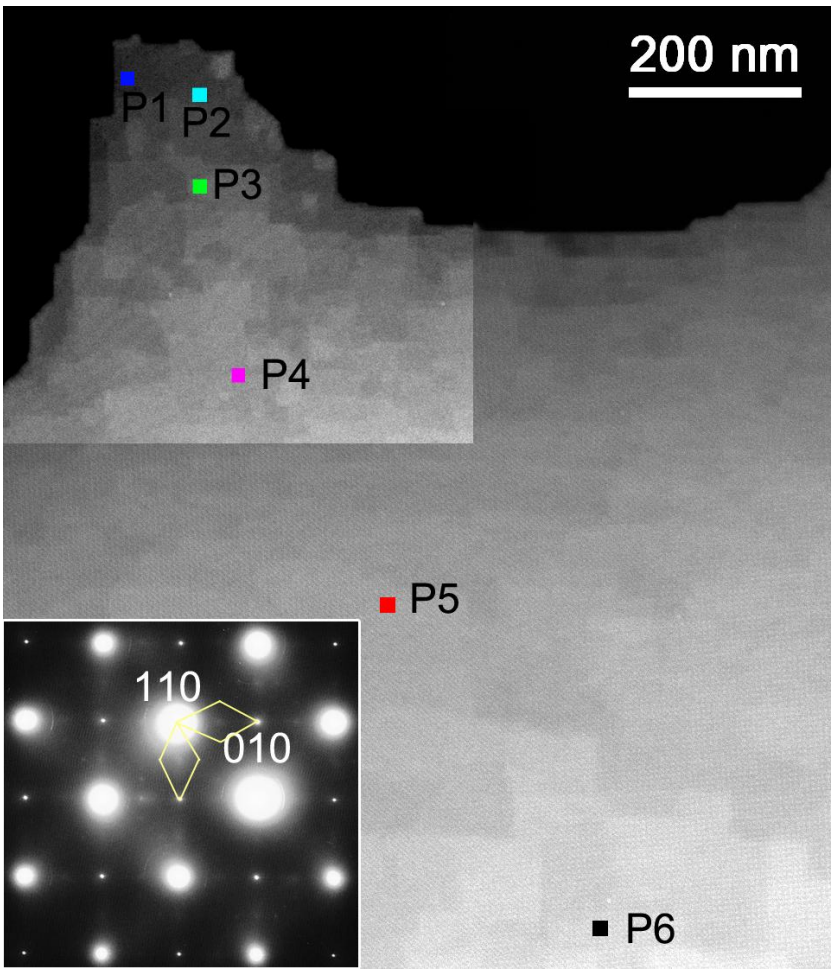

Figure 5-2 STEM-HAADF image of ~[001] oriented sample and related diffraction pattern (in the insert) of the c(4x2) surface reconstructed $SrTiO_3$. Yellow lines in the diffraction pattern highlight the extra reflections arising from the surface reconstruction. The pattern was intentionally overexposed to reveal the weak surface reconstruction reflections. The labels P1-P6 are used for further analysis in section 5.3.

From STEM-HAADF imaging (Z-contrast images), uniform contrast from individual approximately rectangular regions is visible. The lateral dimensions of the terraces vary from 30 to 100 nm in length along <100> directions and imply that the local thickness is constant within these regions. Samples prepared by the same approach have been shown to exhibit terraces of uniform thickness as demonstrated from secondary electron (SE) images[21].

5.2 HIGH-RESOLUTION PROFILE IMAGES

Since the profile images require the incoming electron beam to be perpendicular to the reconstructed surfaces, they provide a comprehensive depth field of view along the third dimension normal to the surfaces. As a consequence, they provide depth information which is missing from other techniques such as diffraction. In this section, we report the first experimental results on the third dimension of the reconstructed $SrTiO_3$ surfaces, which are consistent with energetically favorable structures computed by density functional theory (DFT) simulation.

5.2.1 (2x1) Surface Pattern

The local atomic arrangement of the reconstructed surface was investigated using atomic-resolution HAADF images at the edge of the thin foil under reasonable assumption that the pattern formed at the edge of the TEM foil should be exactly the same as the pattern on the surface (these would be exactly the same {001} crystallographic planes). The STEM-HAADF and simultaneously acquired BF or annular bright-field (ABF) images show that the Ti-O columns are unperturbed while the top-most layer shows a significant rearrangement (see figure 5-3). The spacing between the top-most and subsurface layer is slightly larger (2.1-2.3 Å), which agrees with references[23].

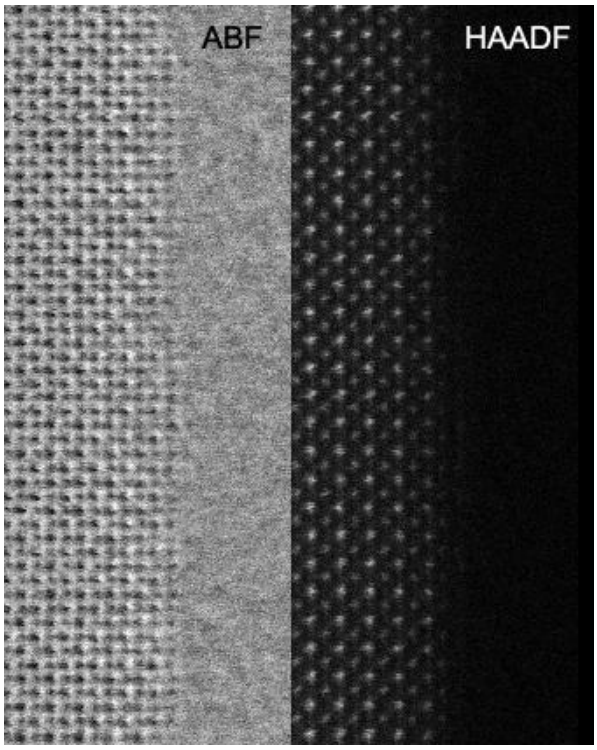

(a) The micrographs from left to right are the ABF and HAADF images

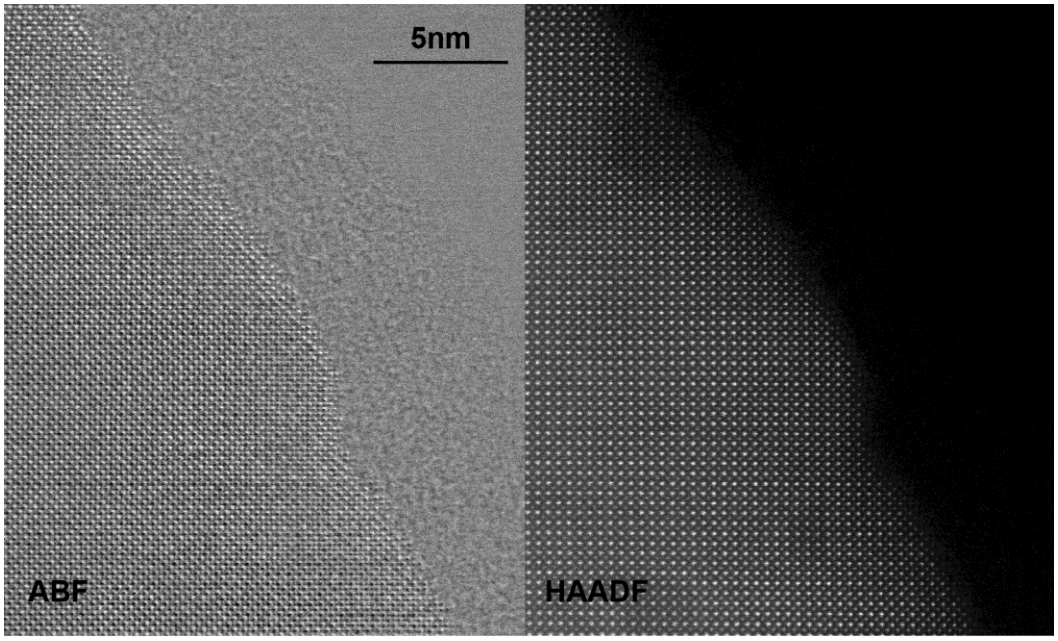

(b) The micrographs from left to right are the ADF and HAADF images

Figure 5-3 High-resolution profile images of the (2x1) surface reconstructions

5.2.2 c(4x2) Surface Patterns

Analogous to the profile images of the (2x1) surface pattern, the STEM-HAADF and simultaneously acquired BF images show that the Ti-O columns are unperturbed while the very top-most layer shows a significant rearrangement (see red arrows in figure 5-4 (a) & (b)). We observed that a few (edge) atoms have shifted from their regular lattice positions suggesting that some reconstruction, up to a few atoms high above the reconstructed (100) plane occurs. The displaced atoms are also visible as rows (individual atoms would not be visible). The experimental measurement of the spacing between the top-most and subsurface layer is roughly 2.4 ± 0.1 Å, significantly larger than the normal (100) plane spacing of 1.9 Å. The above measurements are in fairly good agreement with the proposed atomic model of Erdman et al. [25], this being reduced from the density functional theory (DFT) calculation. Based on the same atomic model[25], simulated HAADF image from both [010] and [001] view directions are entirely consistent with the present experimental profile image, as shown in figure 5-4 (c).

It should be noted that surface steps with heights corresponding to one unit cell are visible at the edge of the foil (Figure 5-4 (a) & (b)). Although the length of these steps appears to be inconsistent with the dimension of the terraces seen from the plan-view image, the length and step height of terraces vary as a result of different inclination angle with respect to the {100} planes, which is $1.4\,^{\circ}$ on the surface while it is $9\,^{\circ}$ at the edge.

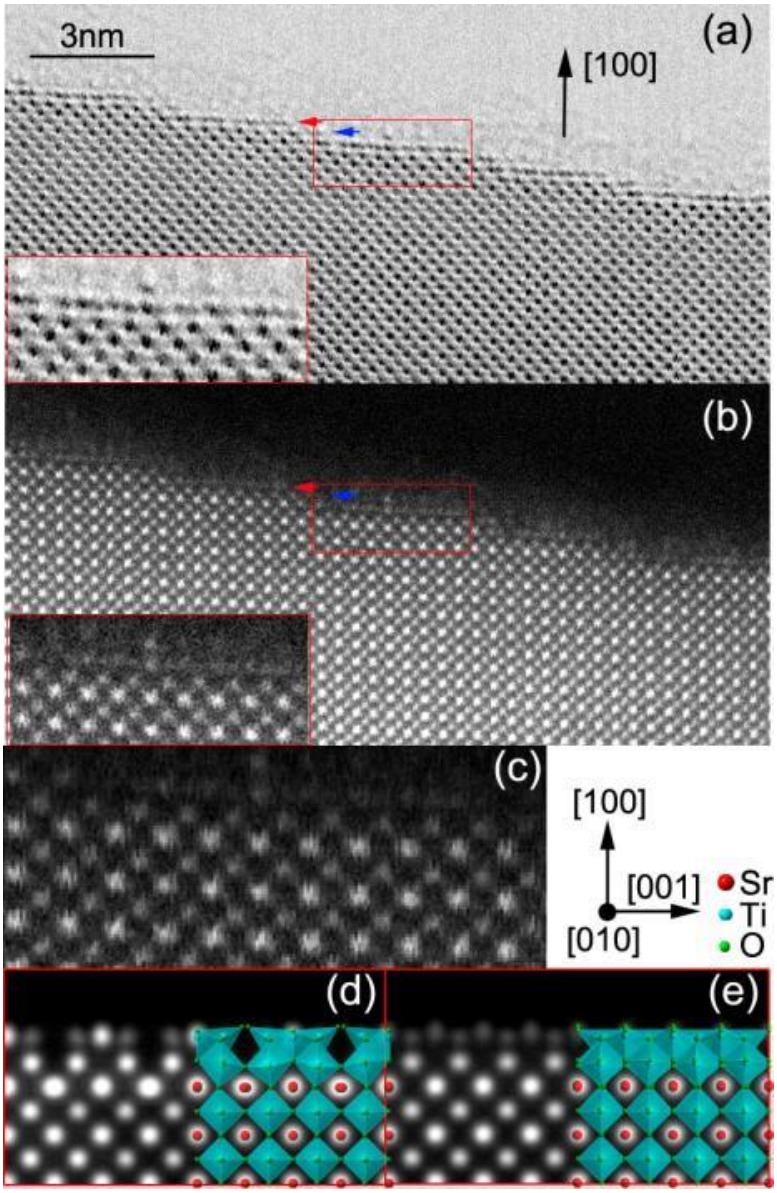

Figure 5-4 High-resolution BF (a) and HAADF (b) images of the typical edge of the surface-reconstructed sample. Red and blue arrows identify the top-most atomic layer and the sub-surface Ti-O atomic layer, respectively. The insert is a higher magnification view of the edge of the sample. Based on the detailed atomic model[25], (d) and (e) are simulated HAADF images using multislice method with view direction of [010] and [001], respectively. The simulation box contains 11,520 atoms within a supercell of 31 Å x 31 Å x 312Å. A fairly good agreement is achieved between the simulation and the experimental HAADF image (c) after applying singular value decomposition to highlight the surface features.

5.3 SURFACE SPECTRA

In this section, we will apply our new methods of a "thickness" series to investigate the surface electronic structure. The c(4x2) surface pattern is chosen as the model system.

5.3.1 Spectra from a Thickness Series

The acquisition of Ti $L_{2,3}$-edge and O K-edge EEL spectra in transmission mode from these terraces, over areas of different sample thickness, provide a series of measurement where the surface and bulk components can be varied in a controlled fashion. Spectra from regions labeled P1-P6 in the HAADF image (Figure 5-2), thus provide a constant contribution of the surface signal at each thickness while the bulk components varies systematically. As shown in figure 5-5(a), the Ti $L_{2,3}$-edge spectra shows a decrease in intensity with decreasing thickness, particularly of the e_g peaks. Based on the Pearson ratio[118], which quantitatively describes the intensity ratio between the white-line intensity (the sum of e_g and t_{2g} intensities) and the continuum past the edge as a monitor of 3d-orbital occupancy, this indicated that the average valence of the Ti gradually changes as the sample thickness decreases (and the surface component increases relative to the bulk). There is also a slight broadening of the spectral features as evidenced by the broader tails of the e_g and t_{2g} features. In detail, all peaks are broadened in proportion to their weighting of surface signals. Additionally, the position of the e_g peaks red-shifts with decreasing thickness, due probably to the surface re-organization of ionic positions. Being so close to the edge threshold, these changes in the edge shape cannot be attributed to multiple scattering effects.

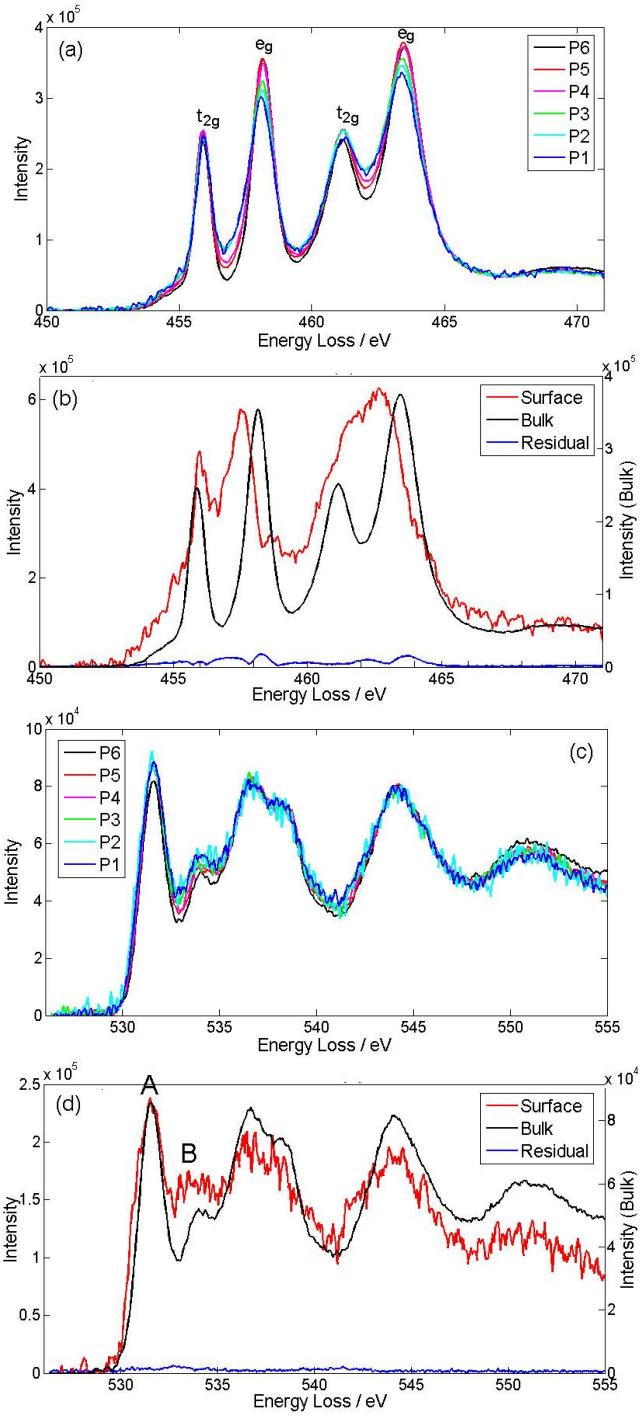

Figure 5-5 Experimental Ti $L_{2,3}$-edge (a) and O K-edge (c) EEL spectra at the positions P1-P6 marked in figure 5-2. (b) and (d) show the fitted surface and bulk EELS spectra from the linear least square methods with the coefficients deduced from the thickness measurement, respectively.

5.3.2 Thickness Measurement

Regarding the very thin regions of the specimen, position-averaged convergent beam electron diffraction (PACBED) images were applied to precisely measure the local thickness. As demonstrated in figure 5-6, a reasonable agreement between experimental and simulated PACBED one is achieved based on the similarities in the overlapping features of the diffracted disks.

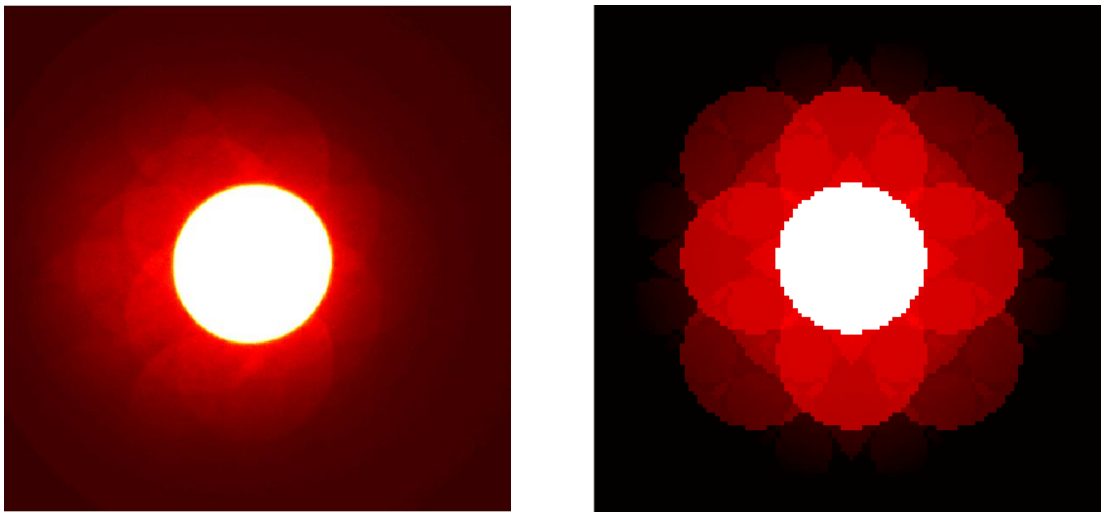

(a) Experimental (b) Simulated

Figure 5-6 Comparison between experimental and simulated PACBEDs. (a) is experimental data and (b) is from the multislice simulation (t=1.95nm, repeated from figure 4-5(a)). The simulation box has the dimension of 42.955x42.955 Å and the final dataset is the average of CBEDs taken from 1,024 frames within the super unit-cell.

The thickness evaluation for thick regions (~>40 nm) associated with individual EEL spectra was achieved through the low-loss EEL spectra based on the Fourier log-ratio method, which was provided as a routine in Digital Micrograph software.

5.3.3 Surface Spectra

The experimental Ti $L_{2,3}$-edge spectra were treated as the linear combinations of the surface and bulk signals as a result of an effective single electron scattering condition and the fact that the thickness of the thickest area (60 nm at point P6) is considerably

smaller than the total inelastic mean free path (>100 nm). A linear least square fitting method was used to extract the surface and bulk signals for individual energy intervals where the coefficients were deduced from the thickness measurements.

As shown in figure 5-5(b), the isolated bulk signal perfectly fits the standard Ti $L_{2,3}$-edge spectrum of $SrTiO_3$ while the isolated surface component has significantly broader features that resemble a spectroscopic signature of Ti^{3+} valence, confirming the first conclusions deduced from the inspection of white-line intensity normalized to the continuum past the threshold.

As an independent probe of the reduction of the surface titanium cations, the reduced number of oxygen anions at the surface can be estimated using the O K-edge EEL spectra and the same numerical decomposition based on precise thickness estimates. As expected, the isolated bulk component completely matches the standard $SrTiO_3$ O K-edge spectrum. The isolated surface signal is consistent with the bonding between titanium and strontium cations via oxygen anions. (Figure 5-5(d)) The titanium-oxygen bonding character, reflected by peak A corresponding to the unoccupied Ti 3d(t_{2g})–O 2p band and by peak B representing the unoccupied Ti 3d (e_g)–O 2p band, is broadened suggesting distorted octahedra and a stronger O-O interaction[119]. It should be noted that the shape of the surface spectra shows features consistent with the appearance of oxygen vacancies as demonstrated in the reference [99].

5.3.4 Multiplet Simulation

In order to support the valence state deducted for the surface Ti cations and provide insight on their coordination, we simulated the Ti $L_{2,3}$-edge spectra using a semi-empirical approach named charge-transfer multiplet approach (implemented in the CTM4XAS code). As a starting point, we have generated the spectrum for the excitation of Ti^{4+} in an ideal TiO_6 octahedron and obtained excellent agreement with the experimental bulk spectrum using a crystal field parameter of 10Dq=1.8 eV as well as known instrumental resolution and typical lifetime broadening.[120] In contrast to the bulk spectra, the crystal field parameters under different site symmetry, as well as charge

transfer effect, need to be taken into account for the atomic arrangement of the sub-surface and the top-most layer which shows experimentally an expansion of the interatomic spacing and a lower valence signature which is consistent with the reduced bond valence charge of surface titanium cations indicated from DFT simulation[25]. The blue and purple curves in Figure 5-7 show the predicted Ti^{4+} $L_{2,3}$-edge EEL spectra for titanium cations located in a distorted TiO_6 octahedron and in a pyramidal TiO_5 octahedron with modified charge-transfer, respectively. Under the simple but reasonable assumption of equivalent contributions of both TiO_6 and TiO_5 polyhedra, the simulated surface spectrum is in accordance with the experimental one (red curve in Figure 5-7) suggesting a spectroscopic signature of reduced Ti cations.

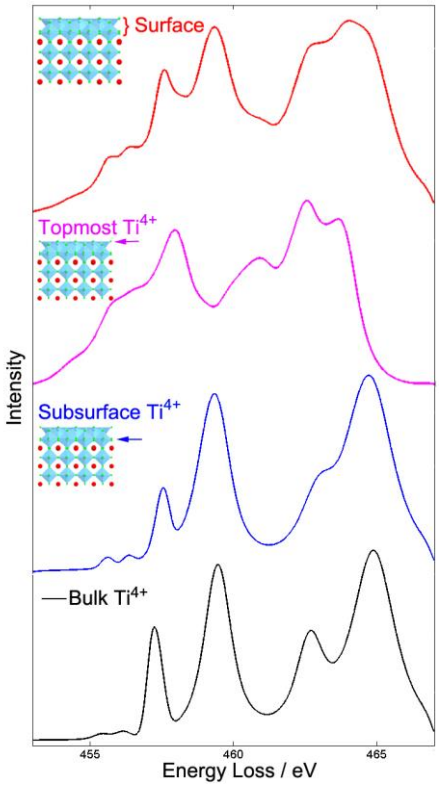

Figure 5-7 Atomic multiplet structure simulations of Ti $L_{2,3}$-edge EEL spectra with different crystal field effects. The black line stands for a Ti^{4+} cation sitting at ideal octahedral symmetry. The blue curve is associated with the sub-surface layer, in which the bonding between Ti^{4+} cation and oxygen onions sitting at the topmost layers with an elongated bond as inferred from the HAADF images. The purple curve is responsible to the topmost layer of pyramidal TiO_5 octahedron with charge-transfer effect. The surface

spectrum (in red) is simplified as the linear combination of topmost Ti^{4+} (in purple) and subsurface Ti^{4+} (in blue) with equivalent contributions.

In comparison with the previous atomic multiplet methods, in which the freely controllable crystal field parameters are input, the crystal-field multiplet method[112] was also applied. It directly constructs the crystal field by the positions and charges of the surrounding ions. Individual $L_{2,3}$ spectra of the five inequivalent Ti ions present in the topmost and subsurface layers have been calculated and summed according to their actual stochiometric ratio. A good convergence of the crystal field and simulated spectra has been achieved with clusters of about 500 ions generated from the structural model[22] used in figure 5-4. Whereas intra-atomic Coulomb and spin-orbit coupling parameters have been kept constant and equal to the $SrTiO_3$ bulk values[112], the only adjustable parameter employed to reproduce the experimental result consisted in the scaling of the crystal field strength (S_{xtal}). Best agreement was obtained for S_{xtal}=1.7 for the topmost layer. To account for the core-level shift due to changes in coordination[121], the topmost surface spectra were shifted down in energy (around 0.65 eV) with respect to the subsurface spectra. These values are consistent with typical range of values (1.0 to 2.0) used to match spectra used in the original paper[112] for different oxides. As shown in figure 5-8(a), Ti L-edge EEL spectra keep their bulk spectroscopic signature even from the layer closest to the reconstructed surface, which confirms the origin of the experimental surface EELS. In addition, the surface features are reproducible from the topmost and subsurface TiO layers. (see figure 5-8(b)) This suggests that the experimental surface signature can be interpreted as that of Ti^{4+} in both 5-fold and 6-fold coordination polyhedral when accounting for local distortions and changes in both ionicities and not to a simple reduction of this cation.

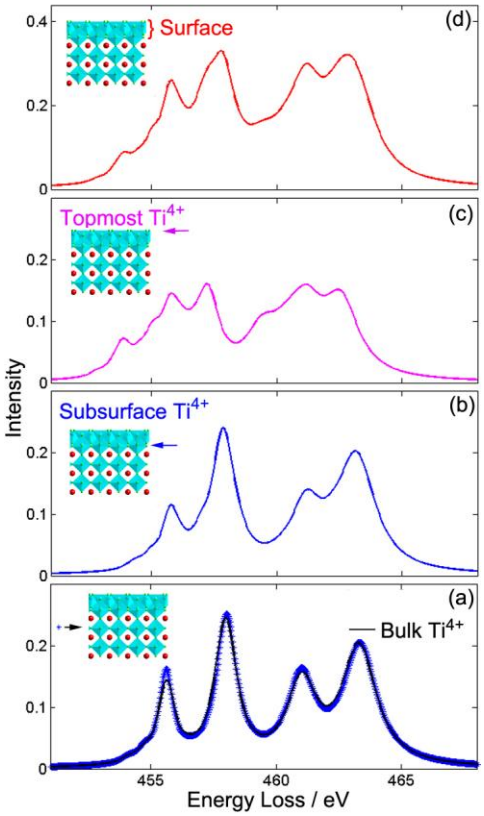

Figure 5-8 Crystal-field multiplet simulations of Ti $L_{2,3}$-edge EEL spectra with different crystal field effects. (a) EEL spectra for ideal bulk and the closest monolayer to the reconstructed surfaces. (b), (c) and (d) are the EEL spectra for the subsurface layer, topmost layer, surfaces containing all non-equivalent Ti surface ions.

CHAPTER SIX

RESULTS: LOW-DIMENSIONAL DEFECTS WITHIN ION-IMPLANTED $SrTiO_3$

Although $SrTiO_3$: (Pr, Al) powders are commercially available phosphors for field-emission displays and vacuum fluorescent displays, the understanding of their luminescence mechanism is still incomplete due to limited experimental evidence on the local defect configurations of Pr and Al dopants. To facilitate our characterization in a TEM, Pr^+ and Al^+ ions were implanted into $SrTiO_3$ single crystals and a post-annealing treatment was subsequently performed. Pr dopants were only detected at Sr-sites by 2-dimensional EELS mapping. The PL spectra suggest that the mechanism of luminescence enhancement from Al ions is different in our synthesis approach compared to the literature. Cube-shaped nano-clusters of about 0.8-2.4nm in size were observed appearing with a reduced intensity with respect to the STO background in HAADF images and with an enhanced intensity in ABF images. Image simulation and EDX mapping confirm that Al ions are concentrated within these nano-clusters. The function of the nano-clusters during luminescence was investigated by the EELS technique.

6.1 PHOTOLUMINESCENCE

A major emission peak of ~610 nm wavelength (red) was recorded in all specimens with different Pr /Al concentration under various annealing conditions. Another emission peak of ~490 nm wavelength (blue) was barely visible in the as-implanted and annealed specimens at 400 ℃ and was greatly enhanced with annealing temperature. Besides these two major peaks, several sharp and isolated peaks were detected. No detectable difference of these peaks was recorded in the specimens with various annealing treatment.

6.1.1 The Effect of Aluminum

In the (Pr, Al) co-implanted specimens, the intensity of this red emission peak increases with: (a) the reduction of Al concentration in the as-implanted specimens (Figure 6-1(a)); (b) the increase of annealing temperature (Figure 6-1(b)); and (c) slightly increases with increasing the annealing time at 700 ℃ (Figure 6-1(b)). In (Pr, Al) co-implanted specimens annealed at 800 ℃, the Al concentration ranging from 2 at.% to 15 at.% plays a weak role for the enhancement of the emission intensity, as shown in figure 6-1(c).

In the Pr-implanted specimens, the intensity of this red emission peak fluctuates with Pr concentration (Figure 6-1(d)). More importantly, its intensity is 3-4 times larger compared to (Pr, Al) co-implanted specimens. This measurement contradicts with the results in the literature (see figure 2-1) probably due to different synthesis methods. In the literature[44], solid state reactions of the raw materials at high temperature instead of ion implantation were used to prepare crystalline $SrTiO_3$ (Pr, Al) powders. Of particular importance, the position of this emission peak shifts toward the long wavelength direction after high-temperature annealing (e.g. $\geq$ 700 ℃) in the specimens without Al compared to the ones co-doped with Al (Figure 6-1(e)).

The change of the blue emission peak (~490 nm wavelength) basically follows the trends of the red emission peak except this peak increases its intensity with increase of Pr concentration in Pr-implanted specimens (Figure 6-1(d)).

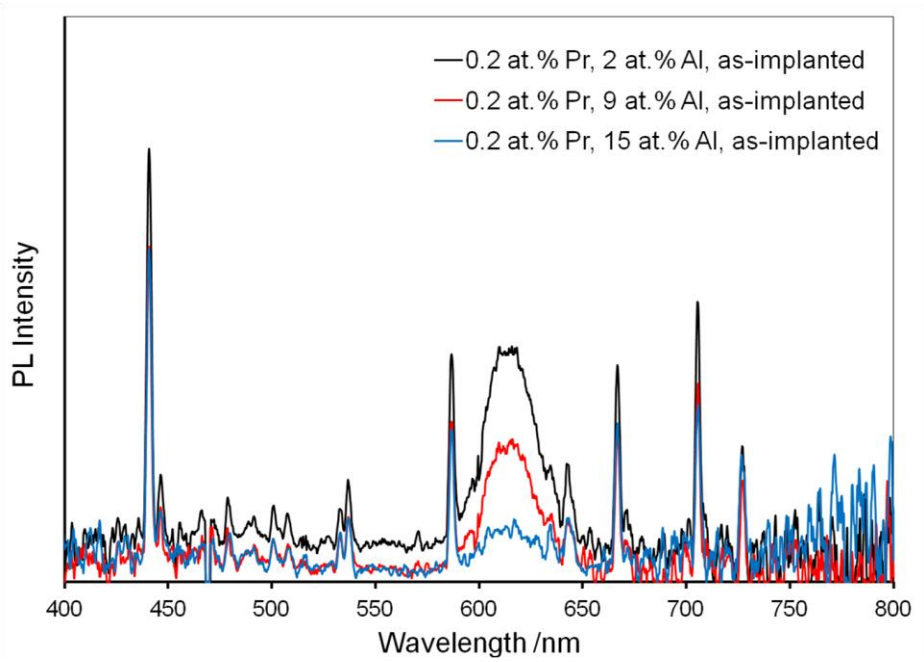

(a) As-implanted specimens with 0.2 at% Pr and different Al concentration

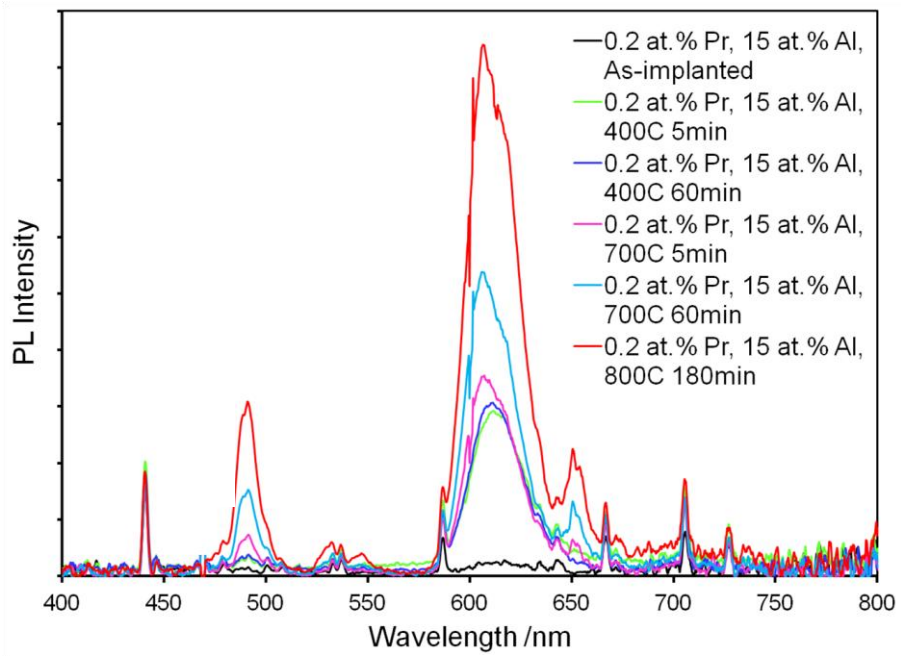

(b) Specimens with 0.2 at.% Pr, 15 at.% Al under various annealing conditions

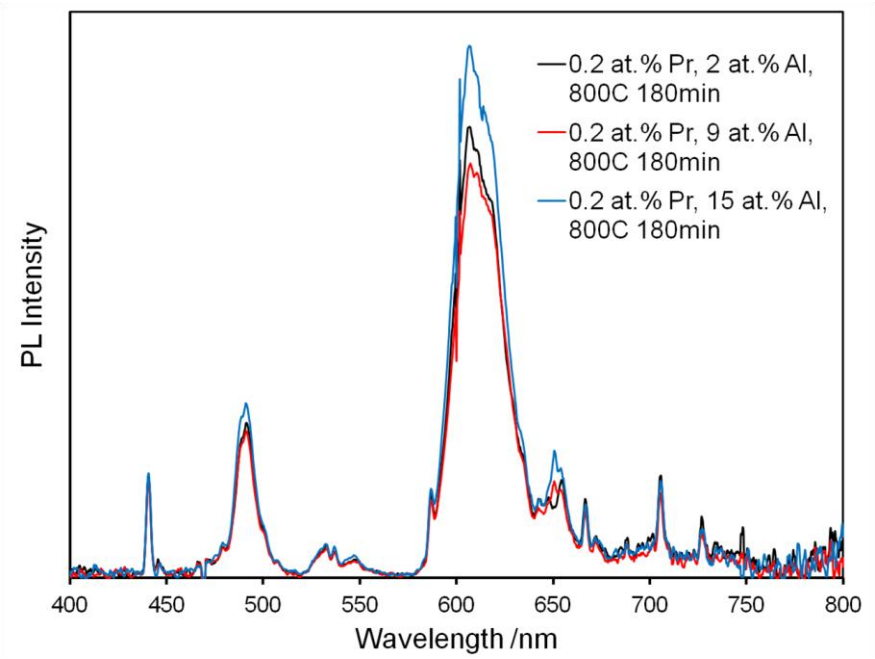

(c) Annealed specimens with 0.2 at.% Pr and different Al concentration

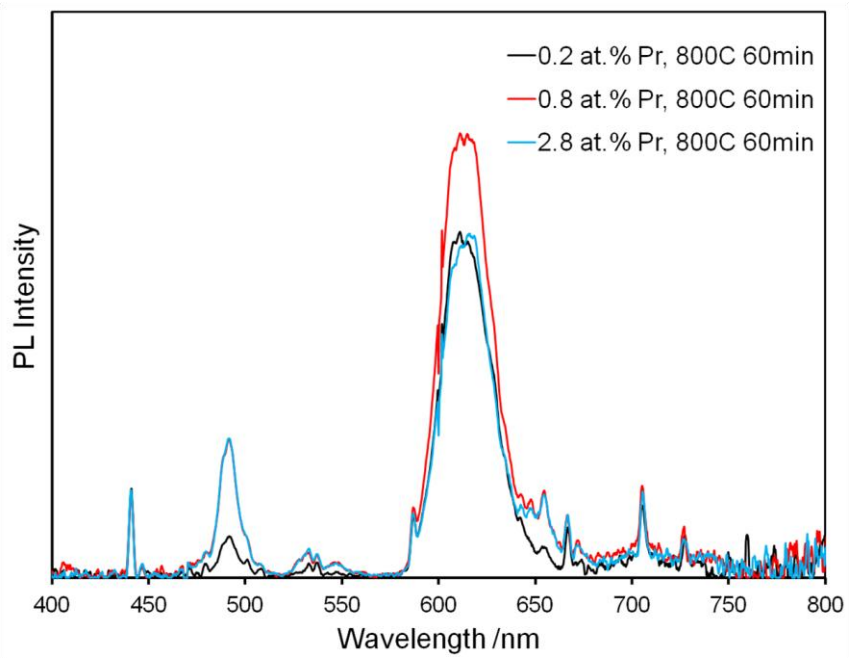

(d) Annealed specimens with different Pr concentration

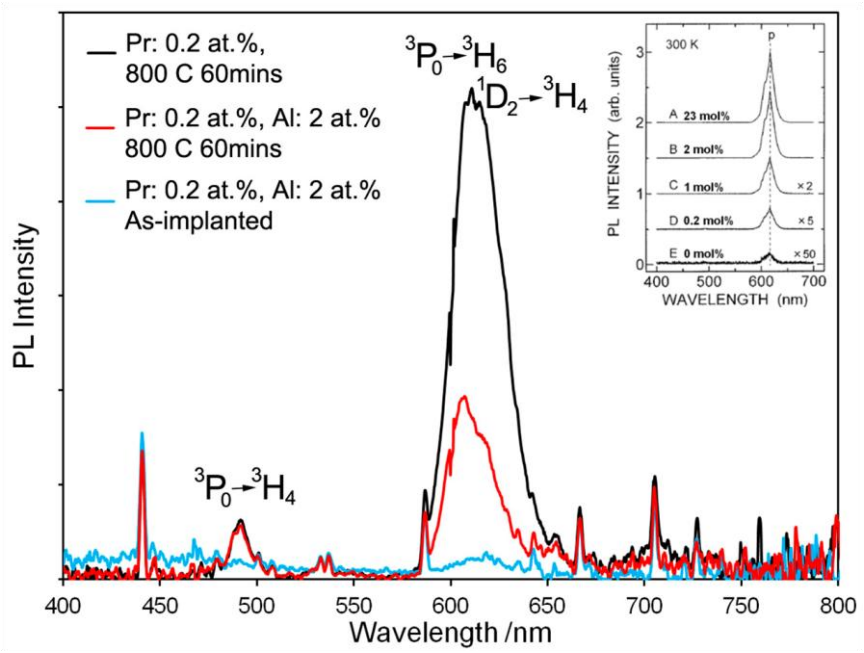

(e) Specimens with 0.2 at.% Pr and with or without 2 at.% Al. Some of the corresponding intra-4f transitions are labeled. As a comparison, figure 2-1(a)[44] is repeated here as the insert.

Figure 6-1 PL spectra at room temperature. The specimens are labeled with the peak concentration of selected injected ions and the subsequently treatment. Heat treatment is labeled as a combination of the temperature and time.

6.1.2 The Associated Crystal Field around Pr^{3+}

As mentioned in section 2.3.1, intra-4f transitions of rare earth (RE) elements are parity forbidden by the Laporte rule. All PL peaks are considered to raise from intra-4f transitions of Pr^{3+} ions, which indicates that Pr^{3+} ions, at least a few of them, are not situated at the centrosymmetric lattice sites; or there is symmetry breaking of the occupied lattice sites by additional Al ions or other point defects created during the implantation processes. In addition, these non-centrosymmetric sites, occupied by the injected atoms, are not, at least not fully, removed by annealing.

It should be noted that pure intra-4f transitions of RE elements are insensitive to their local crystal fields. However, the two major emission peaks are broad and increase in intensity following subsequent heat-treatment, indicating that they are strongly affected

by the local crystal field around the activated Pr^{3+} ions possibly due to the involvement of bonding electrons during the corresponding intra-4f transitions as suggested in the reference[44].

The blue-shift of the red emission peaks occurring in the (Pr, Al) co-implanted specimens after high temperature annealing (e.g. > 700 ℃) can be explained through the incomplete quenching of the $^3P_0$ state of Pr^{3+} ions via low-lying defect states as a possible consequence of neighboring Al^{3+} ions. The effect from crystallization is excluded because a blue-shift of the red emission peak was not detected in annealed Pr-only specimens. (see figure 6-1(d)) In the literature, Al^{3+} ions preferentially locate around Pr^{3+} ions, in order to compensate the charge difference between the Pr^{3+} ions and the host ions because of their charge and ionic radius. According to ref.[51], the energy position of inter-valence charge transfer (IVCT) bands, depends on the nature of the host lattice and is roughly inversely proportional to the optical electronegativity $\chi(M^{n+})$ of the transition metal cations. Compared to the bulk Ti cations ($\chi(Ti^{4+})$=2.05 [122]), the substitutional Al cations ($\chi(Al^{3+})$=1.6 [123]) shift the IVCT bands to higher energy position and thus impede the non-radiative relaxation path from $^3P_0$ to $^1D_2$ via IVCT bands. As a result, more 605nm photons are released from $^1P_0$-$^3H_6$ transition due to the reduced quenching from the $^1P_0$ state. $^1D_2$ state obtains less population and fewer 615nm photons are released from $^1D_2$-$^3H_4$ transitions. Thus, the position of the red emission peak shifts toward the short-wavelength direction.

The emission intensity is determined by a series of processes including the absorption of laser photons, the energy transfer to activated ions (Pr^{3+} ions), the emission from activated ions and the re-absorption of the emitted photons. In the present case, the absorption of laser photons is assumed to be the same due to the fact that absorption occurs in the same $SrTiO_3$ matrix. The re-absorption of the emitted photons is different between as-implanted and annealed specimens because of defect levels present within the band-gap (~3.4 eV for a perfect lattice) in amorphized $SrTiO_3$ layers.

In the (Pr, Al) co-implanted specimens, the emission from the activated ions is considered to be the same due to the same concentration of Pr ions. In the as-implanted

specimens, the intensity difference is most likely due to the re-absorption of the emitted photons by defects created during implantation. The more ions are injected in, the more defects are created. This is in accordance with the TEM results from as-implanted specimens: the damage layer is not fully amorphized in the specimen with the lowest Al concentration, while it is fully amorphized in the specimens with highest Al concentration (Section 6.2).

The enhancement of intensity after heat-treatment implies the recovery of the damaged lattice. This is consistent with the TEM characterization (Figure 6-2): the re-crystallized depth increases with annealing temperature. However, defects may not be fully recovered after annealing, which may explain why the intensity fluctuates with Al concentration in (Pr, Al) co-implanted specimens.

As we mentioned in section 2.3.1.2, high Pr concentration results in strong ion-ion interaction, which quenches the luminescence. Thus, in Pr-implanted specimens, a competitive process occurs between increasing luminescence centers and increasing cross-relaxation effect as well as implanted damage.

6.2 RECRYSTALLIZATION

In the present thesis, the damage layers in the as-implanted crystal wafers are the regions containing the injected ions, which are up to 40 nm deep as suggested from the SRIM simulation in section 3.2.1. From the structural point of view, the damage layers are defined as the regions with destroyed lattice structure. The damage present within the damage layers may be different at different depth. The bulk refers to the region without the effect of the injected ions, in which the perfect $SrTiO_3$ lattice can be clearly identified in the high-resolution images. The implantation direction in the present thesis is from left to right in all images. In the as-implanted crystals with 0.2 at.% Pr (and 2 at.% Al), we observed a 30-40 nm thick damage layer with heavy damage occurring in the range of 15-30 nm depth from the surfaces (Figure 6-3(c), Figure 6-4(a) & Table 6-1(b) and (c)). As shown in the HAADF images, the damage layers contain bright crystalline nano-domains

distributed in the dark background. In all other as-implanted crystals, a ~25-30 nm thick amorphous or near amorphous layer (e.g. the region with comparable dark contrast in the HAADF images) and 7-15 nm thick mosaic layer with slightly mis-oriented crystalline domains are recorded (Figure 6-2(a), Figure 6-3(a), Figure 6-4(c) and (e) & Table 6-1(a), (b) and (c)). We referred both the amorphous and mosaic layers together as the damage layer in these crystals. The extent of the damage, but not the depth of these damage layers, is affected by the dose of injected ions.

6.2.1 Thermal-Induced Recrystallization

Following subsequent annealing, the mosaic layer recrystallizes at 400 ℃ with this effect being more pronounced at higher annealing temperatures. In the crystal annealed at 700 ℃, the damaged layer recrystallizes except a roughly 7 nm thick amorphous layer (Figure 6-2(d) and (e)). The annealing time seems to play a negligible role on the recrystallization. These results imply that energy barriers for recrystallization are different at different depth. In the crystal annealed at 800 ℃, the amorphous layer is fully recrystallized with no detectable change of the periodic structure except at the implantation front (30-40 nm depth from the surfaces), where dislocations are present, consistent with implantation-damage theories[68]. The term "recrystallized layer", standing for the fully recrystallized ion-damaged layer in the annealed specimens is used in the following discussion.

In addition, cube-shaped nano-clusters of 0.8-2.4 nm in size were observed in the implanted regions (see the white arrows in figure 6-2(f) and figure 6-3(b) and (c)) appearing with a reduced intensity with respect to the $SrTiO_3$ background. Very few cube-shaped nano-clusters appear with relative larger size in the Pr-implanted $SrTiO_3$ single crystals (Figure 6-4(b), (d) and (f)).

In these HAADF (Z-contrast) images, Pr-clusters should be visible as bright islands because the atomic number of Pr is higher than all the other elements in the lattice. It should be noted that the contrast contributed by a single Pr atom is not detectable while a Pr-cluster is visible in the present experimental conditions (See appendix 3). Therefore,

we detected no clusters with higher intensity than the background in HAADF images of (Pr, Al) co-implanted specimens with 0.2 at.% Pr peak concentration suggesting that the Pr ions are uniformly distributed rather than coalesced into clusters.

In general, the damaged layer recovers and recrystallizes after annealing, which minimizes the negative effect of defects on photoluminescence. This is consistent with enhanced PL intensity after heat-treatment, as discussed in section 6.1.

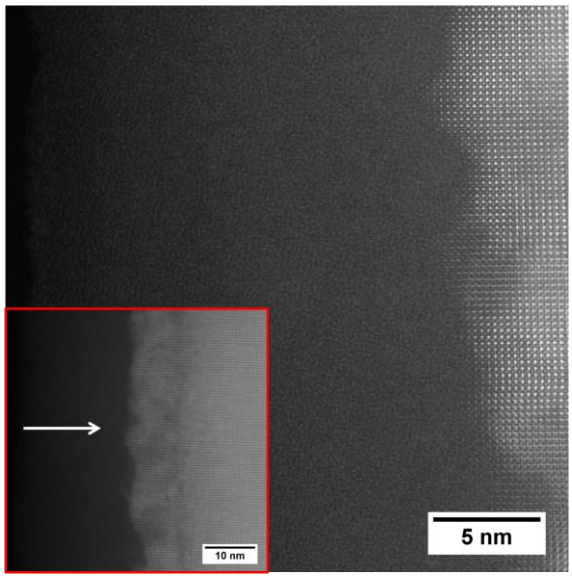

(a) As-implanted

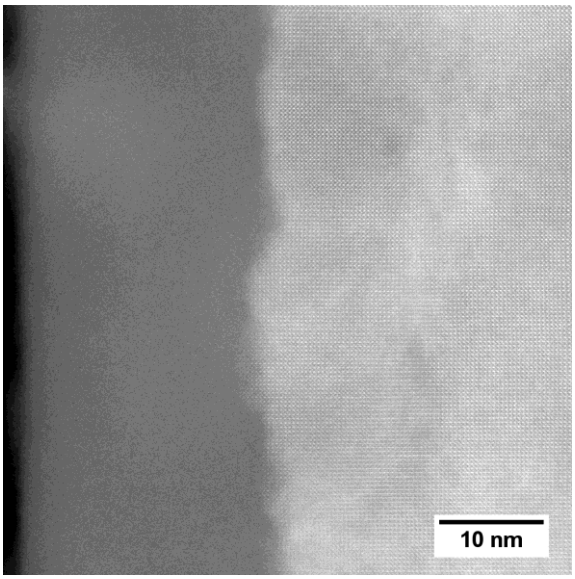

(b) 400 ℃ 5 min

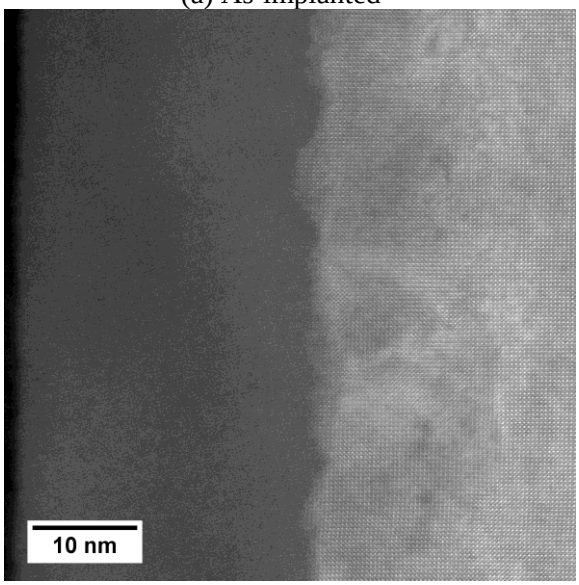

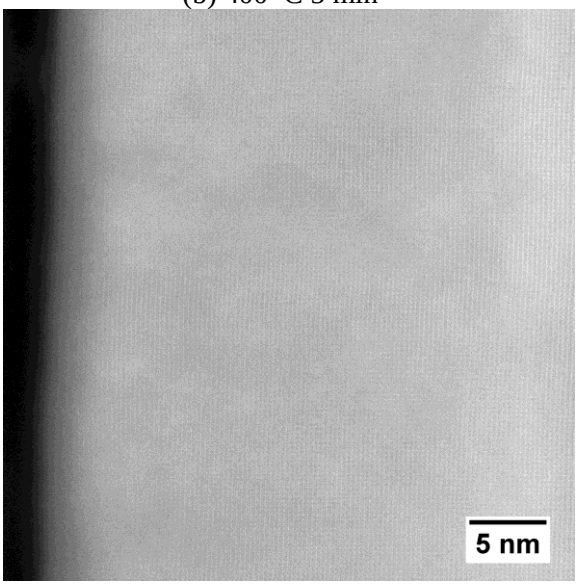

(c) 400 ℃ 60 min

(d) 700 ℃ 5 min

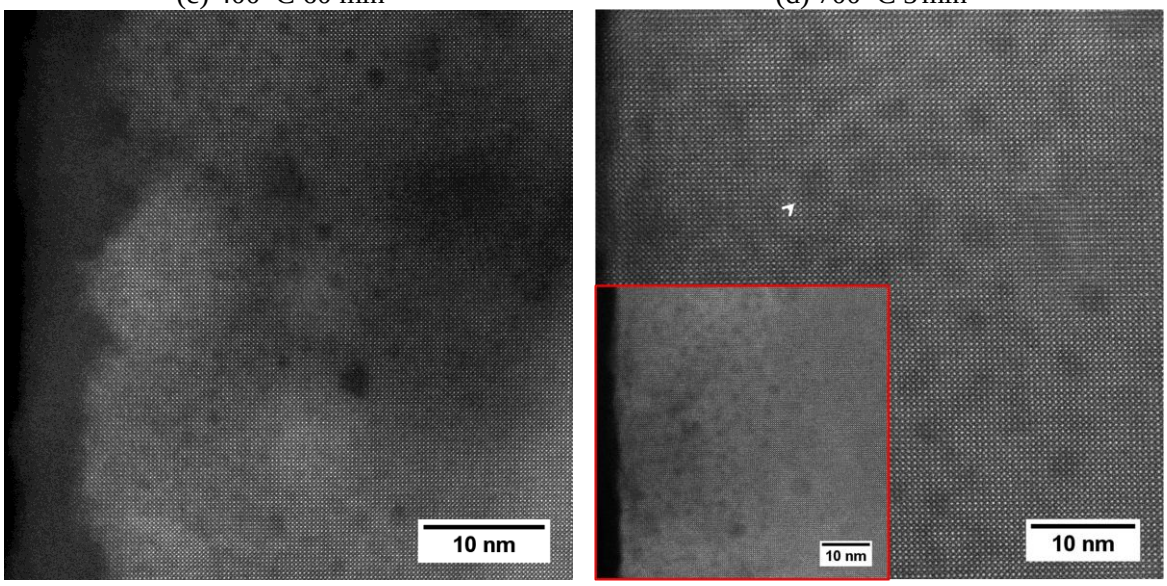

(e) 700 ℃ 60 min

(f) 800 ℃ 180 min

Figure 6-2 STEM-HAADF images of as-implanted (a) and annealed (400 ℃ for 5 min, (b); 400 ℃ for 60 min, (c); 700 ℃ for 5 min, (d); 700 ℃ for 60 min, (e); 800 ℃ for 180 min, (f) $SrTiO_3$ single crystals with 0.2 at.% Pr and 15 at.% Al co-implantation. The inserts are low magnification images showing the field of view and location of the damaged layer. The ions were injected from the surface (the left) into the bulk (the right), as shown in the white arrow in (a).

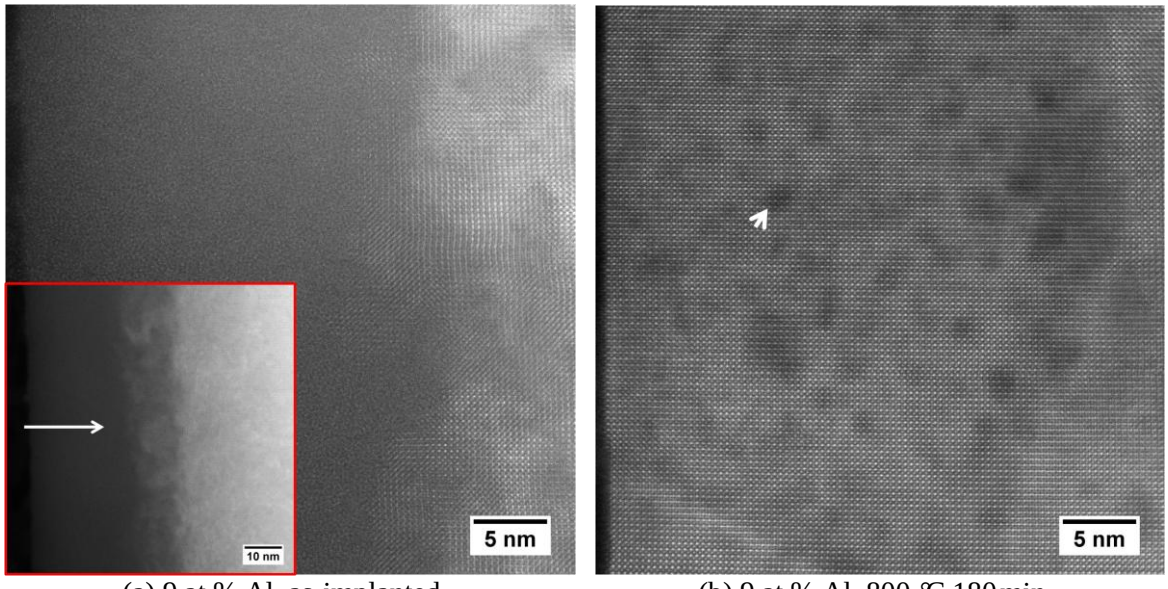

(a) 9 at.% Al, as-implanted

(b) 9 at.% Al, 800 ℃ 180 min

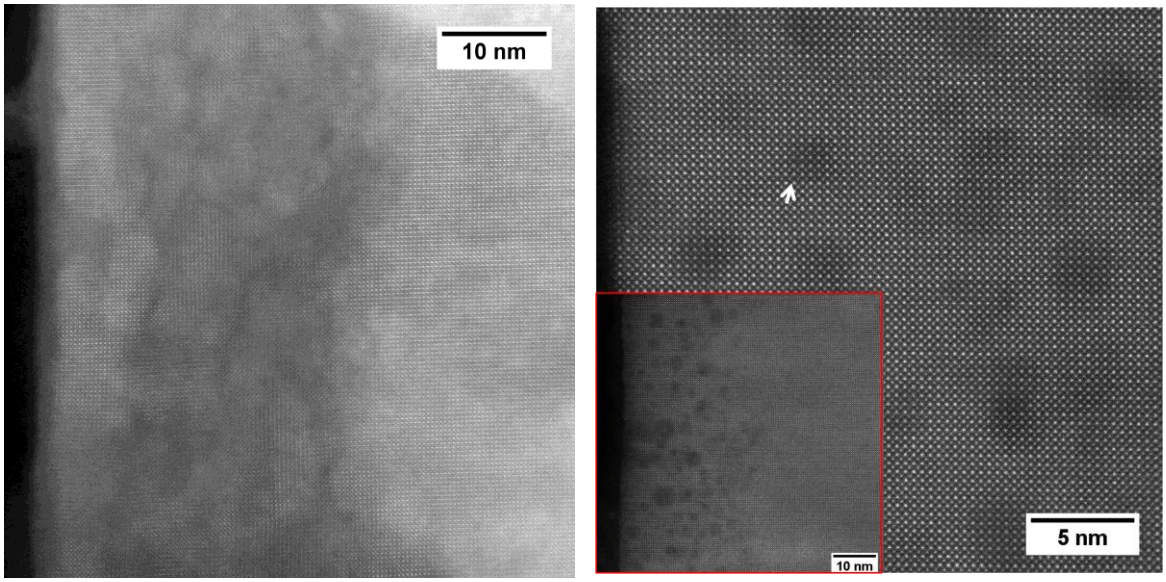

(c) 2 at.% Al, as-implanted (d) 2 at.% Al, 800 ℃ 180 min

Figure 6-3 STEM-HAADF images of as-implanted (a, c) and annealed (800 ℃ for 180 min, and (b, d) $SrTiO_3$ single crystals with 0.2 at.% Pr and 9 or 2 at.% Al co-implantation. The inserts are low magnification images showing the field of view and location of the damaged layer. The ions were injected from the surface (the left) into the bulk (the right), shown as the white arrow in (a).

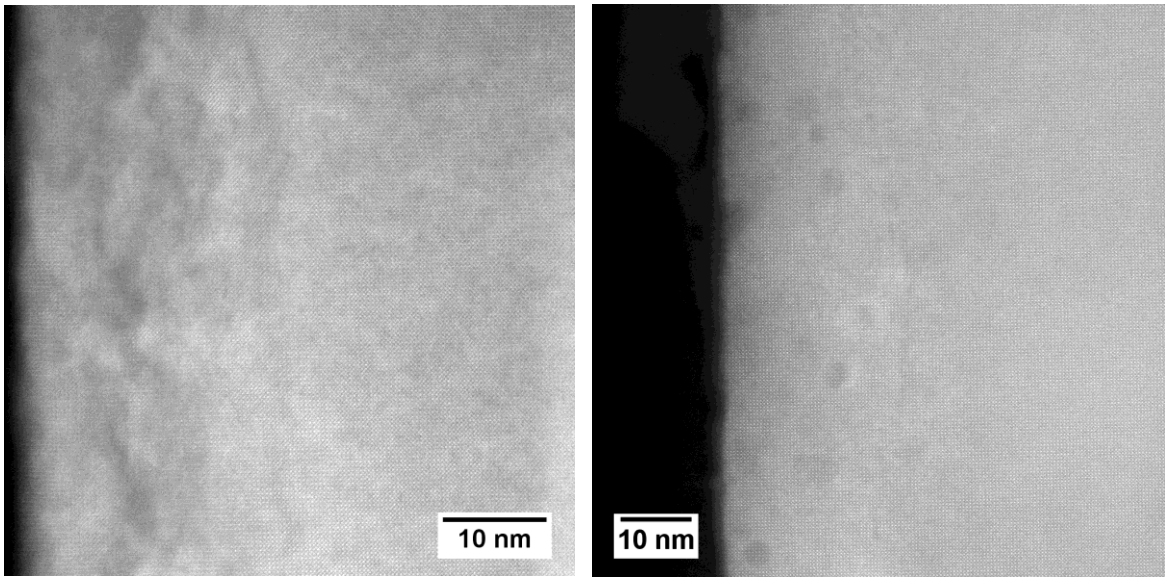

(a) 0.2 at.% Pr, as-implanted (b) 0.2 at.% Pr, 800 ℃ 60 min

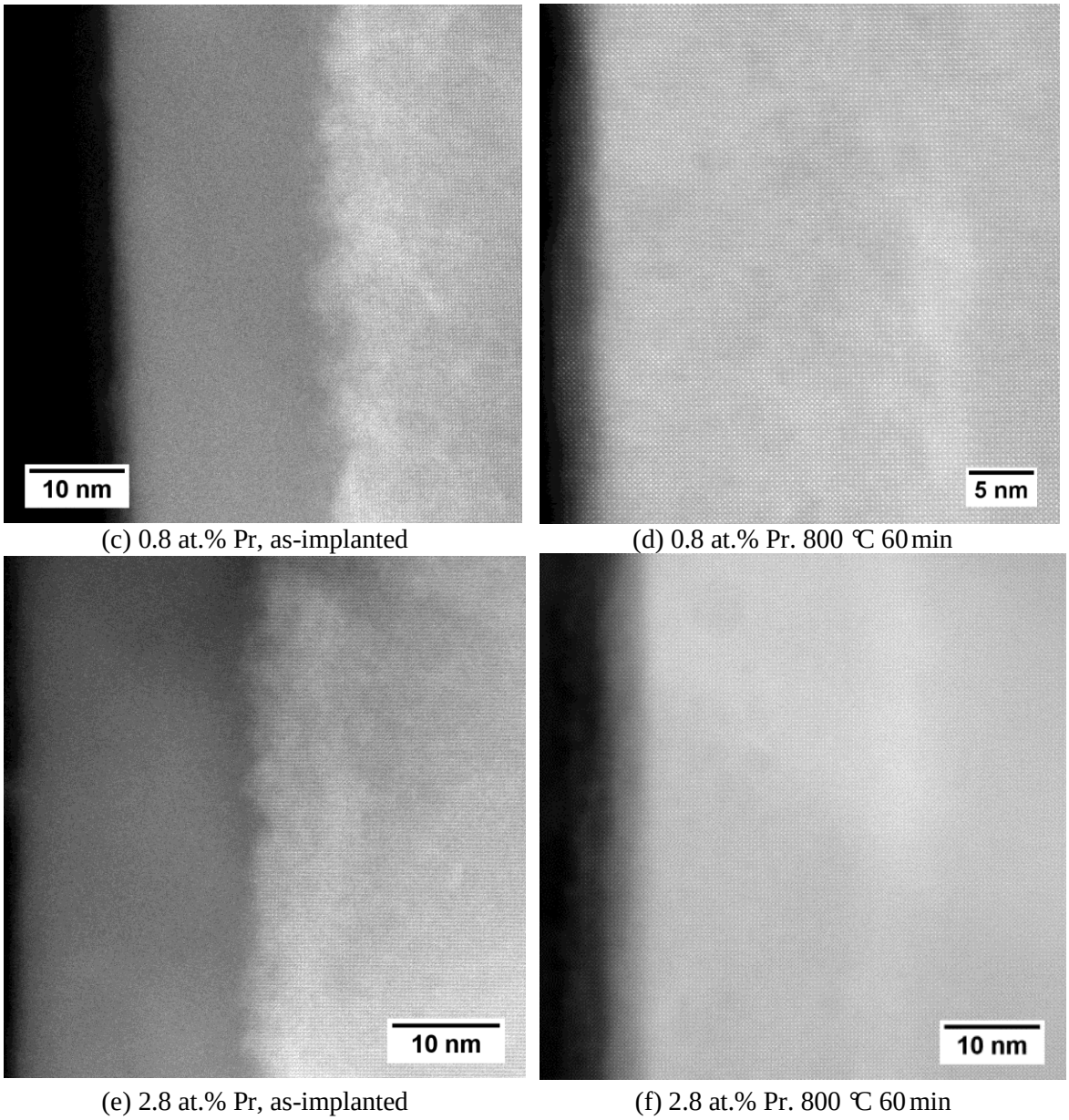

(c) 0.8 at.% Pr, as-implanted (d) 0.8 at.% Pr. 800 ℃ 60 min

(e) 2.8 at.% Pr, as-implanted (f) 2.8 at.% Pr. 800 ℃ 60 min

Figure 6-4 STEM-HAADF images of as-implanted (a, c, e) and annealed (800 ℃ for 60 min, and (b, d, f) $SrTiO_3$ single crystals with 0.2, 0.8 and 2.8 at.% Pr, respectively. The ions were injected from left to right into the bulk.

As stated in section 2.3.3.2, the thermal recrystallization process of ion-implanted-amorphized $SrTiO_3$ single crystals includes an initialization period and a linear growth period. The initialization period is not detectable under the present experimental

conditions. According to equation 2-1, the calculated re-growth rate during the linear growth period is 50 nm/min when Q = 0.77 eV [67], which predicts a full recrystallization after 400 ℃ annealing, in contradiction with present experimental results. A better agreement with experimental data can be achieved when Q = 1.2 eV [85], which implies a re-growth rate of 0.17 nm/min at 400 ℃ and 60 nm/min at 700 ℃. Although Q = 0.77 eV was derived by fitting the results of annealing experiments in air and Q = 1.2 eV was obtained in N_2, the partial H_2O pressure, not the atmosphere, was suggested as the key parameter affecting the value of Q in the literature[85]. Thus, similar H_2O pressure (i.e. very dry environment) was used at the present experimental conditions. On the other hand, the linear growth model cannot explain the final 7 nm depth amorphous layer after 700 ℃. It should be noted that different techniques such as Rutherford backscattering spectrometry (RBS)-channeling and time-resolved reflectivity (TRR) measurements have been applied to determine the recrystallized depth in the literature. However, these are not sensitive to the mosaic structure. Therefore, the activation energy (Q) does not seem to be constant and is highly related to the damage at different depth, which cannot be explained from the simple linear growth model suggested in the literature[85].

Since the beam-assisted recrystallization occurs only in as-implanted specimens with 2.8 at.% Pr peak concentration under normal STEM observation conditions (section 6.2.2), the correlation between the recrystallization and the damage caused by implantation can be achieved *in-situ* in the TEM. The incubation period is probably correlated to the 7-15 nm thick mosaic layer, which requires recovery instead of recrystallization. The linear growth period occurs in amorphized layers, probably under a layer-by-layer solid-phase epitaxy growth mechanism. The activation energy for re-growth must be closely related to the damage. As shown in figure 6-3(c) and figure 6-4(a), the damage in the outmost surface layer (~7 nm) is different, which offers an acceptable explanation for the stable 7 nm surface layer. Another possibility lies in the change of the solute concentration. As a possible result of surface effects, these injected ions are pushed from the bulk toward the surface; thus, the energy barrier for re-growth in the surface

layer is higher. The segregation of Al atoms in the surface layers is confirmed by the Al EDX map shown in figure 6-8.

Table 6-1 Summary of observed structure under TEM

(a) Specimens with 0.2 at.% Pr and 15 at.% Al

Temperature/℃	Time/min	Total affected region/nm	Amorphous/nm	Nano-particles	
as-implanted		38	25~30	Size/nm	Density n/line
400	5	43	28	--	--
400	60	42.5	30	--	--
700	5	37	6	Maybe a few	
700	60	40	6	0.8-1.9	9~12
800	180	40	0	0.8-1.9	10~14

(b) Specimens with 0.2 at.% Pr & 2 at.% Al and 9 at.% Al

Temperature/℃	Time/min	Total affected region/nm	Amorphous/nm	Nano-particles	
				Size/nm	Density n/line
as-implanted, 9 at.% Al		40	25	--	--
800	180	40	0	0.8-1.2	9~11
as-implanted, 2 at.% Al		33	25, not fully amorphized	--	--
800	180	33	0	1.2-2.3	5~6

(c) Specimens with 0.2 at.% Pr, 0.8 at.% Pr and 2.8 at.% Pr

Temperature/℃	Time/min	Total affected region/nm	Amorphous/nm	Nano-particles	
				Size/nm	Density n/line
as-implanted, 0.2 at.% Pr		~35	Layer with heavy defects, 7~13nm	--	--
800	60	38	0	3.5-5.0	<2
as-implanted, 0.8 at.% Pr		~35	20-22	--	--
800	60	~33	0	<1,~3	<2
as-implanted, 2.8 at.% Pr		30-33	21-24	--	--
800	60	~33	0	<1,~3	2-3

6.2.2 Electron-Beam-Associated Recrystallization

In order to elucidate the radiation-assisted recovery kinetics, we here present in-situ responses of $SrTiO_3$:Pr co-implanted with Al under a scanning electron beam. Beam-introduced recrystallization with larger electron flux is observed in Pr-implanted with 0.8 at.% and 2.8 at.% concentration as well as (Pr, Al) as-implanted with Al concentration of 15 at.%. As we mentioned in section 6.2.1, a ~25-30 nm thick amorphous layer and 7-15 nm thick mosaic crystalline layer are observed in the as-implanted specimens. The thickness of the amorphous layer decreases with exposure time to the scanning electron beam, which suggests in-situ epitaxial recrystallization at the amorphous/crystalline interfaces. Recrystallization is only detected within the region exposed to the electron beam and the amorphous/crystalline interface is not a straight atomic plane. In addition, starting with perfect {100} set of planes, the material follows an ideal layer-by-layer mode. It should be noted that we do not observe nano-clusters in the beam-assisted recrystallized region in the Pr-only specimen, as shown in figure 6-5.

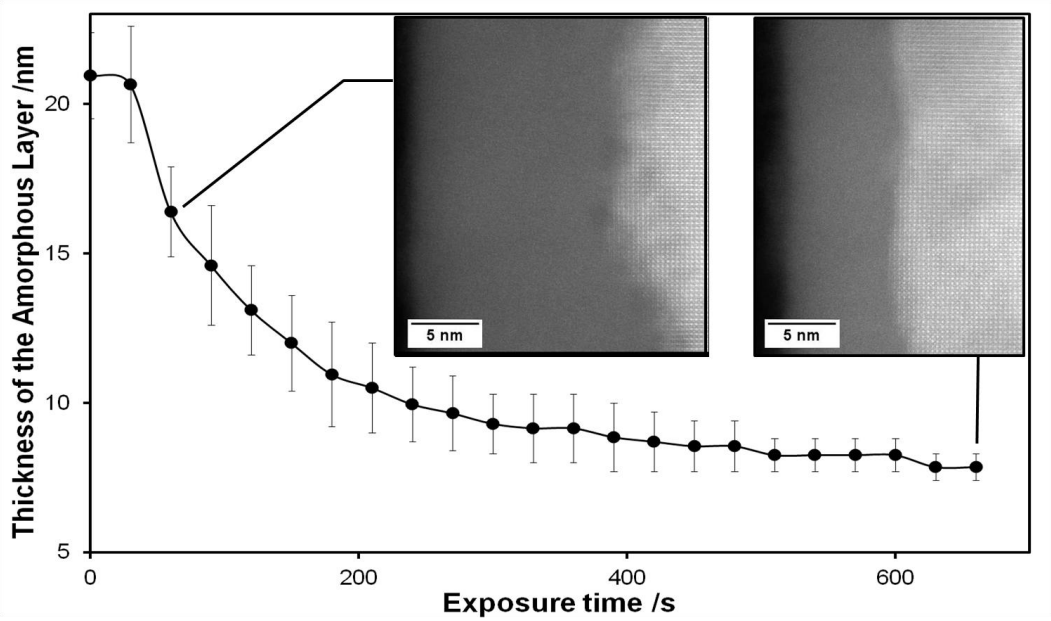

Figure 6-5 Re-crystallization in an as-implanted specimen with 2.8 at.% Pr under the exposure of a scanning e-beam. The estimation of the beam current is approximately 0.003nA (a radiation dose ~$10e^-/Å^2 \cdot s$)). The inserts are HAADF images at the selected frame. The thickness is measured as the average and error bars are treated as upper and

lower limits of the re-crystallization front. The dark contrast region in the HAADF images is the amorphous layer created during implantation and the bright contrast region is the recrystallized lattice.

Although the ion-implanted damage as computed by SRIM is the same, the electron beam flux required for recrystallization of the (Pr, Al) co-implanted specimens is tens of times lager compared to the Pr-only specimens. These results imply that the activation energy for recrystallization is much lower in co-implanted specimens, a likely result of the higher dose of injected ions present. The recrystallization processes are initialized very fast, then slowed down, and is obstructed. A roughly 7 nm thick amorphous layer is preserved even under much larger electron beam flux (Figure 6-5). This observation consists with the stable 7nm amorphous layer after 700 ℃ annealing. (see section 6.2.1) As suggested by Zhang et al[86], the beam-assisted recrystallization is likely due to localized electronic excitations that lower significantly the energy barriers for rearrangement of interfacial atoms.

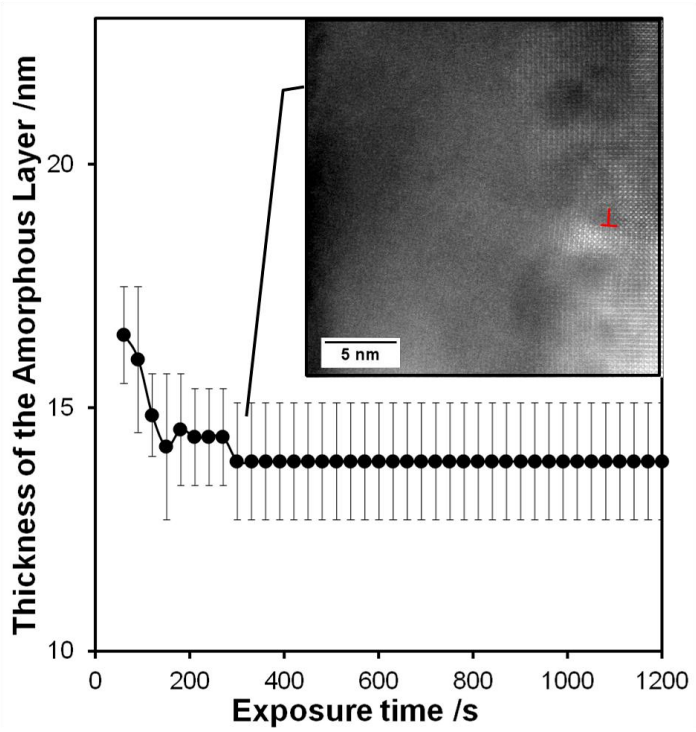

Figure 6-6 Recrystallization in an as-implanted specimen with 2.8 at.% Pr under the exposure of a scanning e-beam current of ~0.040nA (a radiation dose ~$10^2 e^-/(Å^2 \cdot s)$). The insert is the HAADF image at selected frame, which shows an edge dislocation core pinning the recrystallization front.

On the other hand, defects such as dislocations perpendicular to the recrystallization direction have a strong pinning effect on the recrystallization front as shown in Figure 6-6. It seems that the local atomic arrangement, e.g. the distortion and rotation of atomic polyhedral, may also have contributed to the beam-assisted recrystallization. The above measurement may confirm the hypothesis of contributions from the movement of atomic polyhedral pointed out by Zhang et al[86] as the possible subsequent effect of the atomic arrangement by localized electronic excitations.

The above hypothesis assumes that there are atomic polyhedra (i.e. short-range ordering) in the ion-amorphized $SrTiO_3$, which can be proven from the EEL spectra of the amorphous layer. As shown in figure 6-12 (a) and (b), Ti-O and Sr-O bonding character is clearly visible in the low-loss EEL spectra of the amorphous region. Although these peaks are different in shape and intensity compared to those of the ideal bulk, the Ti-O (in the energy window of 3-15 eV) and Sr-O (in the energy window of 15-30 eV) intra-band transitions are confirmed by the appearance of these peaks at the corresponding energy positions. In short, short-range ordering such as atomic polyhedra is confirmed in the amorphous layer, which is similar to the liquid and glass phase.

6.3 NANO-CLUSTERS

Instead of the expected bright spots from heavy Pr^{3+} ions in (Pr, Al) co-doped specimens, the cuboidal-shaped nano-clusters of about 0.8-2.4 nm size are visible in STEM-HAADF images showing a reduced intensity with respect to the STO background and an enhanced intensity in STEM-ABF images. Although all TEM images are the projections of 3D objects, the cuboidal shape nano-clusters are confirmed from observations carried out on cross-sectional specimens prepared with a 90˚ rotation. These clusters were observed only in the recrystallized layers within all (Pr,Al) co-implanted specimens. Within these nano-clusters, the same periodic structure is well kept compared to the bulk.

In the Z-contrast HAADF images, the reduced contrast from these nano-clusters implies these atomic columns have a smaller mean atomic number (smaller Z), probably due to segregation of Al atoms (Figure 6-7). Therefore, we simulated the STEM-ABF and HAADF images containing an Al-rich cluster according to the experimental conditions. The simulated model consists of an Al_{16} cluster sitting in a 5 nm thick $SrTiO_3$ specimen corresponding to the typical dimension of these clusters and the typical thickness of a specimen. The experimental image of the Al-cluster provides similar bright contrast as found in the simulated ABF image and comparable dark contrast as found in the simulated HAADF image. Based on these observations and the simulated images, the results suggest that these nano-clusters are Al-rich clusters.

Besides the above contrast test, both null and concentration tests proposed by Voyles[95] were performed to further support the compositional fluctuation within these nano-clusters. Firstly, no such nano-clusters were observed in blank (unimplanted) specimens and very few nano-clusters with irregular shape were recorded in the annealed specimens with only Pr injected ions. These irregular shape clusters may be due to the form from oxygen vacancies (V_O) to compensate the charge difference between Sr^{2+} ions and Pr^{3+} ions. Secondly, under the reasonable assumption that most dopants are sitting within these nano-clusters, the theoretically expected number of clusters found in a specimen with 0.2 at.% Pr peak concentration and 2 at.% Al peak concentration roughly agrees with the total number of dark regions counted from the experimental images. The experimental images were taken from regions with a typical thickness of 10 nm (25 unit cells). There are roughly 6 nano-clusters with an average size of 1.6 nm (4 unit cells) can be interpreted by a line along the implantation direction within the implantation regions (20 nm in width, corresponding to 50 unit cells). In short, roughly 6 nano-clusters are contained in a 3-dimensional bulk with a size of 25x6x50 unit cells. This corresponds to a 0.12 at.% Pr and a 1.9 at.% Al average concentration within the implantation region under the reasonable assumption that one nano-cluster contains one Pr and sixteen Al atoms. The above calculated concentration fully agrees with the experimental concentration of the present specimen.

In addition to these nano-clusters present in the HAADF and ABF images (Figure 6-7), areas with butterfly shape contrast with a diameter of ~5 nm right at the implantation front suggest the presence of a strain field around dislocations. (see the detailed discussion in section 6.5)

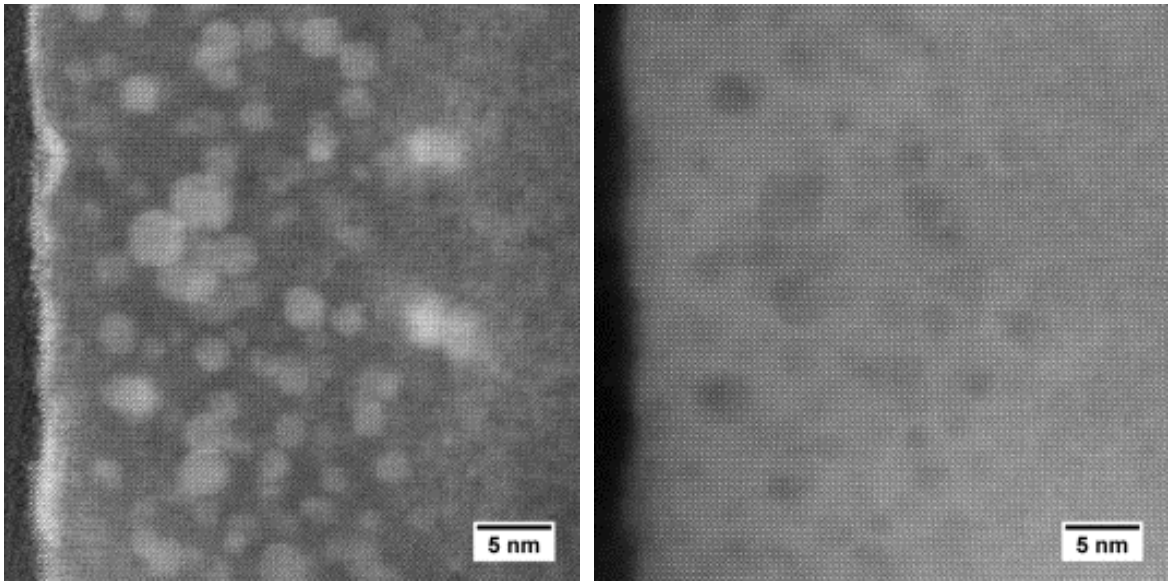

(a) experimental, ABF (b) experimental, HAADF

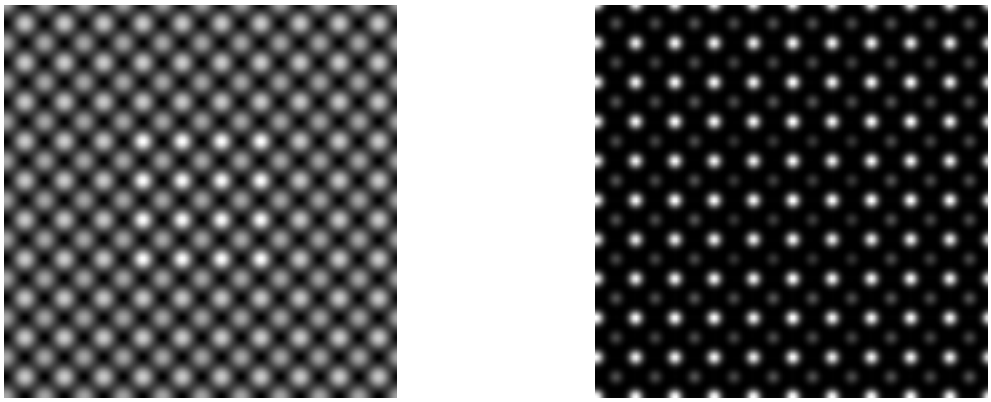

(c) simulated, ABF (d) simulated, HAADF

Figure 6-7 Experimental and simulated STEM-ABF and HAADF images of the nano-clusters. The experimental images are taken with the convergence angle of 17.5mrad under 200 kV from implanted regions annealed at 800˚C for 180 min in the specimens with 0.2 at.% Pr and 2 at.% Al. The ABF and HAADF detectors collect the signal of 10-46 and 75-163 mrad, respectively. The simulated images based on an Al_{16} cluster sitting in a 39x39x51 Å super-cell. Sixteen Al atoms substitute adjacent Ti-sites, in which four neighboring atomic columns contain four adjacent Al atoms each.

6.3.1 Detectability of Dopants

In order to investigate the occupied lattice sites of Pr^{3+} and Al^{3+} ions, chemical characterization by EDX and EELS was carried out. Although the detection of Pr signals in the specimens with 0.2 at.% Pr peak concentration is not convincing, the Pr $M_{4,5}$-edge is clearly visible in the EEL spectra taken from specimens with 2.8 at.% Pr concentration. In addition, Pr ions are only detected at some of the Sr-sites as demonstrated in the atomic EELS map in figure 6-8. The regions with Pr signals seem slightly large compared to the atomic size in the HAADF image, which can be attributed to the broadening effect of the ionization interaction[124]. Al EDX signals were recorded in both as-implanted and re-crystallized (Pr, Al) co-doped specimens. Of particular importance, although the maps do not allow to determine whether the Al is only in the clusters due to the possible overlap of regions, more Al EDX signal, less Ti signal and no compositional change in O signals were detected within the regions containing higher density of these nano-clusters (Figure 6-9), which further confirms that these nano-clusters have a different chemical composition.

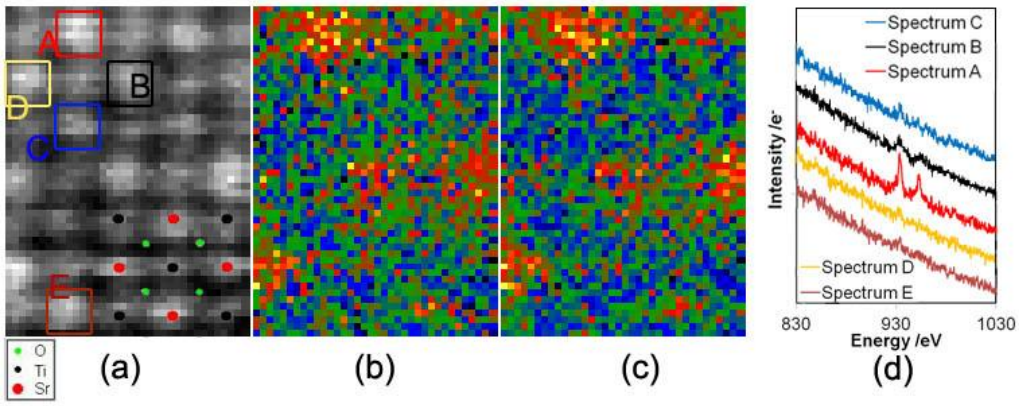

Figure 6-8 EELS map of Pr dopants within a $SrTiO_3$ lattice. (a) the HAADF image acquired simultaneously with a EEL spectrum image; (b) the elemental map of Pr dopants from the raw data; (c) the elemental map after removing noise by principal component analysis (PCA); (c) the raw EEL spectra from selected areas in (a).

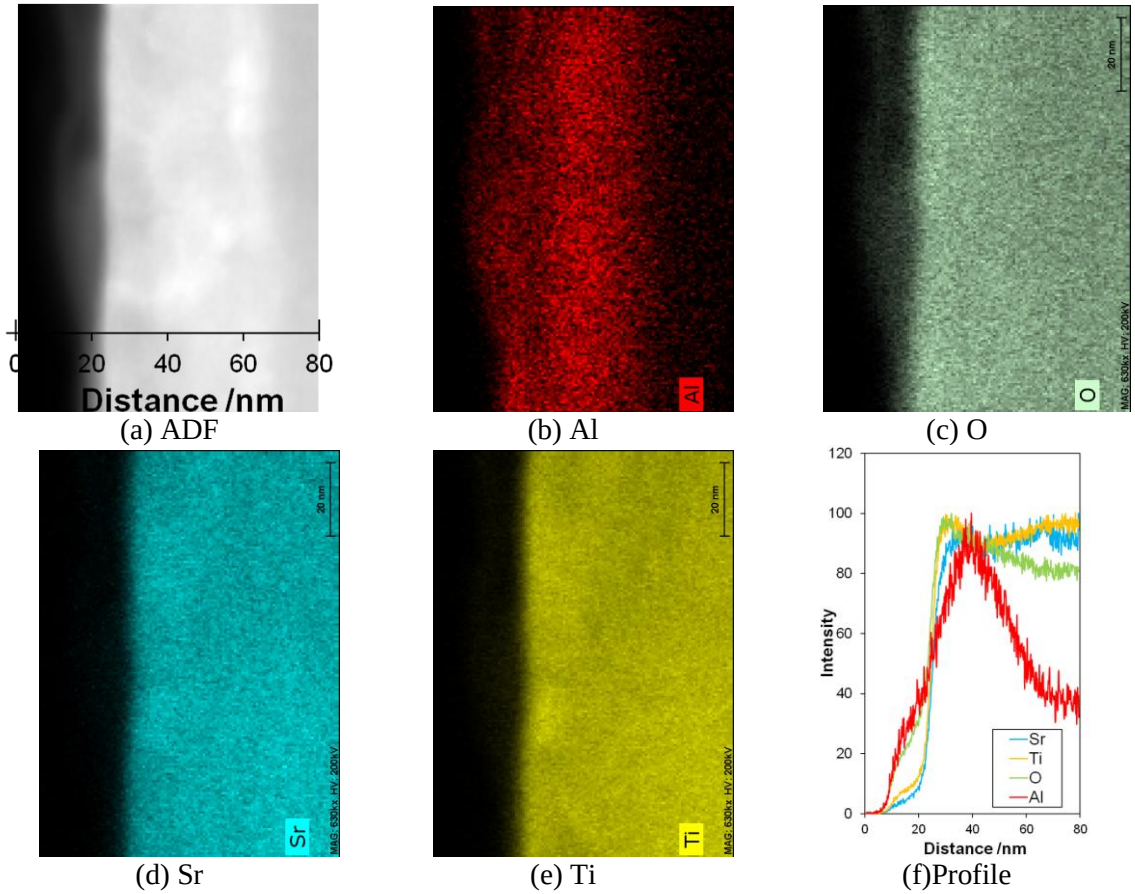

(a) ADF (b) Al (c) O

(d) Sr (e) Ti (f)Profile

Figure 6-9 EDX map of the implanted regions in the annealed specimens with 0.2 at.% Pr and 9 at.% Al peak concentration .

6.3.2 Associated Electronic Structures

In order to investigate local crystal fields from these nano-clusters, Ti $L_{2,3}$-edge and O K-edge EEL spectra were recorded from the region containing a nano-cluster and compared with the adjacent lattice. Since these nano-clusters are cube-like, EEL signals contributed by a nano-cluster can be evaluated from the dimension of the nano-cluster compared to the local thickness of the TEM foil. Under the reasonable assumption that the thickness of the sample is the same in both regions we can extract the linearly fitted Ti $L_{2,3}$-edge spectrum of the nano-cluster via linear combination analysis and the thickness of the nano-cluster from its measured dimensions. The retrieved spectrum shows strong similarities with that of TiO_2 which implies that the formal valence state of

Ti ions is unchanged and the shape of the TiO_6 groups are distorted as compared to the Ti environment in $SrTiO_3$ (Figure 6-10(a)). The slight changes in the O K-edge EEL spectra are probably attributed to the following: a) the presence of Vo, and/or b) the presence of AlO_6 groups (and/or PrO_{12} groups) instead of TiO_6 groups (and/or SrO_{12} groups).

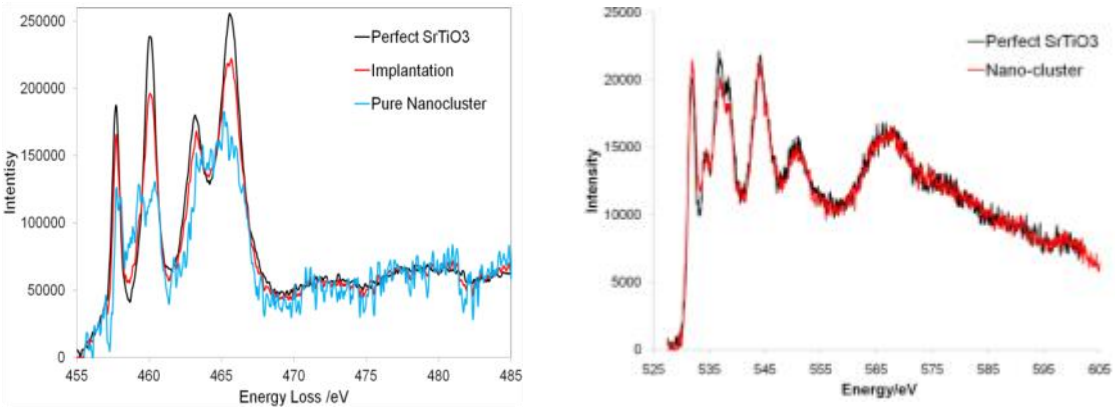

(a) Ti $L_{2,3}$-edge (b) O K-edge

Figure 6-10 Ti $L_{2,3}$ edge (a) and O K-dege (b) EEL spectra of the un/implanted regions annealed at 800˚C for 180min in the specimens with 0.2 at.% Pr and 2 at.% Al. In (a), the spectrum of the nano-cluster is obtained by extracting the component contributed from the nano-cluster via linear combination and known thickness.

6.3.3 Electron-Beam Damage Behaviors

In order to further elucidate the possible void origin of these nano-clusters, the behavior of these nano-clusters under electron beams was investigated and found to be very different compared to the bulk, which implies that the composition difference is a non-negligible parameter of such nano-clusters. Under the high dose electron flux used for the acquisition of EEL spectra image, which is usually tens of times larger than the flux used under normal imaging conditions, these nano-clusters are damaged but recover soon and form a comparable stable phase These new phases have an entirely different periodic pattern compared to the original nano-clusters. The presence of Pr ions and weak Ti signal from the EEL spectra suggests different local chemical environments within these nano-clusters compared to the bulk. As a consequence, the energy barrier to rearrange atoms is much lower. (Figure 6-11)

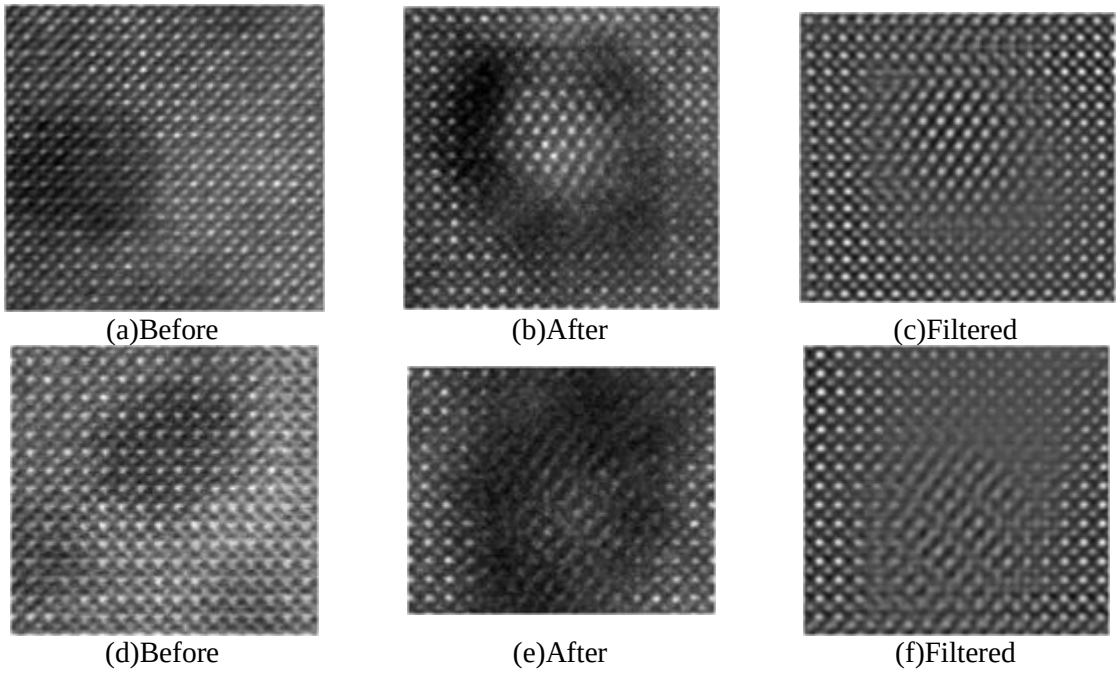

Figure 6-11 The recovery of beam-irradiated nano-clusters within the annealed $SrTiO_3$. (a) and (d) are the HAADF images of the stable atomic structure under the exposure of scanning electron beam current of approximately 0.003nA (a radiation dose of ~$10e^-/Å^2 \cdot s$)), respectively. (b) and (e) are the HAADF images of the same regions in (a) and (d) after acquisition of EEL spectrum images, respectively. The spectrum images were taken under a beam current of ~0.100 nA (~$2 \times 10^2 e^-/Å^2 \cdot s$). (c) and (f) show the Fourier Filtered atomic structure of (b) and (e), respectively.

6.4 ELECTRONIC STRUCTURES

The associated electronic structure was investigated by EELS in order to assess the role of the injected ions on the optical properties. The determination of electronic state from low-loss EEL spectra is complex because of the intense zero-loss peak as well as the superimposition of Cerenkov losses and surface modes within its tail[125]. The contribution of Cerenkov loss can be modeled as a flat and weak background in the energy window before the band-gap as simulated from a *MATLAB* code[126] (See Appendix 4). In other words, no strong feature is caused by Cerenkov losses, which simplifies comparisons of spectra taken from different regions. In the experimental conditions selected for the measurements, surface contribution terms were neglected compared to

the huge bulk contribution because all the low-loss EEL spectra were taken at a thickness of about two mean free paths.

As shown in low-loss EELS spectra in figure 6-12(a), (c), (e), (g) and (i), the joint density of states (JDOS), related to the signal windows of 0-15 eV, are more intense in the implanted regions compared to the un-implanted ones. The intense JDOS in the implanted materials is additionally confirmed by the ellipsometric spectra presented as the insert in figure 6-12(g). Although the ellipsometric spectrum integrates both the signals from the crystallized layer and the bulk, the spectrum for the recrystallized layer is extracted based on the known spectrum of the ideal bulk. The intense JDOS within the band-gap (i.e. 3.4eV) suggests the existence of defect levels, which may confirm the existence of the inter-valence charge transfer (IVCT) bands, as suggested from the PL spectra in section 6.1 and the literature.

In order to a achieve more precise description for the JDOS, the acquired low-loss EEL spectra was firstly aligned at the zero-loss peaks (ZLPs), and then corrected for the multiple scattering events by the Fourier-log deconvolution method, and finally computed as the dielectric function based on a Kramers-Kronig analysis. The Fourier-log deconvolution method is used to remove the ZLP by fitting its tail within the energy window before the band-gap (i.e. 0.5-3 eV), which may underestimate the signals contributed by possible defect levels within this energy window. Accordingly, the interband transition strength J_{cv} (the imaginary part ε_2 of the dielectric function) can be calculated as shown in equation 6-1 [127].

$$\varepsilon_2(E) \propto \frac{1}{E} \int_{E_f - E_i = const.} \frac{dS}{|\nabla_{\mathbf{k}}(E_f - E_i)|} \qquad \text{Equation 6-1}$$

In which, the integral is known as the joint density of states (JDOS), E_f and E_i are the energies of the final and initial states in the involved interband transitions, $\boldsymbol{k}$ is the wave vector. As shown in the black curves in figure 6-12(f) and (h), the spectra within the energy window just after band-gap (i.e. 3-4 eV) have double parabolic shapes in the perfect bulk, which correspond to the direct and indirect band-gap. The sharp change after the band-gap present in the spectra of the recrystallized layers confirms the

existence of defect levels within band-gap. Compared to the ε_2 spectra obtained in the recrystallized layer within the Pr-only specimens (figure 6-12(g)), a different shape of the ε_2 spectra was obtained in the recrystallized layer in the specimens with 2 at.% or 9 at.% Al peak concentration (figure 6-12(f) and (h)), indicating that there are different defect levels within band-gap as referred to the low-lying intervalence charge transfer (IVCT) bands. The above measurement is consistent with the theory about the bulk-shift of the red emission peak in section 6.1, in which different low-lying IVCT bands are presented depending on whether or not Al ions are around Pr ions.

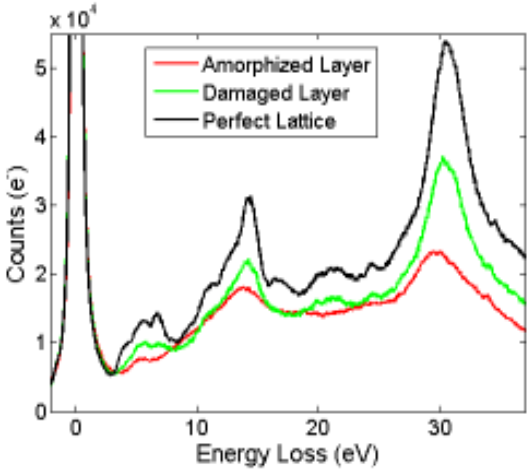

(a) As-implanted, 0.2 at.% Pr and 15 at.% Al, EELS

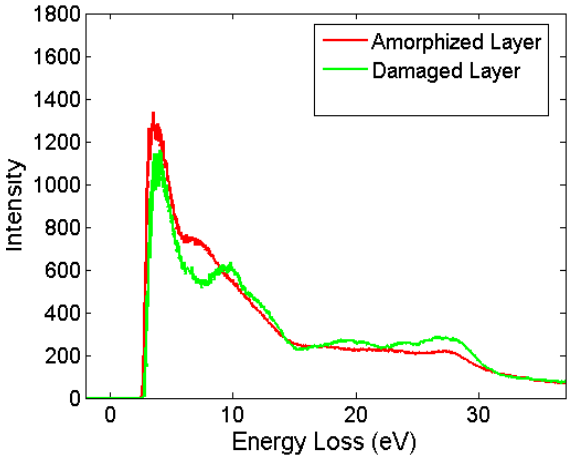

(b) As-implanted, 0.2 at.% Pr and 15 at.% Al, ε_2

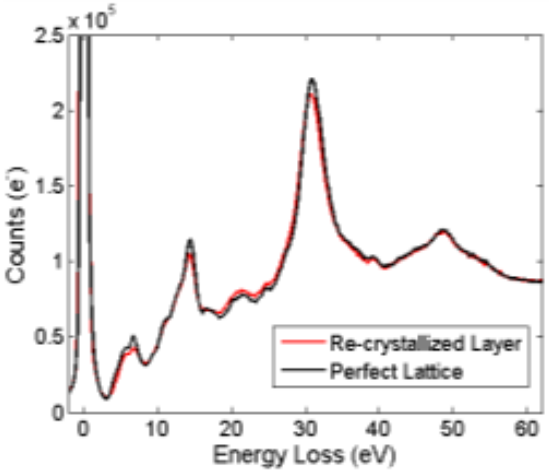

(c) Annealed, 0.2 at.% Pr and 15 at.% Al, EELS

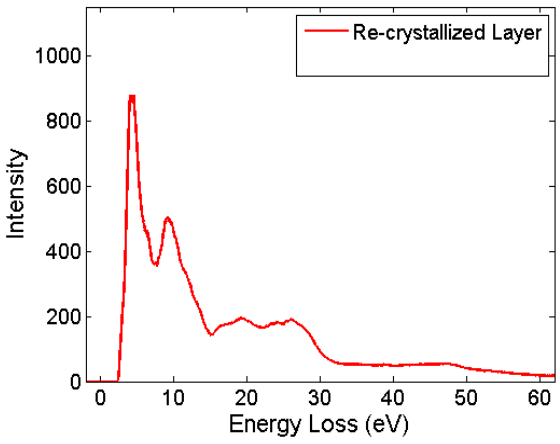

(d) Annealed, 0.2 at.% Pr and 15 at.% Al, ε_2

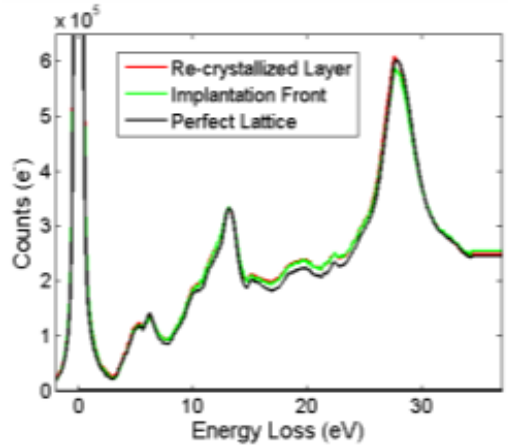

(e) Annealed, 0.2 at.% Pr and 9 at.% Al, EELS

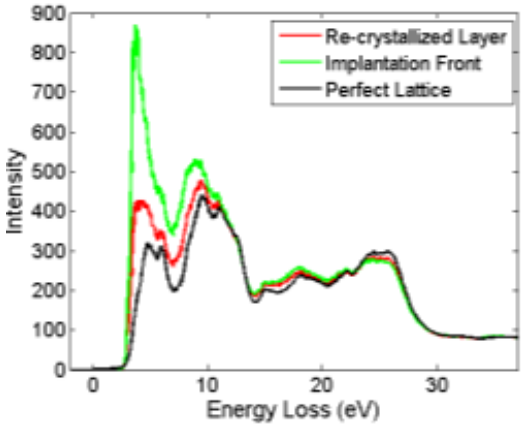

(f) Annealed, 0.2 at.% Pr and 9 at.% Al, ε_2

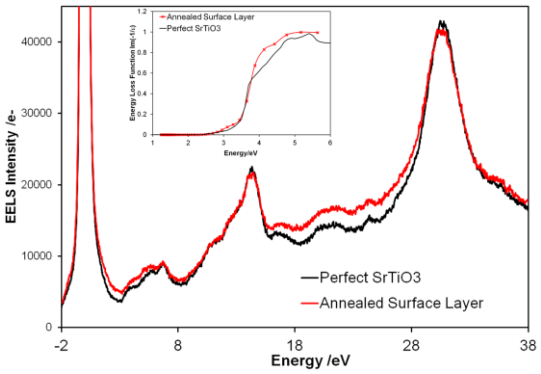

(g) Annealed, 0.2 at.% Pr and 2 at.% Al, EELS. Inserted: ellipsometric spectra.

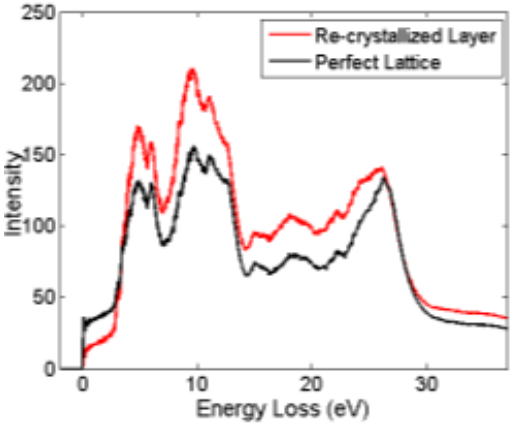

(h) Annealed, 0.2 at.% Pr and 2 at.% Al, ε_2

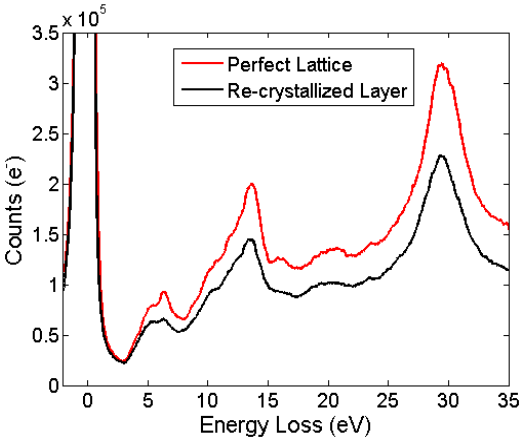

(i) Annealed, 0.2 at.% Pr, EELS

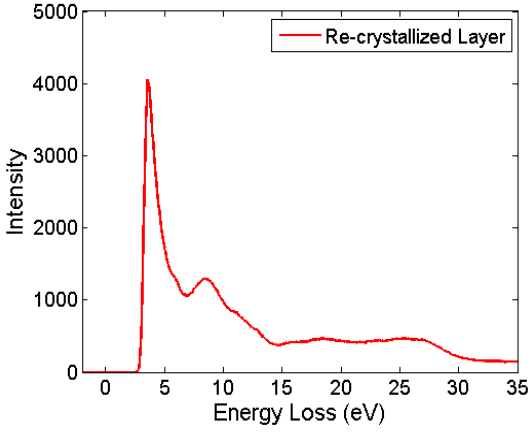

(j) Annealed, 0.2 at.% Pr, ε_2

Figure 6-12 The low-loss spectra of the un/implanted regions in the as-implanted and annealed specimens at 800 ˚C for 180 min. (a) and (b) were taken with the convergence angle of 7.8 mrad and a collection angle of 13 mrad at 200 kV. (c)-(j) were taken with a convergence angle of 15 mrad and a collection angle of 19 mrad at 80 kV.

The corresponding peaks are assigned to specific intra-band transitions as summarized in Table 6-2[128]. The peaks corresponding transitions between O 2p–Ti3d t_{2g} (3-8 eV) and e_g (8-15 eV) typical of crystalline $SrTiO_3$ are strongly enhanced in the region containing these injected ions compared to the bulk features obtained in the unaltered lattice further away from the implanted and crystallized region while the transitions between O and Sr (15-30 eV) exhibit only minor changes, except within ion-amorphized layer. This suggests there are large changes in the Ti 3d bands, indicating changes of the local ligand field around Ti ions. The change of the local ligand field is strongly depended on the positions of O ions with respect to the Ti ions within TiO_6 octahedra. These measurements additionally suggest the presence of distorted TiO_6 octahedra, consistent with our previous conclusion of Al-rich nano-clusters in section 6.3. All these local changes are further enhanced right at the implantation front separating the unaffected lattice and the recrystallized region where we have observed partial disorder and dislocations with strongly distorted TiO_x octahedra.

Table 6-2 Peak position (in eV) and the corresponding phenomena[128]

(a) Energy loss function

Peak position	5.7	6.7	11.3	14.7	17.2	21.1	24.5	31.0	50.2
	I	I	I	I	I	I	I	P*	I

Notes: I stands for the inter-band transition and P for the Plasmon.

(a) Inter-band transition energy

Peak position	5.0	6.6	10.2	11.8	13.4	16.7	20.0
Transitions	O2p-Ti 3d t_{2g}	O2p-Ti 3d t_{2g}	O2p-Ti 3d e_g	O2p-Ti 3d e_g O2p-Sr 4d	O2p-Sr4d	Sr4p-Ti 3d t_{2g}	Sr 4p-Ti 3d e_g
Peak position	24.3	26.4	27.9	-	47.0		
Transitions	?	?	?	?	?		

In summary, the results confirm the existence of the low-lying intervalence charge transfer (IVCT) states, the energy of which increases when Al ions replace Ti ions. It should be noted that the low-loss EEL spectra are consistent with a large absorption of 615 nm photons than 605 nm photons, which excludes the possibility of a higher re-absorption of the emitted 605 nm photons compared to 615 nm photons. This suggests

that the higher yield of 615 nm photons from (Pr, Al) co-implanted specimens is likely caused by the Al ions. Thus, Al ions affect the energy transfer to Pr^{3+} ions and the release process of intra-4f transitions of the Pr ions but not the re-absorption of the emitted photons.

6.5 LINEAR DEFECTS WITHIN IMPLANTATION REGIONS

During implantation, the damage is caused by high energy injected ions, which lose their energy by displacing host ions, especially for those heavy ions injected at lower energy. At the same time, dynamic recovery occurs, during which point defects aggregate and form dislocation loops. At the boundaries between crystalline domains with a diameter of a few nm in the mosaic structure, dislocations or semi-coherent planes are usually present. As shown in figure 6-13, a high density of dislocations (~10 nm in length) was detected in the as-implanted specimens. It should be noted that PL spectra in section 6.1 were recorded from reflected light instead of transmitted light from the back side of specimens, thus the effect of dislocations on the PL luminescence may not be fully detected.

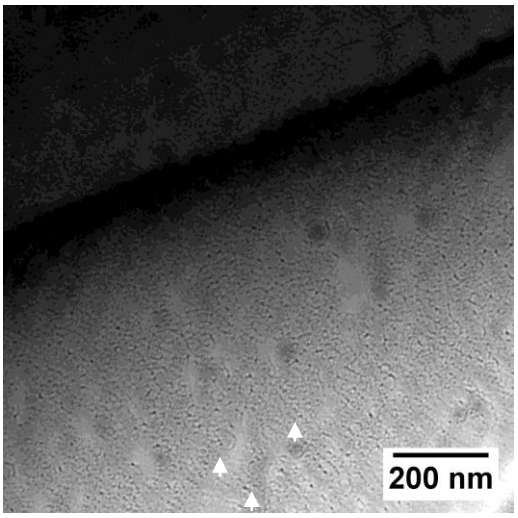

Figure 6-13 Dislocations in the plane-view as-implanted specimens with 0.2 at% Pr and 15 at.% Al peak concentration. The black lines in this micrograph are the dislocation lines, labeled by white arrows.

After annealing, these mosaic structures recover. As a result, dislocation loops are preserved and are observed as identifiable features at the implantation front. As mentioned in section 6.2, the extent of dislocations present in the recrystallization layer highly depends on the extent of damage and the concentration of injected ions.

In this section, we first present the evidence for dislocation loops at the implantation front, following by that for dislocations parallel and perpendicular to the plane of the implantation front, which affect structure evolution such as recrystallization as discussed in section 6.2.2. We will discuss the type of dislocation cores and associated strain field, which contribute to the contrast observed ABF and BF images.

6.4.1 Dislocation Loops

Since dislocations cannot start and end within a perfect lattice, dislocations either start from the surfaces of amorphous layers or they form dislocation loops within a lattice which can be detected in as-implanted specimens. As shown in figure 6-14, dislocations with ~10 nm length were observed, which is consistent with the result shown in figure 6-13. Strain mapping, computed from the geometric phase analysis (GPA) package attached to Digital Micrograph, which is based on the detected displacement of atomic columns in the lattice image, highlights these dislocations and their cores.

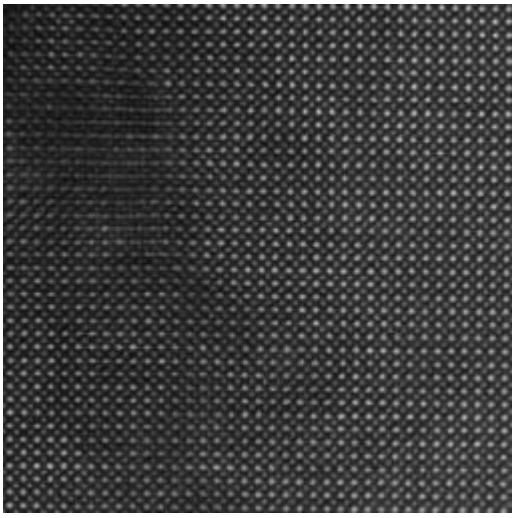

(a) HAADF image

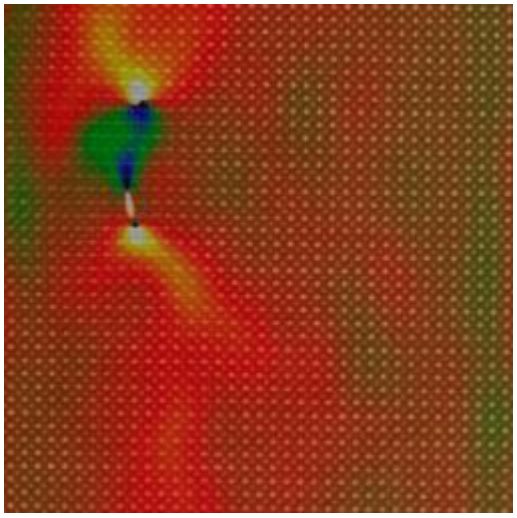

(b) ε_{xx}

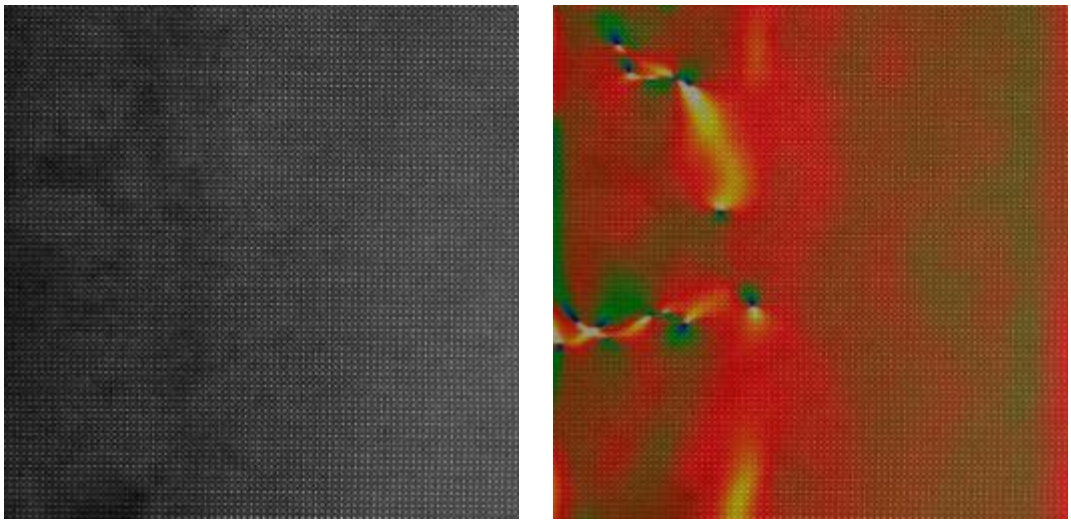

(c) HAADF image (d) ε_{xx}

Figure 6-14 Implantation front from a cross-section view in as-implanted specimens with 0.2 at.% Pr and 15 at.% Al. The amorphous layers are not shown but are at the left of these crystalline layer in above images. (a) and (c) are HAADF images containing the implantation front. (b) and (d) are the calculated strain mapping of normal strain along the horizontal direction ε_{xx} based on (a) and (c), respectively.

Dislocation loops are mainly detected at the implantation front, in both as-implanted (Figure 6-14) and annealed specimens (Figure 6-15). As shown in figure 6-15, the bright regions of ABF images around dislocations correspond to the strain field around dislocations. Of particular importance, there is no detectable relationship between cubed-shape nano-clusters and computed strains measured with the GPA, which implies the bright contrast from nano-clusters are not caused by local strain. (see Figure 6-15(b), (c) and (d))

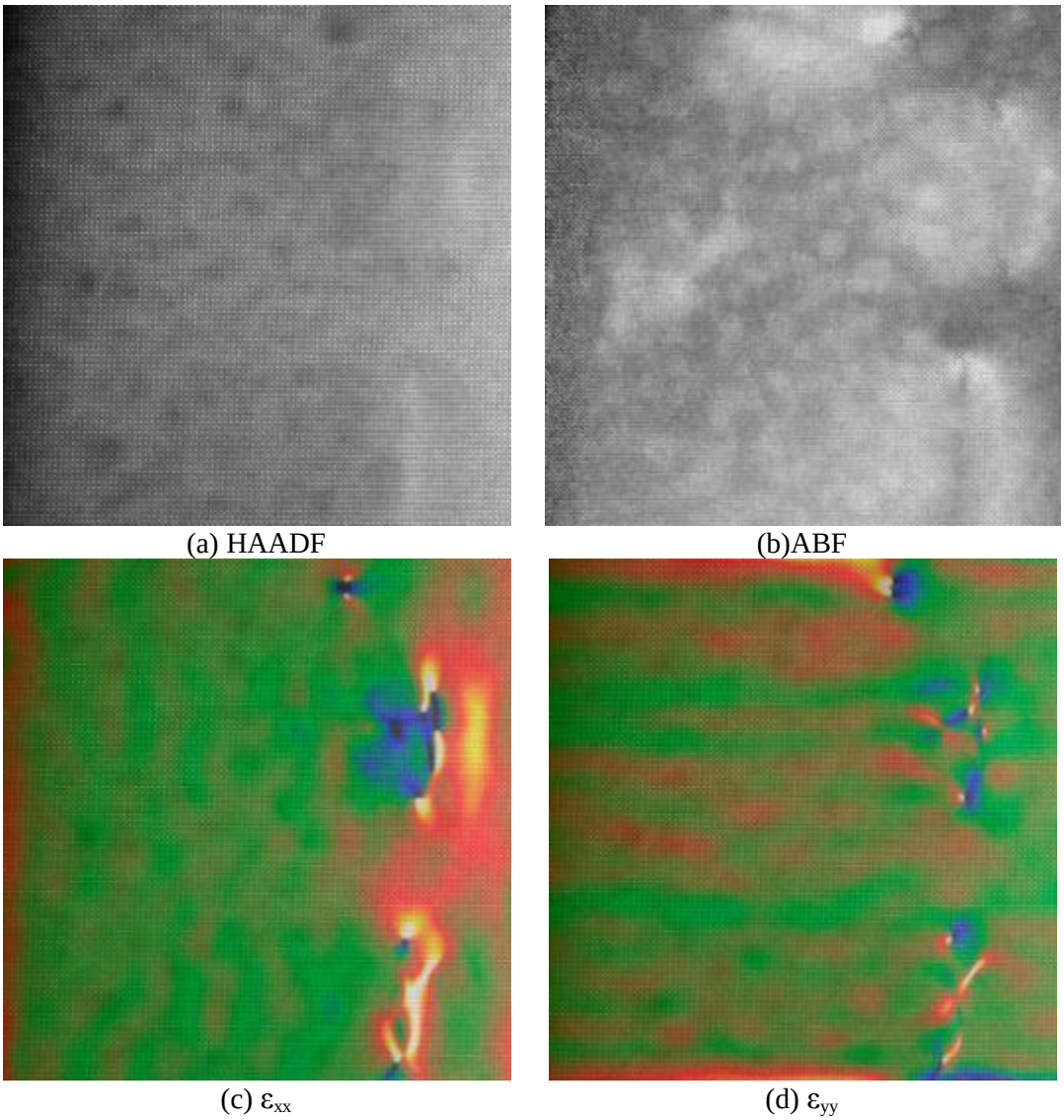

(a) HAADF (b)ABF

(c) ε_{xx} (d) ε_{yy}

Figure 6-15 Dislocations involved in the implantation regions within the annealed specimens with 0.2 at.% Pr and 9 at.% Al. (a) and (b) are the HAADF image and the simultaneously acquired ABF image, respectively. (c) and (d) are the computed strain mapping based on (a). (c) and (d) are the normal strain along the horizontal ε_{xx} and vertical directions ε_{yy}, respectively.

6.4.2 Dislocation Cores

As shown in figure 6-16, an edge dislocation core with a Burger vector of <100> direction is a simple dislocation core with the extra atomic plane almost perfectly located

in the middle of two other atomic planes. Around the dislocation core, consisting of highly mismatched atomic columns, a butterfly shape strain field ε_{xx} and a dumbbell shape strain field τ_{xy} are measured with the GPA, which are very similar to the strain field simulated with a simple dislocation model in an isotropic matrix (see figure A5-1(c) and (e) in Appendix 5). It should be noted that the dislocation model in Appendix 5 contains no information about the dislocation cores, which is beyond the capability of elasticity theory. However, the strain field ε_{yy} has a distorted dumbbell shape, deviating from the ideal shape calculated in figure A5-1(d). The above deviation can be explained through the non-symmetric atomic arrangement within this dislocation core along the horizontal directions.

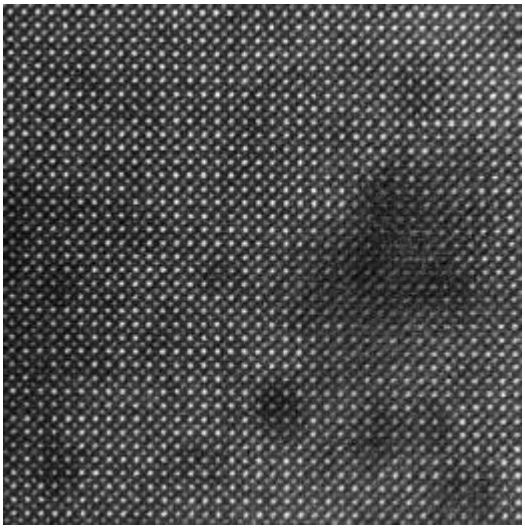

(a) HAADF

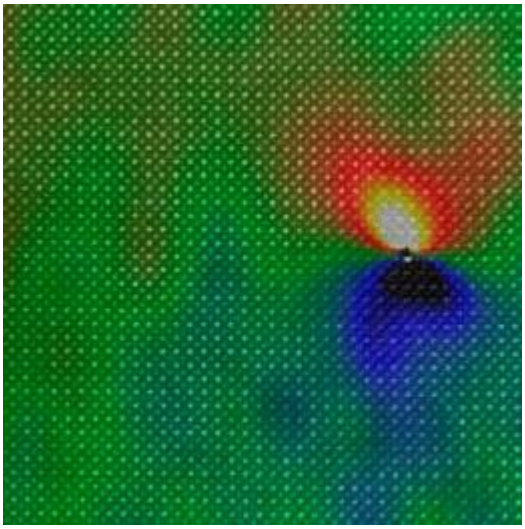

(b) ε_{xx}

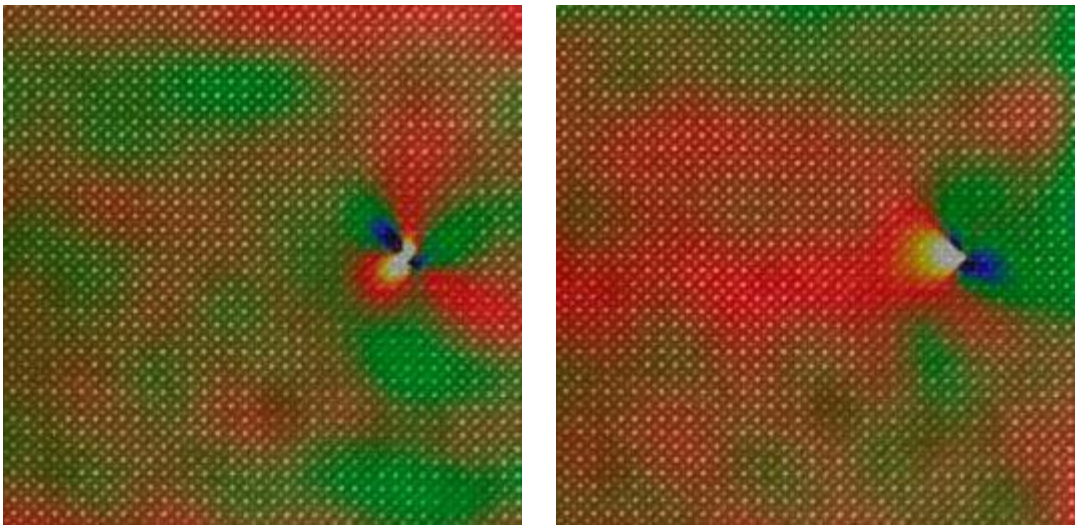

(c) ε_{yy} (d) τ_{xy}

Figure 6-16 Edge dislocation core present in the implantation regions in the specimens with 0.2 at.% Pr and 15 at.% Al annealed at 700 ℃ for 60 min. The strain field is calculated using a group of <110> reflections through the GPA package based on the HAADF image as shown in (a). (b) and (c) are the normal strain along the horizontal ε_{xx} and vertical directions ε_{yy}, respectively. In (d), τ_{xy} is the shear strain corresponding to the x-y plane.

Within a complex oxide lattice such as $SrTiO_3$, complex dislocation cores are expected because a simple dislocation core requires the absence of both Ti-O columns and Sr columns. A couple of partial dislocation cores are presented along <100> crystallographic directions with a Burger vector along <010> directions, as shown in figure 6-17. Another type of dislocation core contains two partial dislocation cores with Burger vector of b= ½<110>, as shown in figure 6-18. The strain fields around them have a butterfly shape pinned at two maxima. At each of the two maxima, the dumbbell shape of the strain fields gives an acceptable agreement with the strain fields deduced from the simple dislocation model (see figure A5-1). Of particular importance, the non-isotropic strain around them seems highly correlated with the dark contrast in the BF images (Figure 6-18(d)). In conclusion, these strain fields not only identify the dislocation types but also provide an acceptable explanation to the contrast observed in ABF and BF images.

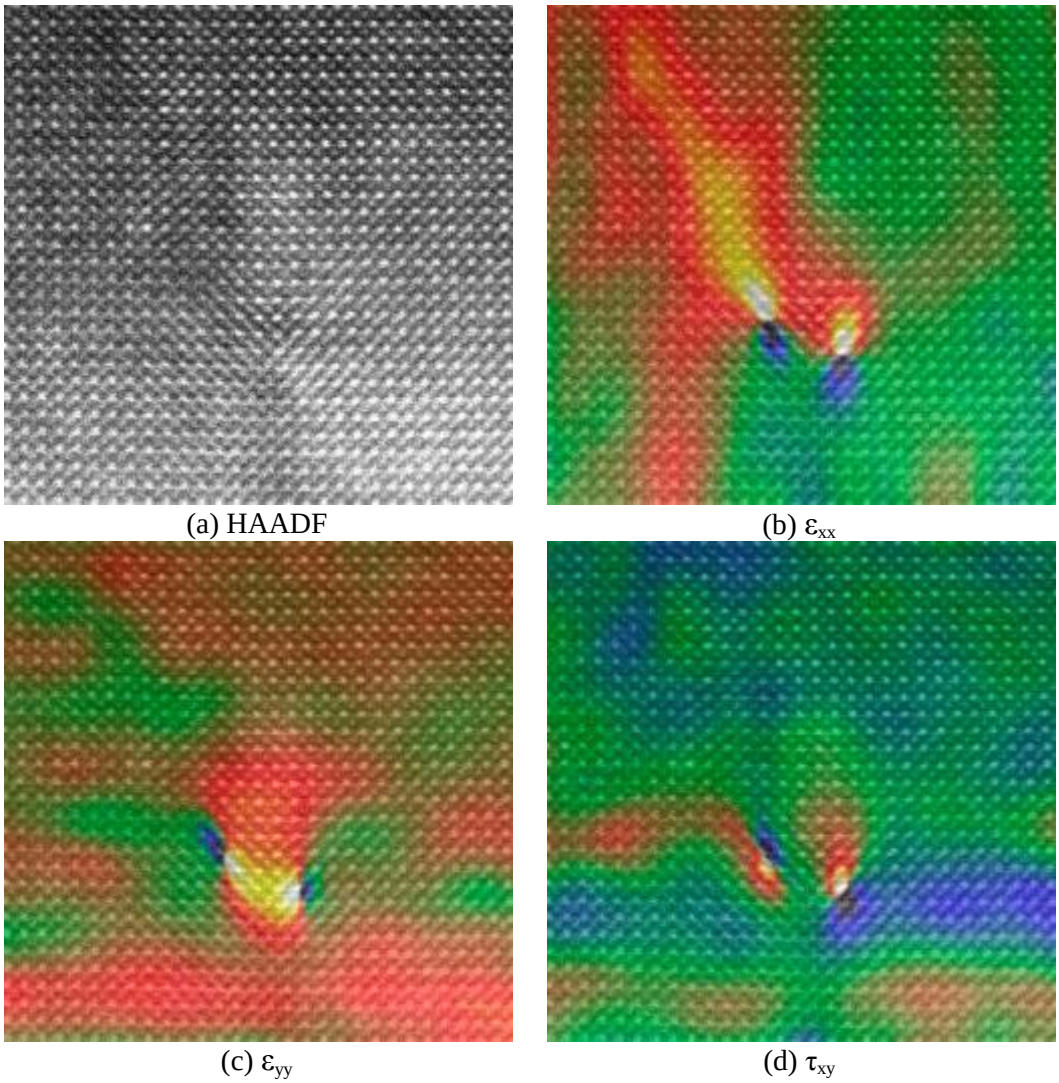

(a) HAADF (b) ε_{xx}

(c) ε_{yy} (d) τ_{xy}

Figure 6-17 Regions with two partial dislocation cores in the specimen with 0.2 at.% Pr and 15 at.% Al annealed at 400 ℃ for 60 min. The strain field is calculated using a group of <110> reflections through the GPA package based on the HAADF image as shown in (a). (b) and (c) are the normal strain along the horizontal ε_{xx} and vertical directions ε_{yy}, respectively. In (d), τ_{xy} is the shear strain in the x-y plane.

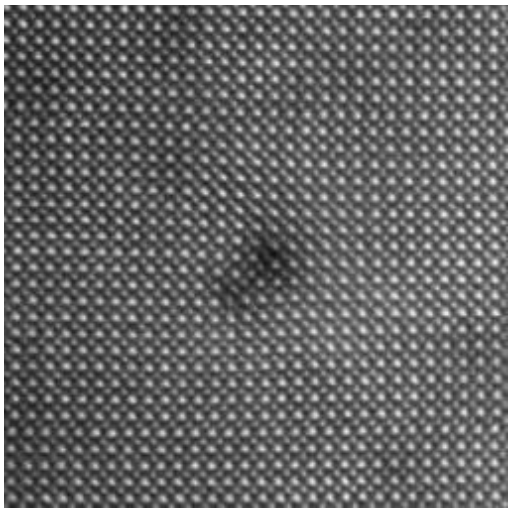

(a) HAADF

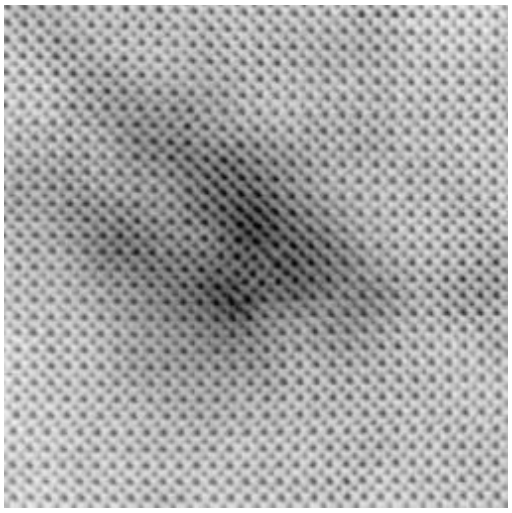

(b) BF

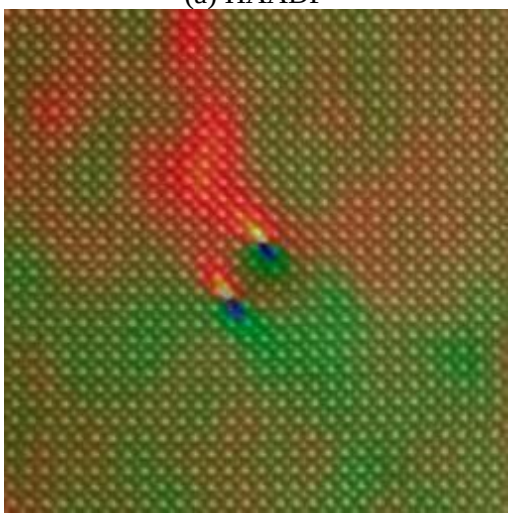

(c) ε_{xx}

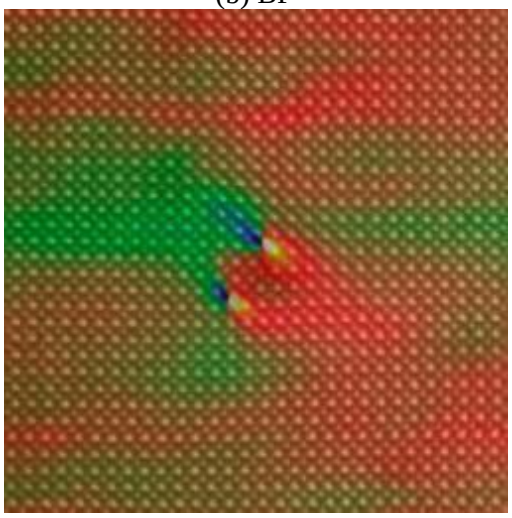

(d) ε_{yy}

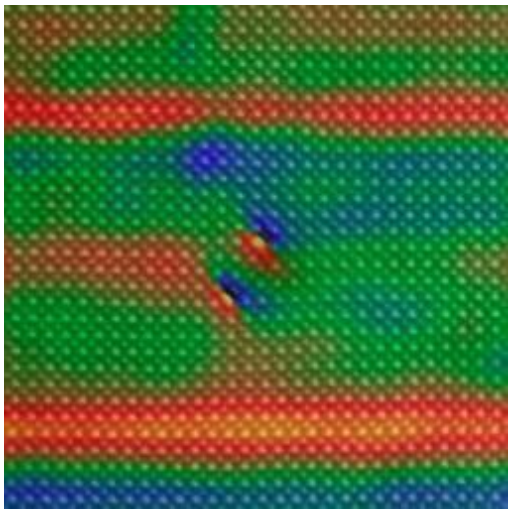

(e) τ_{xy}

Figure 6-18 Dislocation core in as-implanted regions in the specimens of 0.2 at.% Pr and 2 at.% Al. The strain field is calculated using a group of <110> reflections through the GPA package based on the HAADF image as shown in (a). (c) and (d) are the normal strain along the horizontal ε_{xx} and vertical directions ε_{yy}, respectively. In (e), τ_{xy} is the shear strain in the x-y plane. Scanning defects cause the banding artifacts observed in the computed strain fields.

In summary, the atomic arrangement of dislocation cores is complex and provides additional contrast to STEM-ABF/BF images probably due to their local strain fields. The detected atomic arrangement in the high-resolution images can be used to calculate the local strain field, which supports the different contrast mechanism of the STEM-ABF images compared to that contributed from the nano-clusters. Dislocations were detected mainly at the implant front and are only about a few nm in size. Their local strain fields affect only a few unit cells around the cores. Therefore, the effect of dislocations on the emission region, the implanted regions containing Pr ions, can be negligible.

CHAPTER SEVEN

CONCLUSIONS

In the present thesis, new experimental approaches to characterize low-dimensional defects within oxides were developed and successfully applied to the $SrTiO_3$ lattice with implanted foreign species or reconstructed surfaces.

According to the spatial distribution of probe electrons scattered by these low-dimensional defects, collecting signals with different positions of an annular detector highlight these defect features within oxides. Successful application of ABF images includes the direct imaging of Al-rich nano-clusters within a $SrTiO_3$ lattice.

A 'thickness' series method was developed for these energy-loss electrons. The reliable extraction of weak defect and surface signals was achieved by (linear least square) fitting methods applied to experimental datasets with various defect or surface signal contributions. By applying this method, we successfully solved the surface Ti configurations within a monolayer in reconstructed $SrTiO_3$ (001) crystal surfaces and the local defect configurations of implanted Pr within $SrTiO_3$ bulk crystals.

Conclusions are drawn for surface and bulk defects within $SrTiO_3$:

We provided an experimental spectroscopic signature of both the valence and crystal field of Ti ions located on the sub-surface and topmost layer. We reported HR profile images of the c(4x2) surface reconstructed (001) $SrTiO_3$ consisting of a distorted octahedral TiO_6 and pyramidal TiO_5 octahedra, which are generally consistent with atomic structures reported from DFT simulations[25]. In addition, HR profile images of the (2x1) surface reconstructed (001) $SrTiO_3$ surfaces were recorded, and thus provide experimental evidence along the normal direction for the proposed atomic structures[23].

Regarding bulk defects, we provided both experimental evidence, and simulation support of the local defect configurations of injected ions within $SrTiO_3$ lattices. Pr dopants occupy Sr-sites only, as demonstrated in the EELS map. The mechanism of luminescence enhancement from Al ions is different in our synthesis approach compared to the literature. The PL spectra suggest the symmetry breaking of the Pr-occupied lattice site is probably due to adjacent Al ions. The formation of Al-rich clusters was supported by HR ABF and HAADF images. The associated electronic structures of these nanostructures are mapped, suggesting the change of local interband transitions between Ti and O ions and the presence of defect levels within the band-gap.

The effects of implantation and subsequent heat-treatment as well as electron beam-induced effects were investigated. Under the current implantation conditions, a 20-30 nm depth (near) amorphous layer and a ~10 nm depth mosaic structure with a slight misorientation are present. The damaged layer is fully recrystallized at 800 ℃. Under the scanning electron beam, solid phase epitaxial recrystallization was observed in pre-amorphized $SrTO_3$ with large injected flux of heavy ions. Detailed structural characterization of different types of dislocations was carried out. The related strain fields were computed and found to roughly agree the simple dislocation model.

Future work includes theoretical study of the contrast mechanism of the ABF images and band structure calculations of the reconstructed surface as well as the Al-Pr rich clusters.

The bright contrast from these nano-clusters in the ABF images requires further simulation to confirm compositional fluctuation within them. On the other hand, the

bright contrast from the dislocations is highly corresponding to the strain fields around them, although, without perfect match with any of strain components or their combinations. More work is needed to clarify the spatial distribution of the scattered electrons from different compositions or strain fields, thus providing a solid foundation to explain the contrast of ABF images.

Experimentally, the atomic structure of the selected systems is solved based on the high-resolution imaging and spectral results. Therefore, in principle, the band structure can be calculated with input of their atomic structure into the first principle simulation codes such as Wien2k. The calculated electronic structure should be used to predict valence and core level excitations for comparison with experimental EELS data.

APPENDIX 1 PARAMETER ESTIMATION FOR INVERSE POWER-LAW BACKGROUND MODEL

Inverse power-law background model is the de-facto standard since it was proposed by Egerton[93] based on the physical description of plasmon peaks (the Drude model) and core-loss excitations (the hydrogenic cross section). Starting from equation 3-3, a natural log-log transformation to the base e is applied in order to treat it as a linear fitting problem.

$$\ln \mathbf{B} = \ln A - r \ln \mathbf{E} \text{ or}$$

$$\ln B_i = \ln A - r \ln E_i,\ y_i = \ln(B_i),\ \alpha = \ln(A),\ x_i = \ln(E_i) \qquad \text{A1-1}$$

where ***B*** is the recorded count vector within the background fitting windows ***E*** containing n energy intervals.

Especially for the least square fitting method, we rewrite A1-1 as A1-2 in order to have statistically independent parameters a and b [129,130].

$$\mathrm{Y} = a + b\,\mathrm{X}$$

$$y_i = \ln B_i;\ x_i' = x_i - \frac{\sum_n \sigma_i^{-2} x_i}{\sum_n \sigma_i^{-2}};\ a = \ln(A) - r\frac{\sum_n \sigma_i^{-2} x_i}{\sum_n \sigma_i^{-2}};\ b = -r \qquad \text{A1-2}$$

in which, σ_i is the uncertainty of the recorded count C_i. The above transformation actually shifts the fitting window in order to ensure the weighted y axis is located at the middle, as a result, the parameters *a* and *b* are only related to the values of y_i and x_i', respectively. This can be considered as additional proof of the statistical independence of the *a* and *b* parameters. It should be noted that the above transformation does not affect the output fitting results but only simplifies the variance estimation process.

A1.1 Hypotheses and Variance of Each Count

The following two hypotheses are well-accepted and based on the fundamental descriptions of basic physical processes.

A1.1.1 Hypothesis 1: Poissonian Distribution

Because the collection process of a spectrometer is essentially counting statistics of incoming, inelastic electrons, the probability density function (pdf) of recording C_i counts at each energy interval is given by Poisson statistics.

$$p(C_i) = \frac{\exp(-\bar{C}_i)(\bar{C}_i)^{C_i}}{(C_i)!} \quad (C_i \geq 0) \qquad \text{A1-3}$$

where $\overline{C_i}$ is 'true' but unknown value, also be called the parameter of the distribution.

A1.1.2 Hypothesis 2: Independence

We pre-assume that there is no dependence between the counts in different channels. Mathematically, this is equivalent to saying that the joint pdf of the counts between different energy channels $P(C_i*C_j)$ is the product of the pdf $P(C_i)$ and $P(C_j)$. Although it is difficult to justify, this hypothesis is plausible due to the following two reasons: (1) counts for different energies are recorded by different detectors in the case of parallel detection; (2) counts at different energy channels are recorded at different times in the case of sequential detection.

A1.1.3 Variance of Each Count

The noise of each observation C_i corresponding to the energy interval E_i generally includes two sources[131]: (a) major noise governed by Poisson statistics. (b) minor noise caused by additional processes in the conversion of these electrons to digital counts in the CCD/scintillator. (b) is usually negligible because of the application of the dark and gain reference of the detector and the effect from the dark current and readout counts and the inter-pixel mixing of signal expectations C_i can be removed. Thus, the variance of the observation C_i is

$$\mathrm{var}(C_i) = C_i \qquad \text{A1-4}$$

Due to the limitations of beam damage, a spectrum image or a group of spectra from the same region are usually obtained and then summed as the final spectrum. Under the reasonable assumption of ignorable shifts along the energy axis, the final observation C_i corresponding to the energy interval E_i is defined as

$$C_i = C_i^1 + C_i^2 + ... + C_i^k$$

The variance of C_i is given by propagation of uncertainties equation for independent random errors:

$$\mathrm{var}(C_i) = \sum_{j=1}^{k} C_i^j$$

A1.2 Least Square Fitting

under the assumption of no uncertainty in x_i' and y_i, least square fitting method is a standard approach to the best solution of an over-determined system, which has more equations than unknowns The best fitting solution has minimized sum of the squares of the "noise" within each dataset. In the present case, the goal is to minimize the sum of squared vertical distances between the observed responses in the dataset and the responses predicted by the linear approximation.

$$\sum_{i=1}^{N}\left[y_i - \left(a + bx_i'\right)\right]^2 = \min \qquad \text{A1-5}$$

Mathematically, it is equal to setting the partial derivates of A1-5 to zero.

$$\frac{\partial}{\partial a}\sum_{i=1}^{N}\left[y_i - \left(a + bx_i'\right)\right]^2\Big|_{a=\hat{a}} = 0 \;\&\; \frac{\partial}{\partial b}\sum_{i=1}^{N}\left[y_i - \left(a + bx_i'\right)\right]^2\Big|_{b=\hat{b}} = 0 \qquad \text{A1-6}$$

The final fitted parameters are:

$$\hat{a} = \frac{\left(\sum x_i'^2\right)\left(\sum y_i\right) - \left(\sum x_i'\right)\left(\sum x_i' y_i\right)}{N\left(\sum x_i'^2\right) - \left(\sum x_i'\right)^2}$$

$$\hat{b} = \frac{N\left(\sum x_i' y_i\right) - \left(\sum x_i'\right)\left(\sum y_i\right)}{N\left(\sum x_i'^2\right) - \left(\sum x_i'\right)^2} \qquad \text{A1-7}$$

According to Bessel equation, the variances of y_i, a and b are listed as:

$$\mathrm{var}(y_i) = \frac{1}{N-2}\sum_{i=1}^{N}\left[y_i - \left(\hat{a} + \hat{b}x_i'\right)\right]^2$$

$$\mathrm{var}(b) = \sum_{i=1}^{N}\left(\frac{\partial \hat{b}}{\partial y_i}\right)^2 \mathrm{var}(y_i) = \frac{N\,\mathrm{var}(y_i)}{N\left(\sum x_i'^2\right) - \left(\sum x_i'\right)^2}$$

$$\mathrm{var}(a) = \sum_{i=1}^{N}\left(\frac{\partial \hat{a}}{\partial y_i}\right)^2 \mathrm{var}(y_i) = \frac{\sum x_i'^2}{N\left(\sum x_i'^2\right) - \left(\sum x_i'\right)^2}\mathrm{var}(y_i) \qquad \text{A1-8}$$

Since the sum of x_i' is zero after transition stated in A1-2, a and b will be simplified to

$$\hat{a} = \frac{\left(\sum y_i\right)}{N} \;\&\; \hat{b} = \frac{N\left(\sum x_i' y_i\right) - \left(\sum y_i\right)}{N\left(\sum x_i'^2\right)}$$

$$\mathrm{var}(y_i) = \frac{1}{N-2}\sum_{i=1}^{N}\left[y_i - \left(\hat{a} + \hat{b}x_i'\right)\right]^2 \;\&\; \mathrm{var}(a) = \frac{\mathrm{var}(y_i)}{N} \;\&\; \mathrm{var}(b) = \frac{\mathrm{var}(y_i)}{\left(\sum x_i'^2\right)} \qquad \text{A1-9}$$

A1.3 Weighted Least Square Fitting

In practice, it is impossible to obtain experimental values without any uncertainties. If the uncertainty of x_i can be ignorable, weighted least square fitting methods provide more accurate fitting compared to the unweighted one. Defining σ_i as the uncertainty of y_i, then the goal becomes

$$\sum_{i=1}^{N}\frac{1}{\sigma_i^2}\left[y_i - (a + bx_i')\right]^2 = \min \qquad \text{A1-10}$$

The final fitted parameters are:

$$\hat{a} = \frac{1}{\Delta}\begin{vmatrix} \sum\frac{y_i}{\sigma_i^2} & \sum\frac{x_i'}{\sigma_i^2} \\ \sum\frac{x_i' y_i}{\sigma_i^2} & \sum\frac{x_i'^2}{\sigma_i^2} \end{vmatrix} = \frac{1}{\Delta}\left(\sum\frac{y_i}{\sigma_i^2}\sum\frac{x_i'^2}{\sigma_i^2} - \sum\frac{x_i'}{\sigma_i^2}\sum\frac{x_i' y_i}{\sigma_i^2}\right)$$

$$\hat{b}=\frac{1}{\Delta}\begin{vmatrix}\sum\frac{1}{\sigma_i^2} & \sum\frac{y_i}{\sigma_i^2}\\ \sum\frac{x_i'}{\sigma_i^2} & \sum\frac{x_i'y_i}{\sigma_i^2}\end{vmatrix}=\frac{1}{\Delta}(\sum\frac{1}{\sigma_i^2}\sum\frac{x_i'y_i}{\sigma_i^2}-\sum\frac{x_i'}{\sigma_i^2}\sum\frac{y_i}{\sigma_i^2})$$

$$\Delta=\begin{vmatrix}\sum\frac{1}{\sigma_i^2} & \sum\frac{x_i'}{\sigma_i^2}\\ \sum\frac{x_i'}{\sigma_i^2} & \sum\frac{x_i'^2}{\sigma_i^2}\end{vmatrix}=\sum\frac{1}{\sigma_i^2}\sum\frac{x_i'^2}{\sigma_i^2}-(\sum\frac{x_i'}{\sigma_i^2})^2 \qquad \text{A1-11}$$

The variances in the coefficients are

$$\mathrm{var}(y_i)=\frac{1}{N-2}\sum[\frac{1}{\sigma_i^2}(y_i-a-bx_i)^2]$$

$$\mathrm{var}(a)=\mathrm{var}(y_i)\cdot\frac{1}{\Delta}\sum\frac{x_i^2}{\sigma_i^2}\ \&\ \mathrm{var}(b)=\mathrm{var}(y_i)\cdot\frac{1}{\Delta}\sum\frac{1}{\sigma_i^2} \qquad \text{A1-12}$$

According to $\Sigma x_i'/\sigma_i^2=0$ and $\sigma_i^{-1}=\sqrt{y_i}$, the fitting parameters and their standard deviations are derived as following

$$\hat{a}=\frac{1}{\Delta}\begin{vmatrix}\sum y_i^2 & 0\\ \sum x_i'y_i^2 & \sum x_i'^2y_i\end{vmatrix}=\frac{1}{\Delta}\sum y_i^2\sum x_i'^2y_i$$

$$\hat{b}=\frac{1}{\Delta}\begin{vmatrix}\sum y_i & \sum y_i^2\\ 0 & \sum x_i'y_i^2\end{vmatrix}=\frac{1}{\Delta}\sum y_i\sum x_i'y_i^2$$

$$\Delta=\begin{vmatrix}\sum y_i & 0\\ 0 & \sum x_i'^2y_i\end{vmatrix}=\sum y_i\sum x_i'^2y_i$$

$$\mathrm{var}(y_i)=\frac{1}{N-2}\sum[y_i(y_i-a-bx_i')^2]$$

$$\mathrm{var}(a)=\mathrm{var}(y_i)\cdot\frac{1}{\Delta}\sum x_i'^2y_i\ \&\ \mathrm{var}(b)=\mathrm{var}(y_i)\cdot\frac{1}{\Delta}\sum y_i \qquad \text{A1-13}$$

A1.4 Maximum Likelihood

Maximum likelihood (ML) methods[132] provide unbiased and minimum mean square error estimates of all parameters. The best estimators from ML methods are the ones with maximized joint probability density function (pdf) of the counts obtained in different energy channels. Based on the independently Poisson distribution, the joint pdf is defined as

$$p(\mathbf{C} \mid c, r) = p(C_1, C_2, ..., C_n \mid A, r) = \prod_{i=1}^{n} \frac{\exp(-\bar{C}_i)}{C_i!} (\bar{C}_i)^{C_i} \qquad \text{A1-14}$$

To simplify the mathematics, the log-likelihood function is used as the optimization equation:

$$L(\mathbf{C} \mid c, r) = \ln\, p(\mathbf{C} \mid A, r) = \sum_{i=1}^{n} [C_i \ln \bar{C}_i - \bar{C}_i - \ln(C_i!)] \qquad \text{A1-15}$$

To maximum *L(C|c,r)* by setting the partial derivatives with respect to *c* and *r* to zero.

$$\frac{\partial L(\mathbf{C} \mid \alpha, r)}{\partial \alpha} = \sum_{i=1}^{n} [C_i - \exp(\alpha - r x_i)] = 0$$

$$\frac{\partial L(\mathbf{C} \mid \alpha, r)}{\partial r} = \sum_{i=1}^{n} -x_i [C_i - \exp(\alpha - r x_i)] = 0 \qquad \text{A1-16}$$

In order to remove the dependence on α, we define *f(r)* by taking the ratio of the partial sum in equation A1-16.

$$f(r) = \frac{m_1(r)}{m_0(r)} - x_w = 0 \qquad \text{A1-17}$$

with

$$x_w = \sum_{i=1}^{n} x_i C_i \Big/ \sum_{i=1}^{n} C_i, \; m_k(r) = \sum_{i=1}^{n} x_i^k \exp(-r x_i)$$

Since *f(r)* is a monotone decreasing function of *r* due to

$$f'(r) = \frac{\partial f}{\partial r} = \left(\frac{m_1(r)}{m_0(r)} \right)^2 - \frac{m_2(r)}{m_0(r)} < 0$$

The best estimator $\hat{r}$ can be infinitely approached using Newton's method staring with an initial guess r_0.

$$r_{n+1} = r_n - \frac{f(r_n)}{f'(r_n)} \qquad \text{A1-18}$$

Then,

$$\hat{\alpha} = \ln \frac{\sum_{i=1}^{n} C_i}{\sum_{i=1}^{n} \exp(-\hat{r} x_i)} \qquad \text{A1-20}$$

The variances and co-variance of the estimated background parameters are

$$S_\alpha^2 = \frac{m_{\lambda 2}}{\sum \bar{C}_i (x_i - m_{\lambda 1})^2} \quad \& \quad S_r^2 = \frac{1}{\sum \bar{C}_i (x_j - m_{\lambda 1})^2} \qquad \text{A1-21}$$

$$S_{\alpha,r} = \frac{m_{\lambda 1}}{\sum \bar{C}_i (x_j - m_{\lambda 1})^2}$$

in which,

$$m_{\lambda k} = \frac{\sum_{j=1}^{w} x_j^k \bar{C}_i}{\sum_{j=1}^{w} \bar{C}_i}, k = 1, 2$$

A1.5 Variances of the Signal

According to the inverse power-law background model, the variance of the background S_j within the signal window is defined as

$$\text{var}(B_j) = \left(\frac{\partial B}{\partial a}\right)^2 \text{var}(a) + \left(\frac{\partial B}{\partial b}\right)^2 \text{var}(b) \qquad \text{A1-22}$$

according to the equation for linear least square fitting, or

$$\text{var}(B_j) = \left(\frac{\partial B}{\partial \alpha}\right)^2 \text{var}(\alpha) + \left(\frac{\partial B}{\partial r}\right)^2 \text{var}(r) \qquad \text{A1-23}$$

based on the equation for maximum likelihood methods.

Thus, at each energy interval E_i within the signal window, the variance of signal will be

$$\mathrm{var}(S_j) = \left(\frac{\partial S_j}{\partial I_j}\right)^2 \mathrm{var}(I_j) + \left(\frac{\partial S_j}{\partial B_j}\right)^2 \mathrm{var}(B_j) = \mathrm{var}(I_j) + \mathrm{var}(B_j) \qquad \text{A1-24}$$

A1.6 Signal-to-noise Ratio

Signal-to-noise ratio is usually defined as

$$snr = \frac{\sum S_j}{\sqrt{\mathrm{var}(\sum S_j)}}$$

which is a universal criterion to evaluate the best fitting.

APPENDIX 2 *MATLAB* CODES

This appendix gives several *MATLAB* scripts involved in the present project. When *.dm3 files are used as the input, DM3Import.m by Robert A. McLeod is required in the working directory and can be downloaded from the following link (http://www.mathworks.com/matlabcentral/fileexchange/29351-dm3-import-for-gatan-digital-micrograph/content/DM3Import.m).

A2.1 Maximum Likelihood Background Fitting

```
function [A,r,snr,core] = MLfit(infile,varargin)

% MLfit evalutes the parameters A, r for the inverse power-law background model using the maximum likelihood estimation, in which the bound is specified by the Cramer-Rao inequality.
%
% Input:
% infile        the input data matrix, or input file name
% eprestart     the background fitting start energy: eV
% eprewidth     the backgound fitting window width: eV
% r             the intial guess of r, default: 2.
% min           the tolerance, default: 10^(-14)
%
% Output:
% A,r       parameters for the background power law model. B=AE^(-r)
% snr       signal-noise ratio, defined the ratio of the integral of signals and the integral of background within the signal window
% core      the sigal spectrum
% Example:
% infile = 'S1-T2-2 EELS SI (dark ref crt) aligned sum.dm3' ;
% eprestart = 454;
% eprewidth = 10;
% [A,r,snr] = MLfit(infile,eprestart,eprewidth);
%
% Ref: Unser et al, Optimal background estimation in EELS, J. Microsc.,
% 1987(145):245-256
```

```
% check the inputs
msg = nargchk(1,5,nargin);
if ~isempty(msg)
   fprintf('Error! Invalid Input!')
   return
end

if isnumeric(infile)
   [m,n] = size(infile);
   if m==2
      if n<2||n==2
         fprintf('Input Error! Please input the spectra data!')
      end
   elseif m>2
      if n==2
         infile =infile';
      else
         fprintf('Input Error! Please input the spectra data!')
      end
   else
      fprintf('Input Error! Please input the spectra data!')
   end
   escale = infile(1,:);
   spectrum = infile(2,:);
elseif isstr(infile)
   spectra_struct = DM3Import(infile);
   spectra =spectra_struct.spectra_data;  % unit:e-
   if size(spectra,2) > 1
      spectrum = spectra{1}.* spectra_struct.intensity.scale;
      edispersion = spectra_struct.xaxis{1}.scale;
      origin = spectra_struct.xaxis{1}.origin;
   else
      spectrum = spectra{1}.* spectra_struct.intensity.scale;
      edispersion = spectra_struct.xaxis.scale;
      origin = spectra_struct.xaxis.origin;
   end
   N = length( spectrum);
   escale = ( (0:N-1)-origin).* edispersion;   % unit:eV
else
   fprintf('Input Error!')
end

r = 2;
min = 10^(-14);
```

```
eprewidth = [];
eprestart = [];
plot(escale,spectrum);
axisx = escale;
spectrum_i = spectrum;

if (nargin == 3)
   if isnumeric(varargin{nargin-1})&&isnumeric(varargin{nargin-2})
      eprewidth = varargin{nargin-1};
      eprestart = varargin{nargin-2};
   else
      fprintf('Input Error!')
   end
elseif (nargin == 5)
   if isnumeric(varargin{nargin-1})&&isnumeric(varargin{nargin-2})&&isnumeric(varargin{nargin-3})&&isnumeric(varargin{nargin-4})
      min = varargin{nargin-1};
      r = varargin{nargin-2};
      eprewidth = varargin{nargin-3};
      eprestart = varargin{nargin-4};
   else
      fprintf('Input Error!')
   end
elseif (nargin==1)
   temp_input = input('Please input the start pointing for fitting (unit: eV, e.g. 454):', 's');
   eprestart = str2num(temp_input);
   temp_input = input('Please input the wide of fitting window (unit: eV, e.g. 10):', 's');
   eprewidth = str2num(temp_input);
else
   fprintf('Error! Invalid Input!');
end

if ~isempty(eprestart)&&~isempty(eprewidth)
   efilter = ((escale >= eprestart) & (escale <=(eprestart + eprewidth)));
   escale = nonzeros(escale(efilter))';
   spectrum = nonzeros(spectrum(efilter))';
end

% fitting processes
x = log(escale);
xw = sum(x.*spectrum)/sum(spectrum);
mr0 = sum(exp(-r.*x));
```

```
mr1 = sum(x.*exp(-r.*x));
fr = mr1/mr0-xw;

while abs(fr)>min
   mr2 = sum(x.*x.*exp(-r.*x));
   dfdr = (mr1/mr0)^2-mr2/mr0;
   r = r-fr/dfdr;
   mr0 = sum(exp(-r.*x));
   mr1 = sum(x.*exp(-r.*x));
   fr = mr1/mr0-xw;
end

A = sum(spectrum)/mr0;

back = A.*axisx.^(-r);
hold on; plot(axisx, back,'k');

x = log(axisx);
signalstart = 467;
signalwidth = 12;
efilter = ((axisx >= signalstart) & (axisx <=(signalstart + signalwidth)));

mlamda2 = sum(x(efilter).*x(efilter).*back(efilter))/sum(back(efilter));
mlamda1 = sum(x(efilter).*back(efilter))/sum(back(efilter));

b = sum(back(efilter));
dbdr = sum(-x(efilter).*back(efilter));
temp = back(efilter).*(x(efilter)-mlamda1).*(x(efilter)-mlamda1);
edeltab = (b*b*mlamda2+dbdr*dbdr+2*b*dbdr*mlamda1)/sum(temp);

t = sum(spectrum_i(efilter));
snr = (t-b)/sqrt(t+edeltab);
core = spectrum_i - back;
```

A2.2 Singular Value Decomposition

```
function image_svd(varargin)

% Image_svd applies singular value decomposition (SVD) on an image and
selects certain number of main components and then reconstructs to a noise-reduced
image.
% Input
%   *.dm3          the name of an image file to proceed
```

```
% check inputs
msg = nargchk(0,1,nargin);
if ~isempty(msg)
   fprintf('Error! Invalid Input!')
   return
end

if nargin == 0
   [fname, filepath] = uigetfile('D:\Matlab addins\PHD\*.dm3','Please choose the files');
   filename = strcat(filepath, fname);
elseif nargin ==1
   filename = varargin{nargin};
end

[dm3struct] = DM3Import( filename);
data = dm3struct.image_data;
clear dm3struct;

raw_image=imagesc(data);
colormap gray
axis equal off
figure(gcf)

% find the area to process
k = menu('zoomin and define left line coordinate','ok');
[Corner_x1,Corner_y1] = ginput(1);
Corner_x1=round(Corner_x1);
Corner_y1=round(Corner_y1);
k = menu('zoomin and define right line coordinate','ok');
[Corner_x2,Corner_y2] = ginput(1);
Corner_x2=round(Corner_x2);
Corner_y2=round(Corner_y2);
rectangle('Position',[Corner_x1, Corner_y1,Corner_x2-Corner_x1, Corner_y2-Corner_y1],'LineWidth',4,'Edgecolor','r');
data_reduce = data(Corner_y1:Corner_y2, Corner_x1:Corner_x2);

raw_image=imagesc(data_reduce);
colormap gray
axis equal off

[u, s, v]=svd(data_reduce);
xweight = diag(s);
```

```
figure;
bar(xweight);

answer =inputdlg({'the starting components for display?','the end components for display?'});
if ~isempty(answer{1})
   displaynumberstart = round(str2num(answer{1}));
end
if ~isempty(answer{2})
   displaynumberend = round(str2num(answer{2}));
end
for i=displaynumberstart:1:displaynumberend
    figure;
    recon = u(:,i)*s(i,i)*v(:,i)';
    raw_image=imagesc(recon);
    colormap gray
    axis equal off
    titlename = strcat('Component', num2str(i));
    title(titlename);
end

answer =inputdlg({'How many components for reconstruction?'});
if ~isempty(answer{1})
   reconnumber = round(str2num(answer{1}));
end

reconf = u(:,1:reconnumber)*s(1:reconnumber,1:reconnumber)*v(:,1:reconnumber)';
figure;
raw_image=imagesc(reconf);
colormap gray
axis equal off
```

A2.3 Dimension Calibration for a Scanned Diffraction Film

```
function cali = tifcalibration(varargin)

% TIFCALIBRATION calibrates the *.tif file from scanning films containing diffractions.
%
% Input
%  filename     the name of files
%  L            Camera length, (cm)
```

```
%
% Output
%  cali          the calibration value used in Digital Micrograph, image-->display-->calibration-->k,1,1/nm (unit)

msg = nargchk(0,2,nargin);
if ~isempty(msg)
   fprintf('Error! Invalid Input!')
   return
end

if (nargin == 1)
   if isnumeric(varargin{nargin})
      L = varargin{nargin};
      [fname, filepath] = uigetfile('E:\Experimental\*.tif','Please choose the files'); % dialog, to select data file1,sets as the tensile files
      filename = strcat(filepath, fname);
   end
elseif (nargin == 2)
   if isnumeric(varargin{nargin}c)
      L = varargin{nargin};
      filename = varargin{nargin-1};
   elseif isstr(varargin{nargin})
      filename = varargin{nargin};
      L = varargin{nargin-1};
   end
else
   fprintf('Invalid INPUT! Only the camera length or file name + camera length!')
end

imgt = imread(filename);
imgf = imfinfo(filename);
xr = imgf.XResolution;
yr = imgf.YResolution;
ru = imgf.ResolutionUnit;

if ru=='Inch'
   unitexchange = 2.54; %inch/cm
elseif ru=='cm'
   unitexchange = 1;
elseif ru == 'mm'
   unitexchange = 0.1;  %cm/mm
end
```

```
U = 120; % keV
c = 2.99792458e8; % m/s.
h = 6.6260755e-34; % J*s. 4.1356692e-15; %eV*s.
m0 = 9.1093897e-31; % kg.
U = U*1e3; % V.
e = 1.60217733e-19; % C.
lambda = h/sqrt(2*m0*e*U*(1+e*U/2/m0/c^2));

cali = 1/(lambda*L*10^9*(xr/unitexchange/10)); % 1/nm
%   1/(m*mm*(m-->nm)*(cm-->mm))
```

APPENDIX 3 THE VISIBILITY OF PR WIHIN THE $SrTiO_3$ LATTICE

Here we include multislice calculations of larger clusters or detection of the single atoms profiles supporting the conclusion about clusters and thickness. Under the conditions that a single Pr ion occupies a Sr-lattice site or a Ti-lattice site, the contrast from a single Pr atom is negligible in the HAADF images. (see section 4.1.1 and figure A3-1(a)) When forming a cluster, Pr ions are observed as bright dots in the simulated HAADF images. (Figure A3-1(b))

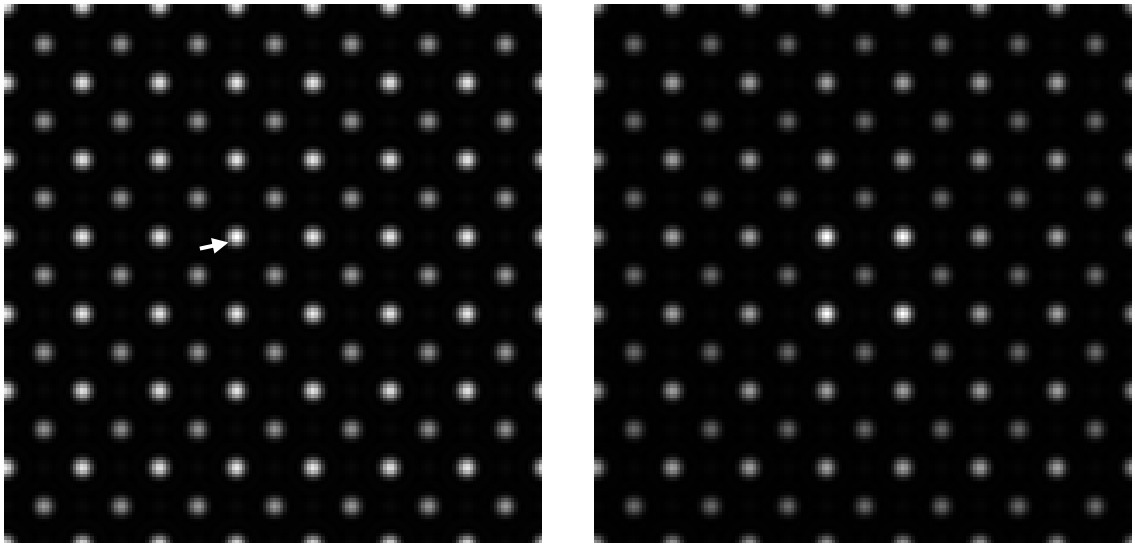

(a) single Pr (b) Pr_8

Figure A3-1 The detectability of Pr clusters. In (a), a single Pr atoms replace a Sr positions as index in the white arrow. In (b), eight Pr atoms substitute adjacent Sr-sites, in which four neighboring atomic columns containing two adjacent Pr atoms each. Pr atoms are at the atomic columns shown as bright dots in (b).

APPENDIX 4 SIMULATED LOW-LOSS EEL SPECTRA IN $SrTiO_3$

Based on the dielectric constant spectra of bulk $SrTiO_3$, the low-loss EEL spectra and their spatial distributions can be simulated as suggested in the reference[126]. According to the first principle simulations in the literature[128], intra-band transitions occur within the energy window of 0-29 eV. The dominant feature around 29 eV corresponds to the plasmon-like collective excitation of the valence and semicore electrons. The intra-band transitions are independent of the momentum vector k_y, while the plasmon-like feature has a slight dependence on the momentum vector k_y. These features are clearly indicated in the simulated E-k_y loss images in figure A4-2 under 30 kV incident electron beam.

The Cerenkov radiation losses with very sharp forward distribution arise when the electron velocity exceeds the phase speed of light in a transparent medium. Cerenkov losses are negligible with a 30 eV incident beam, resulting in features independent of the momentum vector k_y within the energy-loss window of 0-4 eV as shown in figure A4-2. More importantly, under high incident electron beam, the Cerenkov losses contribute as a flat background, as shown in figure A4-1.

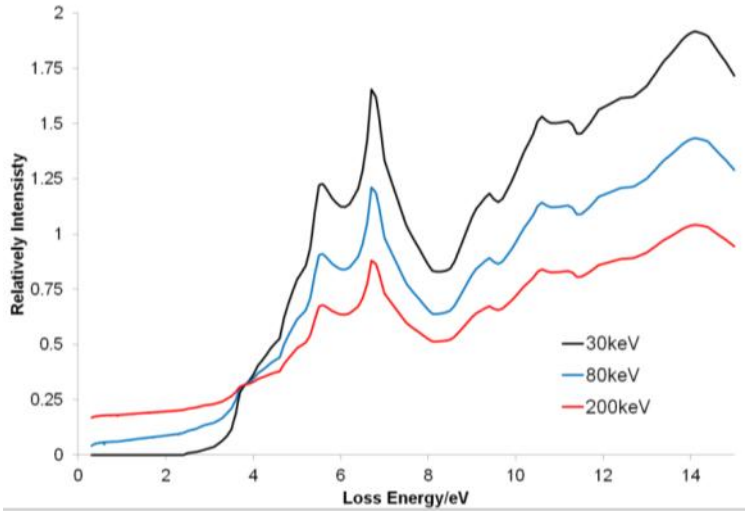

Figure A4-1 The simulated EEL spectra at different incident energies

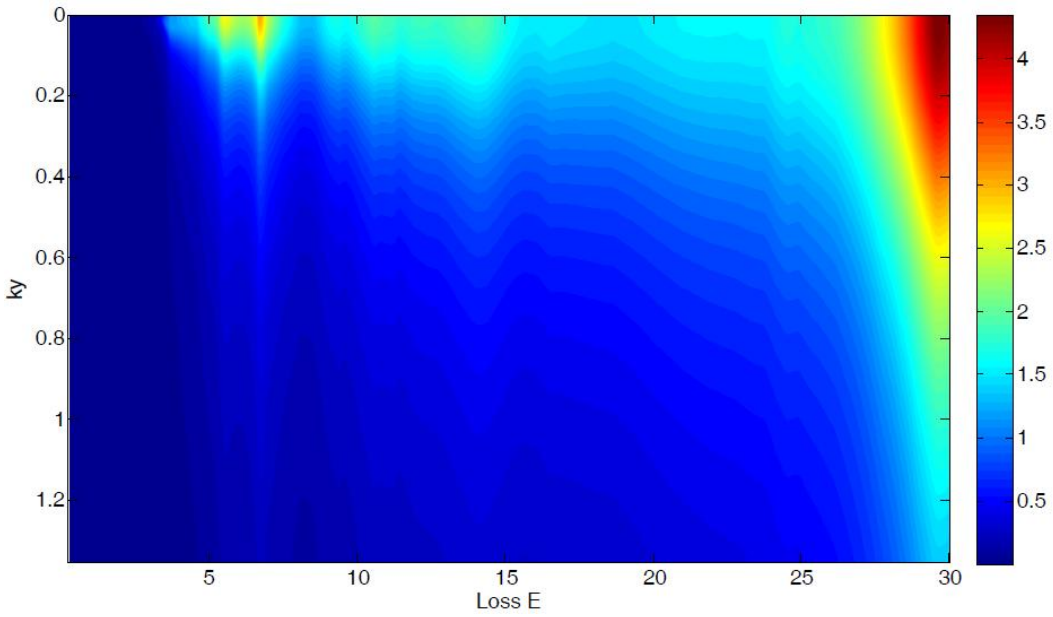

Figure A4-2 Simulated E-k_y loss images at 30 eV.

APPENDIX 5 STRAIN FIELD AROUND A DISLOCATION WITHIN AN ISOTROPIC MATRIX

The strain field around a simple dislocation within an isotropic matrix is shown in figure A5-1 according to A5-2 and A5-2.

According to the elasticity theory, the strain field around a screw dislocation within an isotropic matrix, except the dislocation core is given by:

$$\sigma_{xx} = \sigma_{yy} = \sigma_{zz} = 0,\ \tau_{xy} = 0$$

$$\tau_{xz} = -\frac{\tau_0 by}{x^2 + y^2}, \tau_{yz} = \frac{\tau_0 bx}{x^2 + y^2}, \tau_0 = \frac{G}{2\pi} \qquad \text{A5-1}$$

and the strain field around an edge dislocation wthin an isotropic matrix, except the dislocation core, can be described as:

$$\sigma_{xx} = -\frac{\tau_0 by(3x^2 + y^2)}{(x^2 + y^2)^2},\ \sigma_{yy} = -\frac{\tau_0 by(x^2 - y^2)}{(x^2 + y^2)^2}, \sigma_{zz} = 2\nu\frac{\tau_0 by}{x^2 + y^2}$$

$$\tau_{xy} = \frac{\tau_0 bx(x^2 - y^2)}{(x^2 + y^2)^2},\ \tau_{xz} = \tau_{yz} = 0,\ \tau_0 = \frac{G}{2\pi(1-\nu)} \qquad \text{A5-2}$$

where, σ_{xx}, σ_{yy} and σ_{zz} are the normal stress along x, y and z directions, repectively; τ_{xx}, τ_{yy}, τ_{zz} are the shear stress along different directions; b is the Burger vector defined for the dislocations; G is the shear modulus, and v is the Poisson ratio of the materials. In conclusion, in an isotropic matrix, there are only normal stresses and shear stresses lying in the plane perpendicular to the dislocation line for ideal edge dislocations. As for screw dislocations, shear stresses are along their Burger vectors.

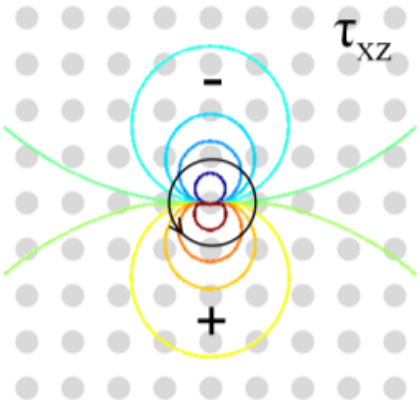

(a) screw dislocation, shear stress τ_{xz}

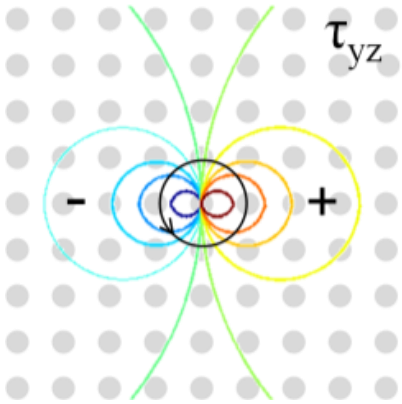

(b) screw dislocation, shear stress τ_{yz}

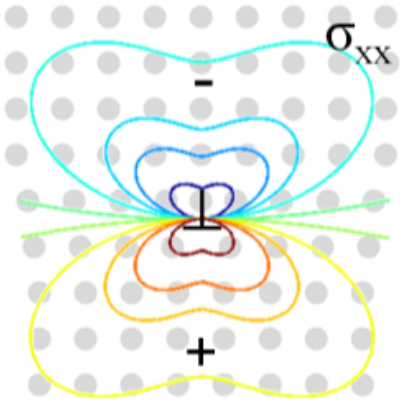

(c) edge dislocation, normal stress σ_{xx}

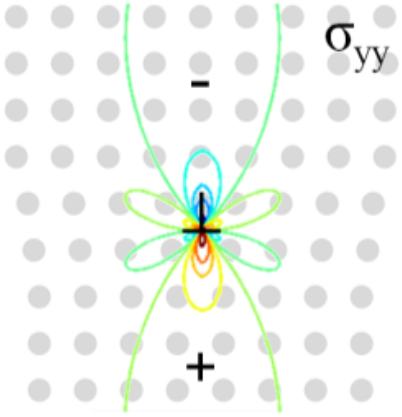

(d) edge dislocation, normal stress σ_{yy}

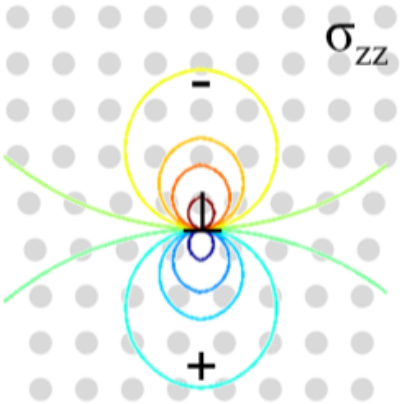

(e) edge dislocation, normal stress σ_{zz}

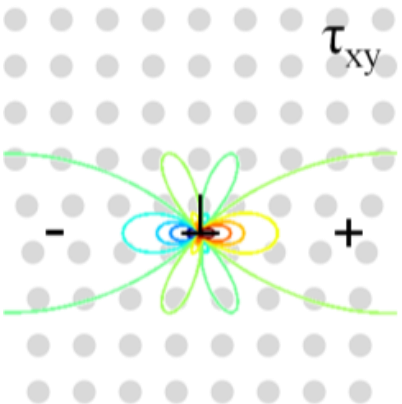

(f) edge dislocation, shear stress τ_{xy}

Figure A5-1 stress field around dislocations computed from equation A5-1 and A5-2. (a) and (b) are the shear stress of a screw dislocation with burger vector and dislocation line along the normal direction.(c)-(f) are the stress fields around a edge dislocation with burger vector along the horizontal direction and the dislocation line along the normal direction.

REFERENCE:

1 Scott, J. F. Technical feature - Physics of oxides for future devices. *Mrs Bull*, 227-230 (2010).

2 Mannhart, J. & Schlom, D. G. Oxide interfaces-An opportunity for electronics. *Science* **327**, 1607-1611 (2010).

3 Jiang, Q. D. & Zegenhagen, J. $SrTiO_3$(001) surfaces and growth of ultra-thin $GdBa_2Cu_3O_{7-x}$ films studied by LEED/AES and UHV-STM. *Surf Sci* **338**, L882-L888 (1995).

4 Iddir, H., Komanicky, V., Ogut, S., You, H. & Zapol, P. Shape of platinum nanoparticles supported on $SrTiO_3$: Experiment and theory. *J Phys Chem C* **111**, 14782-14789 (2007).

5 Ueno, K. *et al.* Electric-field-induced superconductivity in an insulator. *Nat Mater* **7**, 855-858 (2008).

6 Ohtomo, A. & Hwang, H. Y. A high-mobility electron gas at the $LaAlO_3/SrTiO_3$ heterointerface. *Nature* **427**, 423-426 (2004).

7 Son, J. *et al.* Epitaxial $SrTiO_3$ films with electron mobilities exceeding 30,000 $cm^2V^{-1}s^{-1}$. *Nat Mater* **9**, 482-484 (2010).

8 Kan, D. S. *et al.* Blue-light emission at room temperature from Ar^+-irradiated $SrTiO_3$. *Nat Mater* **4**, 816-819 (2005).

9 Muller, D. A. Structure and bonding at the atomic scale by scanning transmission electron microscopy. *Nat Mater* **8**, 263-270 (2009).

10 Voyles, P. M., Muller, D. A., Grazul, J. L., Citrin, P. H. & Gossmann, H. J. L. Atomic-scale imaging of individual dopant atoms and clusters in highly n-type bulk Si. *Nature* **416**, 826-829 (2002).

11 Batson, P. E., Dellby, N. & Krivanek, O. L. Sub-angstrom resolution using aberration corrected electron optics. *Nature* **418**, 617-620 (2002).

12 Freitag, B., Kujawa, S., Mul, P. M., Ringnalda, J. & Tiemeijer, P. C. Breaking the spherical and chromatic aberration barrier in transmission electron microscopy. *Ultramicroscopy* **102**, 209-214 (2005).

13 Heber, J. Materials science: Enter the oxides. *Nature* **459**, 28-30 (2009).

14 Vonhelmolt, R., Wecker, J., Holzapfel, B., Schultz, L. & Samwer, K. Giant negative magnetoresistance in perovskite-like $La_{2/3}Ba_{1/3}MnO_x$ ferromagnetic-films. *Phys Rev Lett* **71**, 2331-2333 (1993).

15 Yennie, D. R. Integral quantum Hall effect for nonspecialists. *Rev Mod Phys* **59**, 781 (1987).

16 Ramesh, R. & Spaldin, N. A. Multiferroics: progress and prospects in thin films. *Nat Mater* **6**, 21-29 (2007).

17 Buban, J. P. *et al.* Grain boundary strengthening in alumina by rare earth impurities. *Science* **311**, 212-215 (2006).

18 Wang, S. W. *et al.* Dopants adsorbed as single atoms prevent degradation of catalysts. *Nat Mater* **3**, 143-146 (2004).

19 Domen, K., Kudo, A. & Onishi, T. Mechanism of photocatalytic decomposition of water into H_2 and O_2 over NiO-$SrTiO_3$. *J Catal* **102**, 92-98 (1986).
20 Tanaka, H., Matsumoto, T., Kawai, T. & Kawai, S. Surface-structure and electronic property of reduced $SrTiO_3$(100) surface observed by scanning tunneling microscopy spectroscopy. *Jpn J Appl Phys 1* **32**, 1405-1409 (1993).
21 Inada, H. *et al.* Atomic imaging using secondary electrons in a scanning transmission electron microscope: Experimental observations and possible mechanisms. *Ultramicroscopy* **111**, 865-876 (2011).
22 Erdman, N. & Marks, L. D. $SrTiO_3$(001) surface structures under oxidizing conditions. *Surf Sci* **526**, 107-114 (2003).
23 Erdman, N. *et al.* The structure and chemistry of the TiO_2-rich surface of $SrTiO_3$(001). *Nature* **419**, 55-58 (2002).
24 Jiang, Q. D. & Zegenhagen, J. c(6x2)and c(4x2)reconstruction of $SrTiO_3$(001). *Surf Sci* **425**, 343-354 (1999).
25 Erdman, N. *et al.* Surface structures of $SrTiO_3$ (001): A TiO_2-rich reconstruction with a c(4 x 2) unit cell. *J Am Chem Soc* **125**, 10050-10056 (2003).
26 Lanier, C. H. *et al.* Atomic-scale structure of the $SrTiO_3$(001)-c(6x2) reconstruction: Experiments and first-principles calculations. *Phys Rev B* **76**, - (2007).
27 Cord, B. & Courths, R. Electronic study of $SrTiO_3$(001) surfaces by photoemission. *Surf Sci* **162**, 34-38 (1985).
28 Fang, Z. & Terakura, K. Spin and orbital polarizations around oxygen vacancies on the (001) surfaces of SrTiO3. *Surf. Sci.* **470**, L75-L80 (2000).
29 Seo, D. K., Perdue, K., Ren, J. & Whangbo, M. H. Study of scanning tunneling microscopy images and probable relaxations of the SrTiO3(100) surface by electronic structure calculations. *Surf Sci* **370**, 245-251 (1997).
30 Kubo, T. & Nozoye, H. Surface structure of $SrTiO_3$(100)-(root 5 x root 5)-R26.6 degrees. *Phys Rev Lett* **86**, 1801-1804 (2001).
31 Subramanian, A. & Marks, L. D. Surface crystallography via electron microscopy. *Ultramicroscopy* **98**, 151-157 (2004).
32 Shibata, N. *et al.* Direct imaging of reconstructed atoms on TiO_2 (110) surfaces. *Science* **322**, 570-573 (2008).
33 Marks, L. D. Direct imaging of carbon-covered and clean gold (110) surfaces. *Phys Rev Lett* **51**, 1000 (1983).
34 Weber, M. J. & Schaufele, R. F. Vibronic spectrum of Eu^{3+} in strontium titanate. *Phys Rev* **138**, A1544 (1965).
35 Yamamoto, H., Makishima, S. & Shionoya, S. Vibronic structure in luminescence spectra of rare earth ions in $SrTiO_3$, $BaTiO_3$ and other perovskites. *Journal of the Physical Society of Japan* **23**, 1321-1332 (1967).
36 Vecht, A. *et al.* New electron excited light emitting materials, 781-784 (AVS).
37 Toki, H., Sato, Y., Tamura, K., Kataoka, F. & Itoh, S. *Proc. Third Int. Display Workshops 2* (1996).

38 Yamamoto, H., Okamoto, S. & Kabayashi, H. Luminescence of rare-earth ions in perovskite-type oxides: from basic research to applications. *J Lumin* **100**, 325-332 (2002).

39 Shin, S. H., Jeon, D. Y. & Suh, K. S. Role of Ga^{3+} in $SrTiO_3$: Pr,Ga phosphor studied through its aging behavior under low-dose electron irradiation. *Jpn J Appl Phys 1* **40**, 6876-6877 (2001).

40 Ryu, H., Singh, B. K., Bartwal, K. S., Brik, M. G. & Kityk, I. V. Novel efficient phosphors on the base of Mg and Zn co-doped $SrTiO_3$: Pr^{3+}. *Acta Mater* **56**, 358-363 (2008).

41 Kyomen, T., Sakamoto, R., Sakamoto, N., Kunugi, S. & Itoh, M. Photoluminescence properties of Pr-doped (Ca,Sr,Ba)TiO_3. *Chem Mater* **17**, 3200-3204 (2005).

42 Tian, L. & Mho, S.-i. Enhanced luminescence of $SrTiO_3$:Pr^{3+} by incorporation of Li^+ ion. *Solid State Commun* **125**, 647-651 (2003).

43 Okamoto, S., Kobayashi, H. & Yamanoto, H. Effects of Al addition on photoluminescence properties in rare-earth ion-doped $SrTiO_3$. *J Electrochem Soc* **147**, 2389-2393 (2000).

44 Okamoto, S. & Kobayashi, H. Enhancement of characteristic red emission from $SrTiO_3$:Pr^{3+} by Al addition. *J Appl Phys* **86**, 5594-5597 (1999).

45 Deguchi, M. *et al.* Luminescence mechanism of (Pr, Al)-doped $SrTiO_3$ fine particles investigated by x-ray absorption spectroscopy. *Phys Rev B* **78**, 073103 (2008).

46 Mochizuki, S. & et al. Photoluminescence and reversible photo-induced spectral change of $SrTiO_3$. *J Phys: Condens Mat* **17**, 923 (2005).

47 Kenyon, A. J. Recent developments in rare-earth doped materials for optoelectronics. *Prog Quant Electron* **26**, 225-284 (2002).

48 De Mello Donegá, C., Meijerink, A. & Blasse, G. Non-radiative relaxation processes of the Pr^{3+} ion in solids. *J Phys Chem Solids* **56**, 673-685 (1995).

49 Boutinaud, P., Pinel, E., Dubois, M., Vink, A. P. & Mahiou, R. UV-to-red relaxation pathways in $CaTiO_3$:Pr^{3+}. *J Lumin* **111**, 69-80 (2005).

50 Reut, E. G. & Ryskin, A. I. Virtual recharge: Mechanism of radiationless transition in scheelite and fergusonite type crystals doped with rare-earth ions. *phys status solidi (a)* **17**, 47-57 (1973).

51 Boutinaud, P. *et al.* Making red emitting phosphors with Pr^{3+}. *Opt Mater* **28**, 9-13 (2006).

52 Boutinaud, P., Mahiou, R., Cavalli, E. & Bettinelli, M. Red luminescence induced by intervalence charge transfer in Pr^{3+}-doped compounds. *J Lumin* **122-123**, 430-433 (2007).

53 Fujiwara, R., Sano, H., Shimizu, M. & Kuwabara, M. Quantitative analysis of UV excitation bands for red emissions in Pr^{3+}-doped $CaTiO_3$, $SrTiO_3$ and $BaTiO_3$ phosphors by peak fitting. *J Lumin* **129**, 231-237 (2009).

54 Okamoto, S., Tanaka, S. & Yamamoto, H. Reduction process of Ruddlesden-Popper-Type planar faults in $SrTiO_3$:Pr^{3+} by Al addition. *Electrochem Solid St* **3**, 242-244 (2000).

55 Okamoto, S. & Yamamoto, H. Luminescent properties of praseodymium-doped alkaline-earth titanates. *J Lumin* **102-103**, 586-589 (2003).

56 Yamamoto, H. & Okamoto, S. Efficiency enhancement by aluminum addition to some oxide phosphors for field emission displays. *Displays* **21**, 93-98 (2000).

57 Okamoto, S. & Yamamoto, H. Characteristic enhancement of emission from $SrTiO_3:Pr^{3+}$ by addition of group-IIIb ions. *Appl Phys Lett* **78**, 655-657 (2001).

58 Diallo, P. T., Jeanlouis, K., Boutinaud, P., Mahiou, R. & Cousseins, J. C. Improvement of the optical performances of Pr^{3+} in $CaTiO_3$. *J Alloy Compd* **323-324**, 218-222 (2001).

59 Tang, J., Yu, X., Yang, L., Zhou, C. & Peng, X. Preparation and Al^{3+} enhanced photoluminescence properties of $CaTiO_3:Pr^{3+}$. *Mater Lett* **60**, 326-329 (2006).

60 Honma, T. & Yamamoto, H. Site determination of doped Ga ions in $SrTiO_3:Pr^{3+}$ phosphor for field emission displays by XAFS. *X-RAY ABSORPTION FINE STRUCTURE - XAFS13: 13th International Conference. AIP Conference Proceedings* **882**, 469-471 (2007).

61 Ogasawara, K. *et al.* Optical spectra of trivalent lanthanides in $LiYF_4$ crystal. *J Solid State Chem* **178**, 412-418 (2005).

62 Takeda, T. & Watanabe, A. Electron spin resonances in reduced $BaTiO_3$. *J. Phys. Soc. Jpn* **21**, 267-274 (1966).

63 Aiura, Y. *et al.* Photoemission study of the metallic state of lightly electron-doped $SrTiO_3$. *Surf Sci* **515**, 61-74 (2002).

64 Kan, D. *et al.* Blue luminescence from electron-doped $SrTiO_3$. *Appl. Phys. Lett.* **88** (2006).

65 Grabner, L. Photoluminescence in $SrTiO_3$. *Physical Review* **177**, 1315 (1969).

66 Kutty, T. R. N. & Nag, A. Role of interface states associated with transitional nanophase precipitates in the photoluminescence enhancement of $SrTiO_3$: Pr^{3+},Al^{3+}. *J Mater Chem* **13**, 2271-2278 (2003).

67 White, C. W. *et al.* Ion-implantation and annealing of crystalline oxides and ceramic materials. *Nucl Instrum Meth B* **32**, 11-22 (1988).

68 White, C. W., Mchargue, C. J., Sklad, P. S., Boatner, L. A. & Farlow, G. C. Ion-implantation and annealing of crystalline oxides. *Mater Sci Eng: C* **4**, 41-146 (1989).

69 Sun, K., Zhu, S., Fromknecht, R., Linker, G. & Wang, L. M. Formation of single-layered Au nanoparticles in Au ion implanted TiO_2 and $SrTiO_3$. *Mater Lett* **58**, 547-550 (2004).

70 Liu, C. M., Zu, X. T. & Zhou, W. L. Photoluminescence of nitrogen doped $SrTiO_3$. *J Phys D: Appl Phy* **40**, 7318 (2007).

71 Yang, B., Townsend, P. D. & Fromknecht, R. Radioluminescence detection of bulk effects in $SrTiO_3$ induced by surface ion implantation. *Nucl Instrum Meth B* **217**, 60-64 (2004).

72 Wang, C. M. *et al.* Precipitation of Au nanoclusters in $SrTiO_3$ by ion implantation. *J Appl Phys* **95**, 5060-5068 (2004).

73 Wang, C. M., Shutthanandan, V., Zhang, Y., Thevuthasan, S. & Duscher, G. Direct observation of substitutional Au atoms in $SrTiO_3$. *Phys Rev B* **70**, - (2004).

74 Oyoshi, K., Hishita, S. & Haneda, H. Study of ion beam induced expitaxial crystalization of $SrTiO_3$. *J Appl Phys* **87**, 3450-3456 (2000).
75 Nakao, S., Wang, Z., Jin, P., Miyagawa, Y. & Miyagawa, S. Effect of high-energy Si^+ ion irradiation on the crystallization behavior of amorphous strontium titanate films. *Nucl Instrum Meth B* **191** (2002).
76 Soulet, S., Chaumont, J., Sabathier, C. & Krupa, J.-C. Irradiation-disorder creation in $SrTiO_3$. *J Mater Res* **17**, 9-13 (2002).
77 Meldrum, A., Boatner, L. A., Weber, W. J. & Ewing, R. C. Amorphization and recrystallization of the ABO_3 oxides. *J Nucl Mater* **300**, 242-254 (2002).
78 Zhang, Y. *et al.* Ion-induced damage accumulation and electron-beam-enhanced recrystallization in $SrTiO_3$. *Phys Rev B* **72**, 094112 (2005).
79 Sabathier, C., Chaumont, J. & Krupa, J. C. Dose rate and temperature effects in radiation disorder creation in $SrTiO_3$. *Nucl Instrum Meth B* **196**, 308-314 (2002).
80 Albrecht, J. *et al.* Surface patterning of $SrTiO_3$ by 30 keV ion irradiation. *Surf Sci* **547**, L847-L852 (2003).
81 Lee, J. S. *et al.* Effects of Co Implantation in $BaTiO_3$, $SrTiO_3$ and $KTaO_3$. *Electrochem Solid St* **6**, J1-J3 (2003).
82 Lee, J. S. *et al.* Magnetic properties of Co- and Mn-implanted $BaTiO_3$, $SrTiO_3$ and $KTaO_3$. *Solid State Electron* **47**, 2225-2230 (2003).
83 Takeda, Y., Plaksin, O. A., Lu, J., Kono, K. & Kishimoto, N. Optical nonlinearity of Cu:$SrTiO_3$ composite fabricated by negative ion implantation. *Nucl Instrum Meth B* **250**, 372-376 (2006).
84 Moretti, P., Canut, B., Ramos, S. M. M., Thevenard, P. & Godefroy, G. Niobium implantation effects in $BaTiO_3$ and $SrTiO_3$. *Nucl Instrum Meth B* **65**, 264-269 (1992).
85 Rankin, J., McCallum, J. C. & Boatner, L. A. The effect of annealing environments on the epitaixal recrystallization of ion-beam-amorphized $SrTiO_3$. *J Mater Res* **7**, 717-724 (1991).
86 Zhang, Y. *et al.* Response of strontium titanate to ion and electron irradiation. *J Nucl Mater* **389**, 303-310 (2009).
87 Jencic, I., Bench, M. W., Robertson, I. M. & Kirk, M. A. Electron-beam-induced crystallization of isolated amorphous regions in Si, Ge, GaP, and GaAs. *J Appl Phys* **78**, 974-982 (1995).
88 Bae, I.-T., Zhang, Y., Weber, W. J., Higuchi, M. & Giannuzzi, L. A. Electron-beam induced recrystallization in amorphous apatite. *Appl Phys Lett* **90**, 021912 (2007).
89 Muller, E. W. Study of atomic structure of metal surfaces in the field ion microscope. *J Appl Phys* **28**, 1-6 (1957).
90 Binnig, G., Quate, C. F. & Gerber, C. Atomic force microscope. *Phys Rev Lett* **56**, 930 (1986).
91 Eigler, D. M. & Schweizer, E. K. Positioning single atoms with a scanning tunnelling microscope. *Nature* **344**, 524-526 (1990).
92 Sugimoto, Y. *et al.* Chemical identification of individual surface atoms by atomic force microscopy. *Nature* **446**, 64-67 (2007).

93 Egerton, R. F. *Electron Energy-Loss Spectroscopy in the Electron Microscope*. 2nd edn, (Springer New York Dordrecht Heidelberg London, 2011).
94 Egerton, R. F. Electron energy-loss spectroscopy in the TEM. *Rep Prog Phys* **72**, 016502 (2009).
95 Voyles, P. M., Grazul, J. L. & Muller, D. A. Imaging individual atoms inside crystals with ADF-STEM. *Ultramicroscopy* **96**, 251-273 (2003).
96 Crewe, A. V., Wall, J. & Langmore, J. Visibility of single atoms. *Science* **168**, 1338-1340 (1970).
97 Nellist, P. D. & Pennycook, S. J. Direct imaging of the atomic configuration of ultradispersed catalysts. *Science* **274**, 413-415 (1996).
98 Ho, O. S. *et al.* Point defect configurations of supersaturated Au atoms inside Si nanowires. *Nano Lett* **8**, 1016-1019 (2008).
99 Muller, D. A., Nakagawa, N., Ohtomo, A., Grazul, J. L. & Hwang, H. Y. Atomic-scale imaging of nanoengineered oxygen vacancy profiles in $SrTiO_3$. *Nature* **430**, 657-661 (2004).
100 Meyer, R. R. *et al.* Discrete atom imaging of one-dimensional crystals formed within single-walled carbon nanotubes. *Science* **289**, 1324-1326 (2000).
101 Jia, C. L., Lentzen, M. & Urban, K. Atomic-resolution imaging of oxygen in perovskite ceramics. *Science* **299**, 870-873 (2003).
102 Jia, C. L., Thust, A. & Urban, K. Atomic-scale analysis of the oxygen configuration at a $SrTiO_3$ dislocation core. *Phys Rev Lett* **95**, - (2005).
103 Suenaga, K. *et al.* Element-Selective Single Atom Imaging. *Science* **290**, 2280-2282 (2000).
104 Allen, L. J., Findlay, S. D., Lupini, A. R., Oxley, M. P. & Pennycook, S. J. Atomic-resolution electron energy loss spectroscopy imaging in aberration corrected scanning transmission electron microscopy. *Phys Rev Lett* **91**, - (2003).
105 Varela, M. *et al.* Spectroscopic imaging of single atoms within a bulk solid. *Phys Rev Lett* **92**, 095502-095501-095504 (2004).
106 Choi, S. Y., Chung, S. Y., Yamamoto, T. & Ikuhara, Y. Direct determination of dopant site selectivity in ordered perovskite $CaCu_3Ti_4O_{12}$ polycrystals by aberration-corrected STEM. *Adv Mater* **21**, 885-+ (2009).
107 Radtke, G. & Botton, G. A. in *Scanning Transmission Electron Microscopy* (eds Stephen J. Pennycook & Peter. D. Nellist) (Springer, 2011).
108 Cowley, J. M. & Moodie, A. F. The scattering of electrons by atoms and crystals. I. A new theoretical approach. *Acta Crystallographica* **10**, 609-619 (1957).
109 Kirkland, E. J. *Advanced Computing in Electron Microscopy*. illustrated edn, 289 (Springer, 2010).
110 Frank de, G. Multiplet effects in X-ray spectroscopy. *Coordination Chemistry Reviews* **249**, 31-63 (2005).
111 Stavitski, E. & de Groot, F. M. F. The CTM4XAS program for EELS and XAS spectral shape analysis of transition metal L edges. *Micron* **41**, 687-694 (2010).
112 Uldry, A., Vernay, F. & Delley, B. Systematic computation of crystal-field multiplets for x-ray core spectroscopies. *Phys Rev B* **85**, 125-133 (2012).

113 Gunawan, A. A., Mkhoyan, K. A., Wills, A. W., Thomas, M. G. & Norris, D. J. Imaging "invisible" dopant atoms in semiconductor nanocrystals. *Nano Lett* **11**, 5553-5557 (2011).

114 Zhu, G. & Botton, G. A. Simulations of high-angle annular dark-field images of point defect configurations of Ce atoms within crystalline Si. *Bulletin of the Microscopical Society of Canada* **38**, 20-24 (2010).

115 Loane, R. F., Kirkland, E. J. & Silcox, J. Visibility of single heavy atoms on thin crystalline silicon in simulated annular dark-field STEM images. *Acta Crystallogr A* **44**, 912-927 (1988).

116 Comon, P. & Jutten, C. in *Handbook of Blind Source Separation* (Academic Press, 2010).

117 LeBeau, J. M., Findlay, S. D., Allen, L. J. & Stemmer, S. Position averaged convergent beam electron diffraction: Theory and applications. *Ultramicroscopy* **110**, 118-125 (2010).

118 Pearson, D. H., Ahn, C. C. & Fultz, B. White lines and d-electron occupancies for the 3d and 4d transition metals. *Phys Rev B* **47**, 8471-8478 (1993).

119 de Groot, F. M. F. *et al.* Oxygen 1s x-ray absorption of tetravalent titanium oxides: A comparison with single-particle calculations. *Phys Rev B* **48**, 2074-2080 (1993).

120 Shao, Y., Maunders, C., Rossouw, D., Kolodiazhnyi, T. & Botton, G. A. Quantification of the Ti oxidation state in $BaTi_{1-x}Nb_xO_3$ compounds. *Ultramicroscopy* **110**, 1014-1019 (2010).

121 Höche, T., Grodzicki, M., Heyroth, F. & van Aken, P. A. Assessment of transition-metal coordination in glasses by electron energy-loss spectroscopy. *Phys Rev B* **72**, 205111 (2005).

122 Lever, A. B. P. *Inogranic electronic spectrosocopy*. 2nd Edition edn, (Elsevier, 1984).

123 Duffy, J. A. Trends in energy gaps of binary compounds: an approach based upon electron transfer parameters from optical spectroscopy. *J Phys C: Solid State* **13**, 2979 (1980).

124 Cosgriff, E. C., Oxley, M. P., Allen, L. J. & Pennycook, S. J. The spatial resolution of imaging using core-loss spectroscopy in the scanning transmission electron microscope. *Ultramicroscopy* **102**, 317-326 (2005).

125 Stöger-Pollach, M. Optical properties and bandgaps from low loss EELS: Pitfalls and solutions. *Micron* **39**, 1092-1110 (2008).

126 Couillard, M., Yurtsever, A. & Muller, D. A. Competition between bulk and interface plasmonic modes in valence electron energy-loss spectroscopy of ultrathin SiO_2 gate stacks. *Phys Rev B* **77**, 085318 (2008).

127 Schattschneider, P. & Jouffrey, B. in *Energy-filtering Transimission Electron Microscopy Springer Series in Optical Sciences* (ed Ludwig Reimer) (Springer, Verlag Berlin Heideberg, 1995).

128 Benthem, K. v., Elsässer, C. & French, R. H. Bulk electronic structure of $SrTiO_3$: Experiment and theory. *J Appl Phys* **90**, 6156-6164 (2001).

129 Pun, T., Ellis, J. R. & Murray, E. Optimized acquisition parameters and statistical detection limit in quantitative EELS. *J microsc* **135**, 295-316 (1984).

130 Pun, T., Ellis, J. R. & Murray, E. Weighted least squares estimation of background in EELS imaging. *J microsc* **137**, 93-100 (1985).
131 Verbeeck, J. & Van Aert, S. Model based quantification of EELS spectra. *Ultramicroscopy* **101**, 207-224 (2004).
132 Unser, M., Ellis, J. R., Pun, T. & Eden, M. Optimal background estimation in EELS. *J microsc* **145**, 245-256 (1987).